MOF-Polymer Hybrid Materials towards High MOF-Loaded Thin Films

片山，雄治

MOF-Polymer Hybrid Materials towards High MOF-Loaded Thin Films

Yuji Katayama

September 2020

Performance Materials Technology Center

Corporate Research & Development

Asahi Kasei Corporation

Contents

# General Introduction

Porous Solids-Polymer Hybrid Materials

The development of nanoporous materials including zeolites and Metal-organic frameworks (MOFs, vide infra) have attracted enormous attention towards a variety of applications (e.g., separation, adsorption, storage, catalysis, and so on).[1-6]   However, nanoporous materials are mostly used as powder due to their crystalline or microcrystalline nature.[7]   In most cases, it is difficult to process those materials because of their brittleness and the poor form factor derived from their rigid nature, which limits the application of the nanoporous materials.   Therefore, improvement of their flexible form factor enables the further development of nanoporous materials towards practical applications.

One of the attractive approaches to obtain the flexible and processable materials with nanoporous solids is to use hybrid materials consisting of nanoporous solids and polymer.   While inorganic porous solids are rigid and crystalline materials, polymers have a flexible nature.   The flexible polymers have already demonstrated the excellent processability in various applications such as films.   For example, in separation membranes, although inorganic separation membranes are still struggling to be widely commercialized despite their excellent capabilities in terms of separation performance, polymeric separation membranes have been used in the industry for decades.   In the inorganic membranes, the difficult handling of the brittle inorganic active layer, the complicated fabricating processes, and the use of expensive porous inorganic substrates which is generally used as the support of the thin inorganic active layer limit the access towards the practical applications.   Therefore, combining the properties of nanoporous materials and the flexible form factor of polymer can achieve the flexible and processable hybrid materials, generating the great advance on the utility of nanoporous materials towards practical applications.

Porous Solids-Polymer Hybrid Films

One of the attractive applications of porous solids-polymer hybrid materials is formation of films, because the films can be applied to the various applications such as separation membranes, adsorptive films, battery separators, and other applications.[7-9] These applications cannot be achieved with the properties obtained from the nanoporous powder. A number of efforts towards forming flexible films with nanoporous materials have been performed for decades.

For example, among those studies, Mixed-matrix membranes (MMMs) have been most widely studied to hybridize nanoporous particles and polymer.[8] MMMs consist of dispersed inorganic porous solids and polymer matrix to obtain hybrid materials having flexible form factor of polymer and the desired properties of porous solids (**Figure 1**). This concept has been studied for decades with porous solids such as zeolites, porous carbon especially towards high performance gas separation membranes.
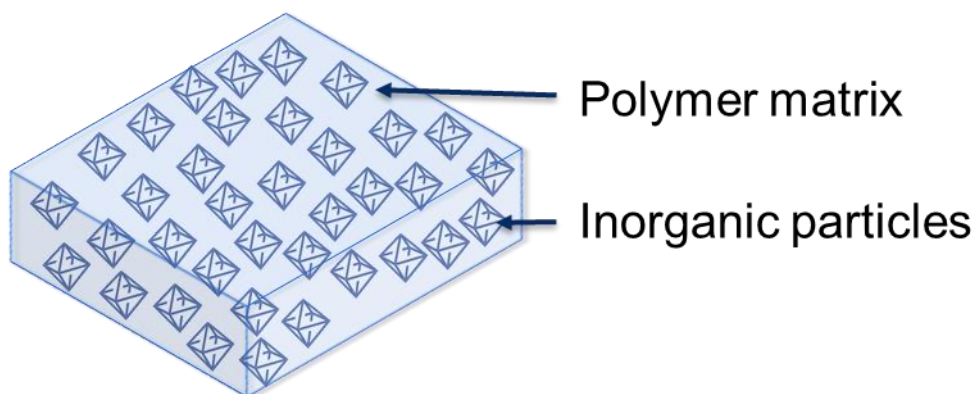
Figure 1. Concept of Mixed-matrix membranes.

Zeolites are porous minerals consist of metal-oxide bonds, and applied for separations, gas sorption, and catalysis.[1, 10] The narrow pore size of zeolites is suitable for separating gas molecules with similar size, such as O_2, N_2, CO_2, CH_4 etc.. While, porous carbon such as activated carbon have also shown the excellent size-sieving abilities towards small molecules.[11] Because the trade-off between permeability and selectivity is observed in pure-polymer gas separation membranes (known as the Robeson Upper bound),[12, 13] zeolite particles or activated carbon powder have been used as a filler in an attempt to exploit the size-sieving effect of the narrow pore size via creating MMMs to improve the separation performance of pure polymer membranes.[10, 14]

These MMMs are mostly prepared through physically mixing of particles and polymer matrix.　Most widely used method to prepare the physically mixed MMMs is simple particle dispersion and casting methods.　In the typical approach, the solution including homogeneously dispersed inorganic particles, polymer and organic solvent is casted on the substrate, heated to evaporate the solvent, producing the physically mixed MMMs.　This method has been widely used for fabricating MMMs with various porous particles and polymers towards a wide range of applications.　As thick MMMs can also be fabricated with this physical mixing method, flexible and easy-handling free-standing MMMs can be readily obtained.

　　In general, higher particle loading (e.g., over 50 wt %) is desired to make the most of the capability of porous particles in MMMs, and a thinner film is preferable in many applications.　For example, in separation membranes, thinner membrane results in greater flux, which is important toward commercialization.　The parameter of permeability (P, barrer, defined as a transport flux per unit transmembrane pressure difference per unit membrane thickness) is used to evaluate the separation capability of the membrane material, and the parameter of permeance (Q, GPU, defined as a transport flux per unit transmembrane pressure difference, meaning pressure normalized flux) is used to evaluate the membrane capabilities.　There is a correlation that permeance (Q) is in inverse proportion to membrane thickness (l) and in proportion to permeability (P):[15]

$$Q = \frac{P}{l}$$

The unit of permeability (P) is barrer, defined as

$$1\ barrer = 1\ \times 10^{-10}\ \frac{cm^3(STP)\ \times\ cm}{cm^2\ \times\ s\ \times\ cmHg}$$

The unit of permeance (Q) is GPU, defined as

$$1\ GPU = 1\ \times 10^{-6}\ \frac{cm^3(STP)}{cm^2\ \times\ s\ \times\ cmHg}$$

In the practical applications, permeance (Q) that is the pressure normalized flux is the important parameter because it finally defines the efficiency of the membrane modules. Based on the correlation above, thinner membranes such as submicron-scale thin membrane are preferable.　Therefore, a thinner film with high particle loading is one of the most desired factors in fabricating MMMs.

　　Despite the extensive works with MMMs with porous solids towards high particle loading thin MMMs, there are still limitations:　suboptimal structures ("sieve-in-a-cage" and "plugged sieves") and non-uniform morphologies such as aggregations.

The suboptimal structures including defective interfaces between the particles and polymers (called "sieve-in-a-cage" structure) and blocked pore of porous materials (called "plugged sieves" structure) result in poorer separation performances compared with desired ideal MMMs (**Figure 2**).[8]   These undesired suboptimal structures are caused by insufficient control of the interface between inorganic particles and polymer matrix, and the porous particles do not control the separation of gas molecules in these structures.

Ideal MMM 　"sieve-in-a-cage" 　"plugged sieves"

Non-selective bypasses 　　　　Blocked pores
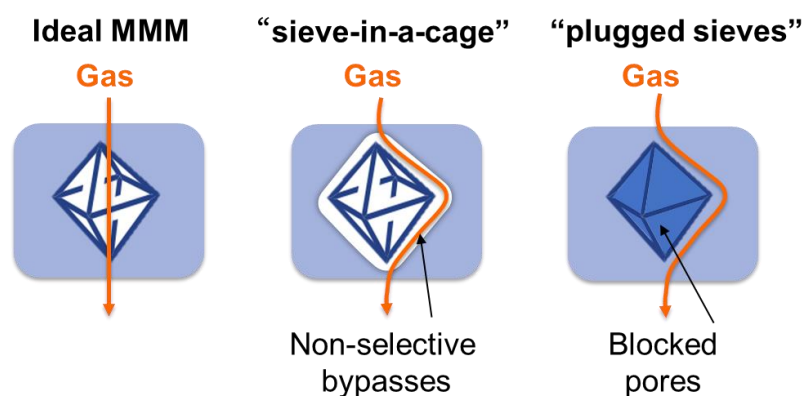
**Figure 2.**　Ideal and suboptimal structures of MMMs.

The poor particle/polymer compatibility can result in "sieve-in-a-cage" structures (**Figure 3**).[16, 17]   In case of this architecture, the space between particles and polymer matrix is generated, causing nonselective bypass pathways for gas molecules. As particles are not involved in the separation mechanism in this structure, the desired size-sieving properties of the filler are not obtained, which result in the decreased or maintained selectivity at best.   Though permeability would increase due to the bypass pathways, this architecture causes the pinhole defects especially in thin films as thinner films tend to be susceptible to the pinhole formation.   The critical pinhole defects defeat the ability of the membranes to separate.[18, 19]   The pinhole defects cause a non-selective convection transport, resulting in the significant decrease of selectivity.

On the other hand, the pores of the porous solids can be blocked with the small molecules and polymer chains, which results in "plugged sieves" structures.[8]   In this structure, the gas molecules are not able to pass through the pore of the filler, having to circumvent the blocked particles, passing through longer pathway, resulting in the decrease of gas permeability.

Non-uniform morphologies such as severe aggregation often occur in physically mixed MMMs with high particle loading (over 50 wt %), even though high particle loading is desired.   The particle aggregation generates the macrovoids or

4

pinhole, resulting in a severe decrease of selectivity.   These non-uniform structures are caused by the poor particle dispersibility in the polymer matrix and a lack of particle assembly control.

Therefore, towards the high-performance porous solids/polymer hybrid films including MMMs, the precise control of the particle/polymer interface is essential. Developing the way to control the interfaces between porous solids and polymer would avoid suboptimal and non-uniform structures, generating the new materials including films to overcome current limits of porous solids/polymer hybrid materials towards diverse applications.
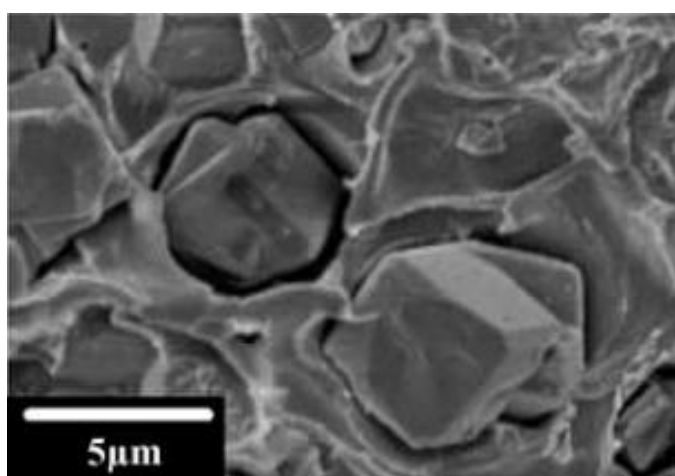
Figure 3. The example of "sieve-in-a-cage" structure: MMMs with Zeolite 4A particles.[20]

Metal-Organic Frameworks (MOFs)

To control the interface between nanoporous materials and polymer, Metal-organic frameworks (MOFs) also known as Porous coordinating polymers (PCP) have been sought after because of their distinctive properties.   MOFs are three-dimensional crystalline porous materials with inorganic metal ions and rigid organic linkers, which are connected with coordination bonds (**Figure 4**).[21-23]   Therefore, MOFs have both properties of organic and inorganic materials in contrast to other porous solids like zeolites, which is the significant advantage towards the integration of inorganic porous materials and polymer.[22]   For example, the particle/polymer interfaces in the hybrid materials can be controlled by modifying the organic linker of the inorganic MOF particles with organic reagents, which also enables to tune the diverse chemical functionality of MOFs towards the specific applications.   Moreover, due to their unique structure, MOFs demonstrate the extraordinary high surface area with uniform nanopores.   As MOFs can be designed with the countless combinations of metal ions and organic linkers, the extensive structural variety and the tunable porosity can be achieved.   In addition, MOFs can be synthesized with simpler and more processable conditions compared to conventional porous inorganic materials like zeolites, which enables MOF materials to access to the commercial applications.[24]   By taking advantage of these unique properties, MOFs have demonstrated exceptional separation, storage, and catalysis capacities, pushing the limits of the nanoporous inorganic materials toward a wide range of applications over the last two decades.[2-5, 25] Therefore, MOFs have a particularly high potential towards MOF-polymer hybrid materials due to the organic/inorganic functionality for the control of particle/polymer interfaces, the diverse chemical tunability, the high surface area with uniform nanopores, structural varieties, and simple synthesis conditions.
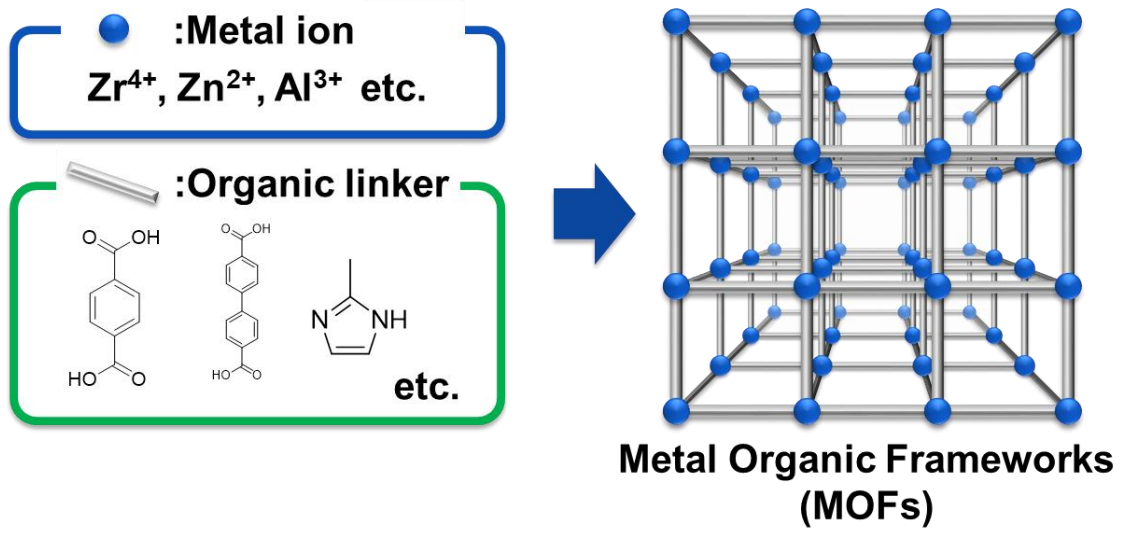
Figure 4. Metal-organic frameworks (MOFs)

MOFs for Film Application

        To date, pure-MOFs films have shown the potential to the practical application such as separation membranes, adsorptive films, battery separators, and sensors and so on.[9, 26]   For example, pure-MOF membranes have shown the excellent features in gas separation in terms of selectivity and permeability.   Because the uniform MOF pores are an ideal structure for the size-sieving and the high porosity of MOFs allows more gas molecules to pass through the membranes, the high selectivity and permeability have been achieved (**Figure 5**).   For example, separation membranes with ZIF-8 (ZIF: Zeolitic Imidazolate Framework), a class of zinc-based MOFs, have shown the excellent separation performances.   ZIF-8 membrane shows the great propylene permeability and propylene/propane selectivity beyond Robson upper bound which is the trade-off limit of polymer membranes.[27]

        Towards practical applications, though the pure-MOF films are brittle and have a poor processability due to their crystalline nature as well as other inorganic materials like zeolites, MOFs have a great potential to achieve the high performance porous solids-polymer hybrid films by taking advantage of the unique MOF properties such as the controllable particle/polymer interfaces.
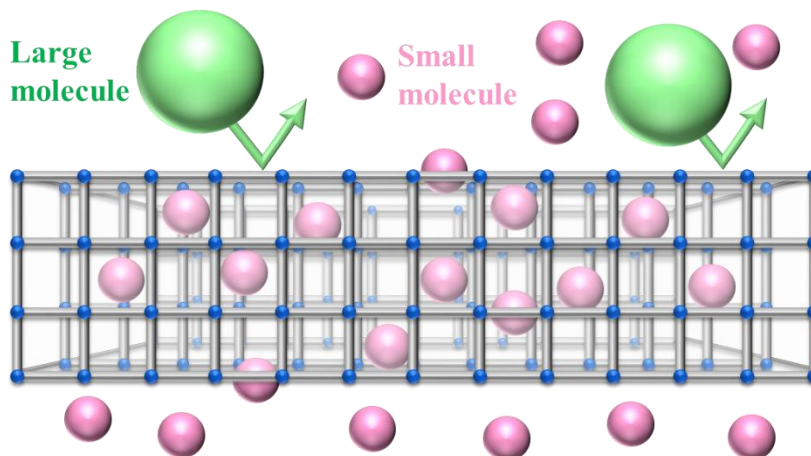
Figure 5.   Size-sieving property of MOF-based separation membrane.

MOF-Polymer Hybrid Materials

Therefore, hybridizing MOFs having a high performance towards practical application and flexible polymer would generate the novel flexible and processable nanoporous materials. A number of efforts towards combining the properties of MOFs and the flexible nature of polymer have been performed, showing the advance of the utility of MOFs. Recently, various approaches to create MOF-polymer hybrid materials have been studied, which includes MMMs,[28] polymers grafted from MOF particles,[29] polymerization in MOFs, polymers templating MOF growth, MOFs composed of polymer ligands (PolyMOFs).[30-34] (**Figure 6**). These approaches are classified into two strategies; top-down and bottom-up approaches. Top-down approach is the way where MOF particles are initially synthesized and subsequently hybridized with polymer (e.g., MMMs).[28] While bottom-up approach is the way where MOF-polymer hybrid materials are synthesized when MOF formation is proceeding (e.g., PolyMOFs). Some of these approaches about MOF-polymer hybrid materials would create a platform to utilize these materials toward practical applications. Among these strategies, top-down approaches including MOF-based MMMs have been most widely studied towards MOF-polymer hybrid fims.[28]
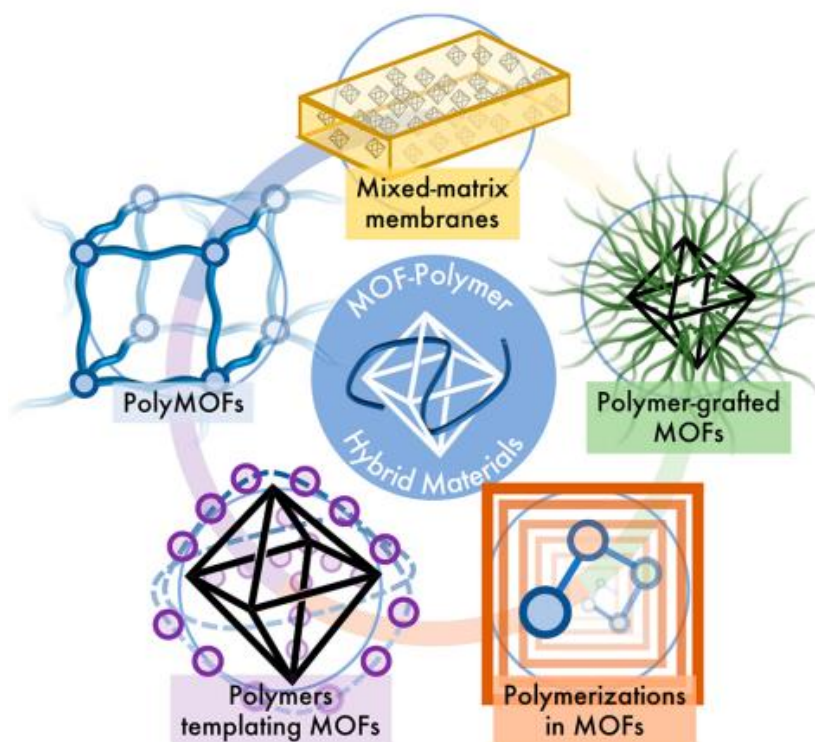
Figure 6. Overview of MOF-Polymer hybrid materials.[35]

MOF-Polymer Hybrid Films

By taking advantage of the unique properties of MOFs, where MOF has both properties of organic and inorganic materials, a numbers of efforts to control the MOF/polymer interface have been performed in the top-down approach of MOF-based MMMs.[22]   Various approaches have been studied to obtain improved MMMs especially for the gas separation application for a decade.[7, 35]   Since some MOFs demonstrate higher flux and selectivity than polymer-only membranes, the incorporation of MOF particles in polymer matrix have been sought after towards high performance gas separation membranes.

In MOF-based MMMs, there are two main approaches to control the MOF/polymer interfaces.   First approach is MMMs fabricated through the conventional simple physical mixing with unmodified MOF particles and polymer in order to generate noncovalent bonding such as π-π stacking or hydrogen bonding between MOF particles and polymer matrix.   The second approach involves the chemical modification of the organic ligands of MOF particles in order to improve the surface properties of the particles.

The second approach of MMMs with modified MOF particles have attracted the enormous attention recently because most MMMs in first approach are focusing on relatively low MOF loadings (less than 40 wt %).   Especially, the modification MOF particles with polymer offers a variety of approaches to tailor MOF surface properties towards desired MMMs.   For example, by attaching polymers to the MOF linker with covalent bonds, it is possible to introduce the strong interactions at the particle/polymer interface, which shows the potential to achieve the complete integration of MOF and polymer components towards the desired MOF/polymer hybrid films.

MOF Modification Methods

Compared to other porous solids like zeolites, one of the great advantages of MOF materials is the unique ability for the modification.   In order to control MOF/polymer interface in MMMs, it is a strong tool to modify presynthesized MOF particles through postsynthetic manners such as postsynthetic exchange (PSE), postsynthetic modification (PSM), postsynthetic polymerization (PSP) (**Figure 7**).[36] These unique methods make it possible to generate functional MOFs that are not accessible from direct synthesis, and to functionalize the surface of the MOF particles.

Through PSE reaction, linkers in MOF particles are readily replaced with other linkers without loss of MOF crystallinity or porosity.[37]   In the case that the newly introduced linker is bigger than the pore size of MOF particles, PSE reaction tend to proceed only on the particle surface leaving the inside pore intact, which result in the surface modification of the MOF particles.

PSM is a process involving the reaction with reagents and MOF particles.[36] The reagents react with the functional groups of organic linkers or metal nodes, which results in the functionalization of MOF particles.   When the reagents react with the functional groups of the organic linkers and form covalent bonds, the strong connection between MOFs and the newly introduced components can be achieved.   If reagents are balky, the modification can occur only on the particle surface.

In PSP reaction, a polymer chain grows from the functional groups of linkers as a "grafting-from" method.[38, 39]   The covalent surface modification of MOF particles with polymer can be achieved through the PSP reaction.   By attaching the polymerization initiator to the MOF linker, a living radical polymerization can be used for the PSP reaction, resulting in the precise control of the polymerization.

Through these postsynthetic methods or combination of these, the modification of the surface properties of MOFs without loss of original MOF properties can be achieved, enabling the precise control of MOF-polymer interface towards MOF-polymer hybrid materials.
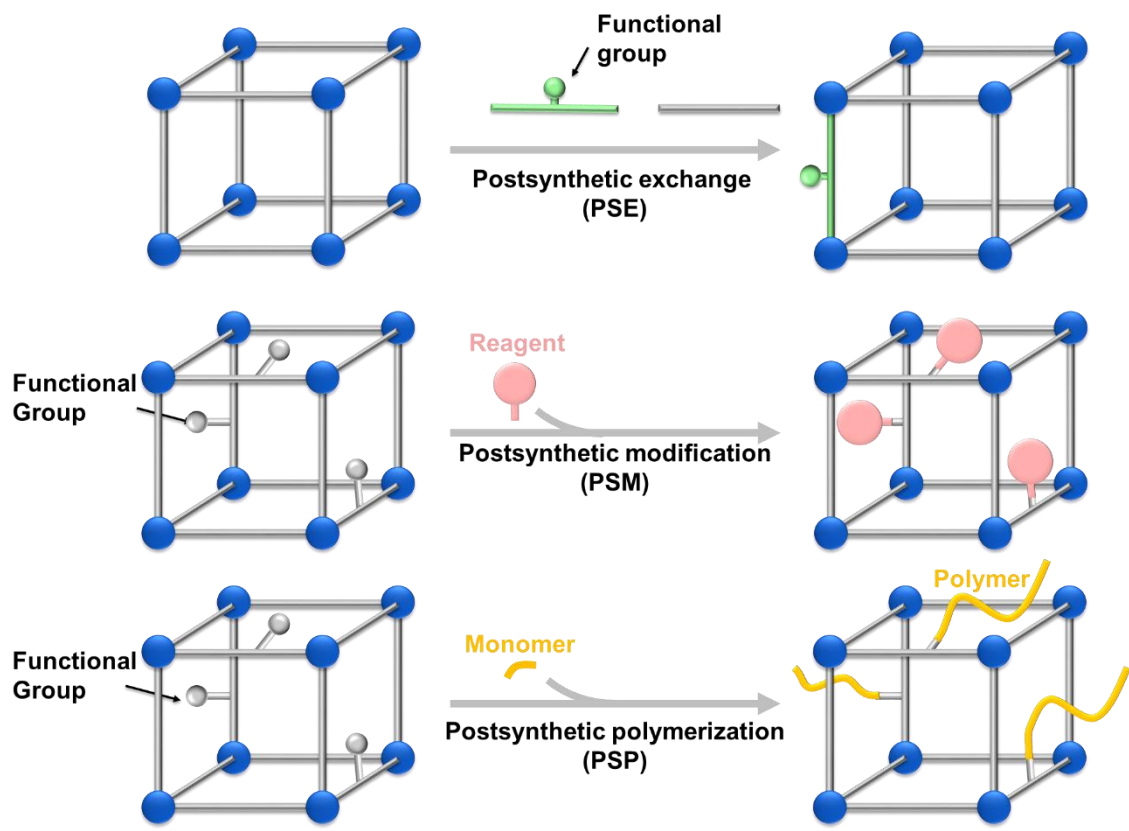
Figure 7. Schemes of Postsynthetic methods: postsynthetic exchange, postsynthetic modification, postsynthetic polymerization.

Core-Shell MOFs Approach

One of the interesting approaches to modify MOF particles is to utilize core-shell MOFs with polymer shell.   Polymer shells provide unique properties: a strong adhesion of covalent bonds between inorganic MOF particles and organic polymer shell; a good dispersibility in organic solvent or polymer matrix; further reactions form the functional groups in the polymer shell; protection of MOF pores from pore-blocking; adhesions of each particles via physical interactions of the flexible polymer shell and so on.

There are two common methods to synthesize core-shell MOF particles; "grafting-to" and "grafting-from" method.[35, 40-43]   A "grafting-to" method is achieved through PSM reactions with presynthesized polymers with reactive groups and MOF particles with functional groups.   As the polymer can be prepared with precise control of the molecular weight and dispersity prior to PSM reaction, the shell size of core-shell MOFs is controlled facilely with a simple procedure.   It is a significant advantage to characterize the properties of the polymer before the "grafting-to" reaction.   However, the grafting density tend to be poor through the "grafting-to" method, which limits the amount of polymer on the MOF particles.

In contrast, "grafting-from" method is performed through PSP reaction with MOF particles modified with polymerization-initiating sites.[44]   The polymers are grown from the initiating sites through PSP reaction.   This method generates highly dense polymer brushes and results in large amount of polymer on the MOF particles. In this method, a living radical polymerization such as Atom transfer radical polymerization (ATRP) can be applied and the dense polymer shell can be achieved.

Though several studies about these approaches towards MMMs with good MOF/polymer compatibility have been reported,[38, 45-51] it is still challenging to achieve high MOF-loaded MOF-polymer hybrid films, especially in the case of thin films.

(a)
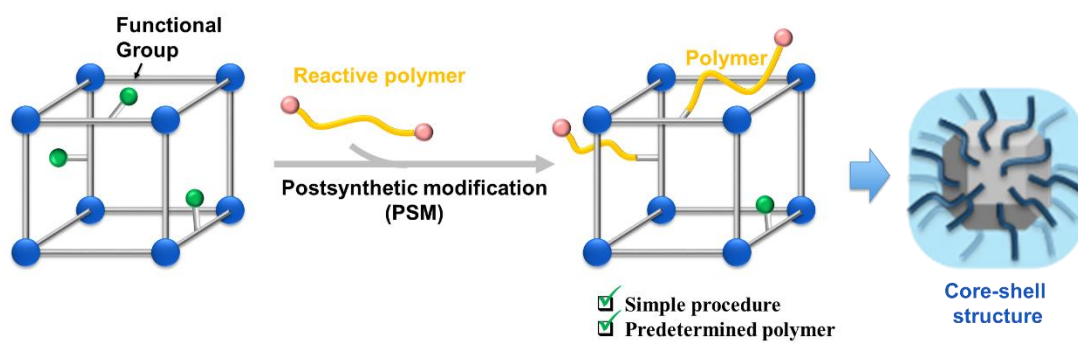
(b)
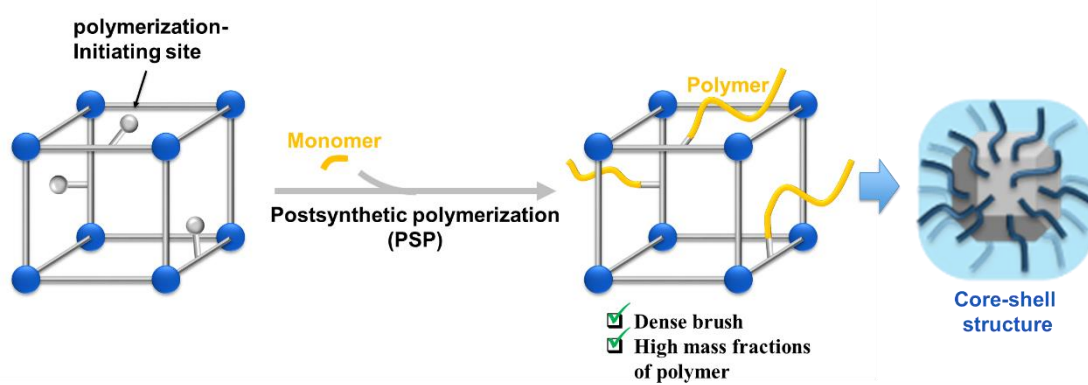
Figure 8. Schemes of grafting routes: (a) "Grafting-to" method. (b) "Grafting-from" method
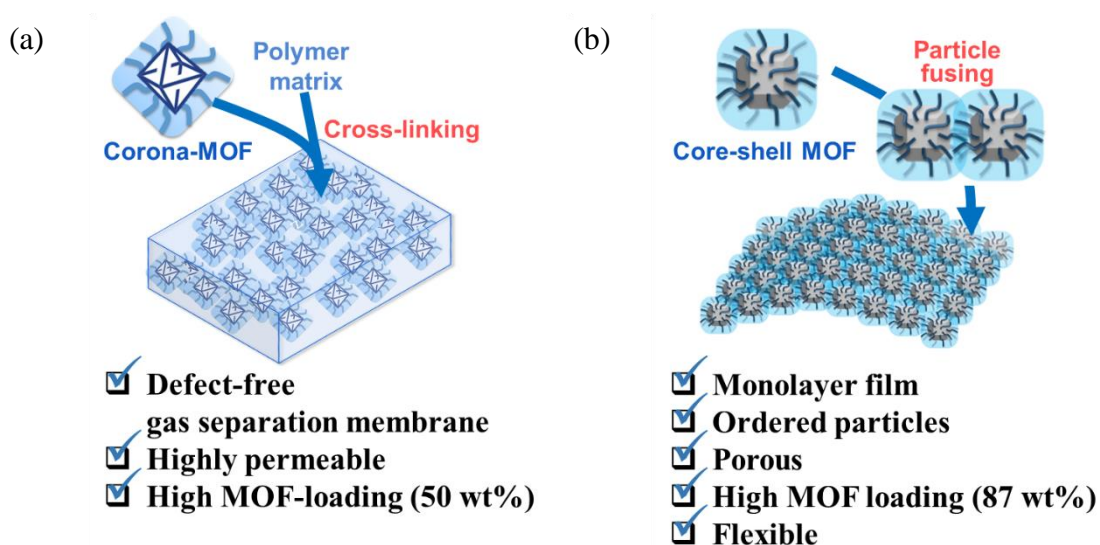
Purpose of This Research

In this study, in order to control the MOF-polymer interfaces and to achieve MOF-polymer hybrid materials towards high MOF-loaded thin films, we synthesized core-shell structured MOFs with the polymer shell (termed "corona-MOF" in Chapter 1, termed "core-shell MOF" in Chapter 2) (**Figure 9**).   The polymer chain of the shell is covalently integrated to the surface of the MOF particles using postsynthetic methods such as PSM, PSE, and PSP in order to obtain core-shell structured MOF particles.   By using core-shell structured MOFs, the flexible MOF-polymer hybrid films with high MOF loading were achieved.   Additionally, to demonstrate the potential of the core-shell strategy, we also synthesized thin MMMs with high MOF loading and the high MOF loading monolayer with ordered particles.

In Chapter 1, we synthesized a PDMS-decorated MOF (termed here "corona-MOF") by covalently grafting allyl-functionalized UiO-66 (UiO-66-Allyl) (UiO: University of Oslo) with hydride-terminated poly(dimethylsiloxane) (PDMS) as a "grafting-to" method.   The corona-MOFs and PDMS polymer matrix were used to fabricate defect-free MMMs for gas separation membranes.   The hydrophobic corona generates the excellent particle dispersibility in the PDMS polymer matrix, and the cross-linking of the corona and PDMS polymer matrix with covalent linkages gives strong MOF/polymer adhesion.   These factors allowed for fabrication of the defect-free MMMs with 50 wt % MOF loading.   The single gas separation tests demonstrated the improved separation performance of corona-MOF MMMs, showing the significant advantage of corona-MOFs strategy.   This strategy is also able to be used for the fabrication of free-standing flexible thin films (<1 μm thickness) without any apparent macrovoids, which demonstrates the applicability of this concept towards practical applications.

In Chapter 2, we synthesized porous monolayers and free-standing multilayer films via self-assembly.   Despite a lot of efforts towards fabricating monolayers with nanoparticles for various applications, densely ordered porous thin monolayers have not been reported.   The self-assembled MOF monolayers (termed here "SAMMs") were achieved with core-shell MOF particles via a liquid-air interface method, resulting in an extremely thin MOF/polymer hybrid film with the controlled particle assembly.   Core-shell MOFs were obtained by synthesizing the layer of poly(methyl methacrylate) (PMMA) on ZIF-8 particles using a histamine anchor via ATRP reaction ("grafting-from" method).   SAMMs were obtained as thin films with 87 wt % (89 vol %) MOF loading and the intact porosity.   Additionally, MOF multilayers such as alternating

MOF/polymer heterostructures were synthesized by stacking SAMMs.   SAMMs were also able to be covered on the three-dimensional object such as silicon microparticles, and free-standing self-assembled films with five-particle thickness showing opalescence were also fabricated.   This achievement of MOF-polymer monolayer is a significant advancement for creating a platform towards various applications such as porous membranes and coatings.   To the best of our knowledge, this study is the first report about self-assembled porous monolayer and free-standing self-assembled multilayer films composed of MOF nanoparticles.

Figure 9. Purpose of this research: (a) Defect-free MOF-based MMMs obtained by corona cross-linking for gas separation.   (b) Self-assembly of MOF nanoparticle monolayers.

References

1.	Rangnekar, N.;	Mittal, N.;	Elyassi, B.;	Caro, J.; Tsapatsis, M., Zeolite membranes – a review and comparison with MOFs. *Chemical Society Reviews* **2015,** *44* (20), 7128-7154.

2.	Kirchon, A.;	Feng, L.;	Drake, H. F.;	Joseph, E. A.; Zhou, H. C., From fundamentals to applications: a toolbox for robust and multifunctional MOF materials. *Chem Soc Rev* **2018,** *47* (23), 8611-8638.

3.	Li, J. R.;	Sculley, J.; Zhou, H. C., Metal-organic frameworks for separations. *Chem Rev* **2012,** *112* (2), 869-932.

4.	Suh, M. P.;	Park, H. J.;	Prasad, T. K.; Lim, D. W., Hydrogen storage in metal-organic frameworks. *Chem Rev* **2012,** *112* (2), 782-835.

5.	Khan, N. A.;	Hasan, Z.; Jhung, S. H., Adsorptive removal of hazardous materials using metal-organic frameworks (MOFs): a review. *J Hazard Mater* **2013,** *244-245*, 444-56.

6.	Li, Y.;	Li, L.; Yu, J., Applications of Zeolites in Sustainable Chemistry. *Chem* **2017,** *3* (6), 928-949.

7.	Dechnik, J.;	Gascon, J.;	Doonan, C. J.;	Janiak, C.; Sumby, C. J., Mixed-Matrix Membranes. *Angew. Chem. Int. Ed.* **2017,** *56*, 9292-9310.

8.	Rezakazemi, M.;	Ebadi Amooghin, A.;	Montazer-Rahmati, M. M.; Ismail, A. F.; Matsuura, T., State-of-the-Art Membrane Based CO2 Separation Using Mixed Matrix Membranes (MMMs): An Overview on Current Status and Future Directions. *Prog. Polym. Sci.* **2014,** *39*, 817-861.

9.	Li, W., Metal–organic framework membranes: Production, modification, and applications. Progress in Materials Science: Vol. 100, pp 21-63.

10.	Bastani, D.;	Esmaeili, N.; Asadollahi, M., Polymeric mixed matrix membranes containing zeolites as a filler for gas separation applications: A review. *J. Ind. Eng. Chem.* **2013,** *19*, 375-393.

11.	Saufi, S. M.; Ismail, A. F., Fabrication of carbon membranes for gas separation—a review. *Carbon* **2004,** *42* (2), 241-259.

12.	Robeson, L. M., The Upper Bound Revisited. *J. Membr. Sci.* **2008,** *320*, 390-400.

13.	Robeson, L. M.;	Liu, Q.;	Freeman, B. D.; Paul, D. R., Comparison of transport properties of rubbery and glassy polymers and the relevance to the upper bound relationship. *Journal of Membrane Science* **2015,** *476*, 421-431.

14.	García, M. G.;	Marchese, J.; Ochoa, N. A., High activated carbon loading

mixed matrix membranes for gas separations. *Journal of Materials Science* **2012,** *47* (7), 3064-3075.

15.   Freeman, B. D., Yampolskii, Y., Pinnau, I, *Materials Science of Membranes for Gas and Vapor Separation*. John Wiley & Sons: 2006.

16.   Lin, R.;   Villacorta Hernandez, B.;   Ge, L.; Zhu, Z., Metal Organic Framework Based Mixed Matrix Membranes: An Overview on Filler/Polymer Interfaces. *J. Mater. Chem. A* **2018,** *6*, 293-312.

17.   Anjum, M. W.;   Vermoortele, F.;   Khan, A. L.;   Bueken, B.;   De Vos, D. E.; Vankelecom, I. F. J., Modulated UiO-66-Based Mixed-Matrix Membranes for CO2 Separation. *ACS Appl. Mater. Interfaces* **2015,** *7*, 25193-25201.

18.   Gao, X.;   Zhang, J.; Huang, K., ROMP for Metal–Organic Frameworks: An Efficient Technique toward Robust and High-Separation Performance Membranes. *ACS Appl. Mater. Interfaces* **2018,** *10*, 34640-34645.

19.   Park, H. B.;   Kamcev, J.;   Robeson, L. M.;   Elimelech, M.; Freeman, B. D., Maximizing the Right Stuff: The Trade-Off Between Membrane Permeability and Selectivity. *Science* **2017,** *356*, eaab0530.

20.   Moore, T. T.; Koros, W. J., Non-ideal effects in organic–inorganic materials for gas separation membranes. *Journal of Molecular Structure* **2005,** *739* (1), 87-98.

21.   Meek, S. T.;   Greathouse, J. A.; Allendorf, M. D., Metal-Organic Frameworks: A Rapidly Growing Class of Versatile Nanoporous Materials. *Adv. Mater.* **2011,** *23*, 249-267.

22.   Yaghi, O. M.;   O'Keeffe, M.;   Ockwig, N. W.;   Chae, H. K.;   Eddaoudi, M.; Kim, J., Reticular Synthesis and the Design of New Materials. *Nature* **2003,** *423*, 705-714.

23.   Eddaoudi, M.;   Kim, J.;   Rosi, N.;   Vodak, D.;   Wachter, J.;   O'Keeffe, M.; Yaghi, O. M., Systematic design of pore size and functionality in isoreticular MOFs and their application in methane storage. *Science* **2002,** *295* (5554), 469-72.

24.   Stock, N.; Biswas, S., Synthesis of metal-organic frameworks (MOFs): routes to various MOF topologies, morphologies, and composites. *Chem Rev* **2012,** *112* (2), 933-69.

25.   Yuan, S.;   Feng, L.;   Wang, K.;   Pang, J.;   Bosch, M.;   Lollar, C.;   Sun, Y.;   Qin, J.;   Yang, X.;   Zhang, P.;   Wang, Q.;   Zou, L.;   Zhang, Y.;   Zhang, L.; Fang, Y.;   Li, J.; Zhou, H. C., Stable Metal-Organic Frameworks: Design, Synthesis, and Applications. *Adv Mater* **2018,** *30* (37), e1704303.

26.   Shekhah, O.;   Chernikova, V.;   Belmabkhout, Y.; Eddaoudi, M., Metal–Organic Framework Membranes: From Fabrication to Gas Separation. *Crystals*: 2**018**;

Vol. 8, p 412.

27.　　　Kwon, H. T.; Jeong, H.-K., In Situ Synthesis of Thin Zeolitic–Imidazolate Framework ZIF-8 Membranes Exhibiting Exceptionally High Propylene/Propane Separation. *J. Am. Chem. Soc.* **2013,** *135*, 10763-10768.

28.　　　Denny Jr, M. S.;　Moreton, J. C.;　Benz, L.; Cohen, S. M., Metal–organic frameworks for membrane-based separations. *Nat. Rev. Mater.* **2016,** *1*, 16078.

29.　　　Wang, H.;　He, S.;　Qin, X.;　Li, C.; Li, T., Interfacial Engineering in Metal–Organic Framework-Based Mixed Matrix Membranes Using Covalently Grafted Polyimide Brushes. *J. Am. Chem. Soc.* **2018,** *140*, 17203-17210.

30.　　　Ayala, S.;　Bentz, K. C.; Cohen, S. M., Block co-polyMOFs: morphology control of polymer-MOF hybrid materials. *Chem Sci* **2019,** *10* (6), 1746-1753.

31.　　　Ayala, S.;　Zhang, Z.; Cohen, S. M., Hierarchical structure and porosity in UiO-66 polyMOFs. *Chem Commun (Camb)* **2017,** *53* (21), 3058-3061.

32.　　　Schukraft, G. E. M.;　Ayala, S.;　Dick, B. L.; Cohen, S. M., Isoreticular expansion of polyMOFs achieves high surface area materials. *Chem Commun (Camb)* **2017,** *53* (77), 10684-10687.

33.　　　Zhang, Z.;　Nguyen, H. T.;　Miller, S. A.;　Ploskonka, A. M.;　DeCoste, J. B.; Cohen, S. M., Polymer-Metal-Organic Frameworks (polyMOFs) as Water Tolerant Materials for Selective Carbon Dioxide Separations. *J Am Chem Soc* **2016,** *138* (3), 920-5.

34.　　　Zhang, Z.;　Nguyen, H. T.;　Miller, S. A.; Cohen, S. M., polyMOFs: A Class of Interconvertible Polymer-Metal-Organic-Framework Hybrid Materials. *Angew Chem Int Ed Engl* **2015,** *54* (21), 6152-7.

35.　　　Kalaj, M.;　Bentz, K. C.;　Ayala, S.;　Palomba, J. M.;　Barcus, K. S.;　Katayama, Y.; Cohen, S. M., MOF-Polymer Hybrid Materials: From Simple Composites to Tailored Architectures. *Chem Rev* **2020**.

36.　　　Cohen, S. M., Postsynthetic Methods for the Functionalization of Metal–Organic Frameworks. *Chem. Rev.* **2012,** *112*, 970-1000.

37.　　　Kim, M.;　Cahill, J. F.;　Su, Y.;　Prather, K. A.; Cohen, S. M., Postsynthetic ligand exchange as a route to functionalization of 'inert' metal–organic frameworks. *Chemical Science* **2012,** *3* (1), 126-130.

38.　　　Yao, B.-J.;　Jiang, W.-L.;　Dong, Y.;　Liu, Z.-X.; Dong, Y.-B., Post-Synthetic Polymerization of UiO-66-NH2 Nanoparticles and Polyurethane Oligomer toward Stand-Alone Membranes for Dye Removal and Separation. *Chem. Eur. J.* **2016,** *22*, 10565-10571.

39.　　　Kalaj, M.;　Denny Jr., M. S.;　Bentz, K. C.;　Palomba, J. M.; Cohen, S. M.,

Nylon–MOF Composites through Postsynthetic Polymerization. *Angewandte Chemie International Edition* **2019,** *58* (8), 2336-2340.

40.   Dukes, D.; Li, Y.; Lewis, S.; Benicewicz, B.; Schadler, L.; Kumar, S. K., Conformational Transitions of Spherical Polymer Brushes: Synthesis, Characterization, and Theory. *Macromolecules* **2010,** *43*, 1564-1570.

41.   Hansson, S.; Trouillet, V.; Tischer, T.; Goldmann, A. S.; Carlmark, A.; Barner-Kowollik, C.; Malmstrom, E., Grafting Efficiency of Synthetic Polymers onto Biomaterials: A Comparative Study of Grafting-from versus Grafting-To. *Biomacromolecules* **2013,** *14*, 64-74.

42.   Radhakrishnan, B.; Ranjan, R.; Brittain, W. J., Surface Initiated Polymerizations from Silica Nanoparticles. *Soft Matter* **2006,** *2*, 386-396.

43.   Bentz, K. C.; Savin, D. A., Chain Dispersity Effects on Brush Properties of Surface-Grafted Polycaprolactone-Modified Silica Nanoparticles: Unique Scaling Behavior in the Concentrated Polymer Brush Regime. *Macromolecules* **2017,** *50*, 5565-5573.

44.   Xie, K.; Fu, Q.; Kim, J.; Lu, H.; He, Y.; Zhao, Q.; Scofield, J.; Webley, P. A.; Qiao, G. G., Increasing Both Selectivity and Permeability of Mixed-Matrix Membranes: Sealing the External Surface of Porous MOF Nanoparticles. *J. Membr. Sci.* **2017,** *535*, 350-356.

45.   Gao, X.; Zhang, J.; Huang, K.; Zhang, J., ROMP for Metal–Organic Frameworks: An Efficient Technique toward Robust and High-Separation Performance Membranes. *ACS Appl. Mater. Interfaces* **2018,** *10*, 34640-34645.

46.   Molavi, H.; Shojaei, A.; Mousavi, S. A., Improving Mixed-Matrix Membrane Performance via PMMA Grafting from Functionalized NH2–UiO-66. *J. Mater. Chem. A* **2018,** *6*, 2775-2791.

47.   Tien-Binh, N.; Rodrigue, D.; Kaliaguine, S., In-Situ Cross Interface Linking of PIM-1 Polymer and UiO-66-NH2 for Outstanding Gas Separation and Physical Aging Control. *J. Membrane Sci.* **2018,** *548*, 429-438.

48.   Yao, B.-J.; Ding, L.-G.; Li, F.; Li, J.-T.; Fu, Q.-J.; Ban, Y.; Guo, A.; Dong, Y.-B., Chemically Cross-Linked MOF Membrane Generated from Imidazolium-Based Ionic Liquid-Decorated UiO-66 Type NMOF and Its Application toward CO2 Separation and Conversion. *ACS Appl. Mater. Interfaces* **2017,** *9*, 38919-38930.

49.   Zhang, Y.; Feng, X.; Li, H.; Chen, Y.; Zhao, J.; Wang, S.; Wang, L.; Wang, B., Photoinduced Postsynthetic Polymerization of a Metal-Organic Framework toward a Flexible Stand-Alone Membrane. *Angew. Chem., Int. Ed.* **2015,** *54*, 4259-4263.

50.   Jiang, W.-L.;   Ding, L.-G.;   Yao, B.-J.;   Wang, J.-C.;   Chen, G.-J.;   Li, Y.-A.;   Ma, J.-P.;   Ji, J.;   Dong, Y.; Dong, Y.-B., A MOF-Membrane Based on the Covalent Bonding Driven Assembly of a NMOF with an Organic Oligomer and its Application in Membrane Reactors. *Chem. Commun.* **2016,** *52*, 13564-13567.

51.   Satheeshkumar, C.;   Yu, H. J.;   Park, H.;   Kim, M.;   Lee, J. S.; Seo, M., Thiol–Ene Photopolymerization of Vinyl-Functionalized Metal–Organic Frameworks Towards Mixed-Matrix Membranes. *J. Mater. Chem. A* **2018,** *6*, 21961-21968.

Chapter 1

Defect-Free MOF-Based Mixed-Matrix Membranes Obtained by Corona Cross-Linking for Gas Separation

Abstract

Allyl-functionalized UiO-66 (UiO: University of Oslo) type Metal-organic framework (MOF) particles were grafted with hydride-terminated poly(dimethylsiloxane) (PDMS) with covalent bonds via "graft-to method" as postsynthetic modification (PSM).   The PDMS-grafted particles (termed here "corona-MOFs") were utilized to fabricate high MOF loaded Mixed-matrix membranes (MMMs) with PDMS polymer matrix.   Because the PDMS corona possesses unreacted terminal hydride group, it can be further reacted with PDMS polymer matrix. Therefore, the corona is bound to both the particles and the polymer matrix, acting as a bridge, creating a strong MOF/polymer matrix adhesion.   Attributed to the improved MOF/polymer matrix adhesion with covalent linkages and the dispersibility of the particles in the polymer matrix, 50 wt % defect-free MOF-loaded MMMs were achieved.

In single gas permeation tests, the corona-MOF MMMs demonstrated the higher CO_2 gas permeability than PDMS-only membrane without loss of the selectivity, which shows distinct property of corona-MOF MMMs.   On the other hand, MMMs with undecorated MOF particles showed the decreased selectivity, indicating the presence of pinholes.   To identify the separation mechanism of corona-MOF MMMs, the permeability of various sized gases such as CO_2, N_2, and propane were measured with single gas separation tests.   The results show that the corona-MOF MMMs demonstrate the size-sieving ability, which supports the fact that the separation mechanism of corona-MOF MMMs is an "ideal MMMs" scenario which avoids sub-optimal "sieve-in-a-cage" and "plugged sieves" structures.

In addition, by taking advantage of the strong MOF/polymer adhesion and the

excellent dispersibility of the particles in the polymer matrix, the self-standing thin MMMs (<1 μm in thickness) with good flexibility were achieved.   The covalently attached corona of low quantities of polymer (<5 wt %) acts an important role in fabricating the defect-free, high MOF-loaded thin MMMs.

Introduction

One of the most attractive applications of Metal-organic frameworks (MOFs) is MOF-based separation membrane.[1-3] Since separation membranes can separate without phase change and heat, membrane separations can drastically reduce the energy consumption compared to the conventional distillation, which is the most common separation method now in various purification processes. For example, Sholl et al. reported that the chemical separations such as hydrocarbon separation, separation of alkenes from alkanes and separation of benzene derivatives from each other, account for half of the US industrial energy consumption and 10-15 % of the world's energy use, suggesting one potential way to reduce the huge energy use is to apply separation membranes. As separation membranes require 90% less energy than distillation (**Figure 1–1**), developing high performance separation membranes would generate a huge impact on industrial processes.[4] One attractive strategy is to develop MOF-based membranes. Because their uniform and tunable nanopores can be suitably applied to the size-sieving separations, separation membranes with MOFs have a huge potential for the future separation processes.
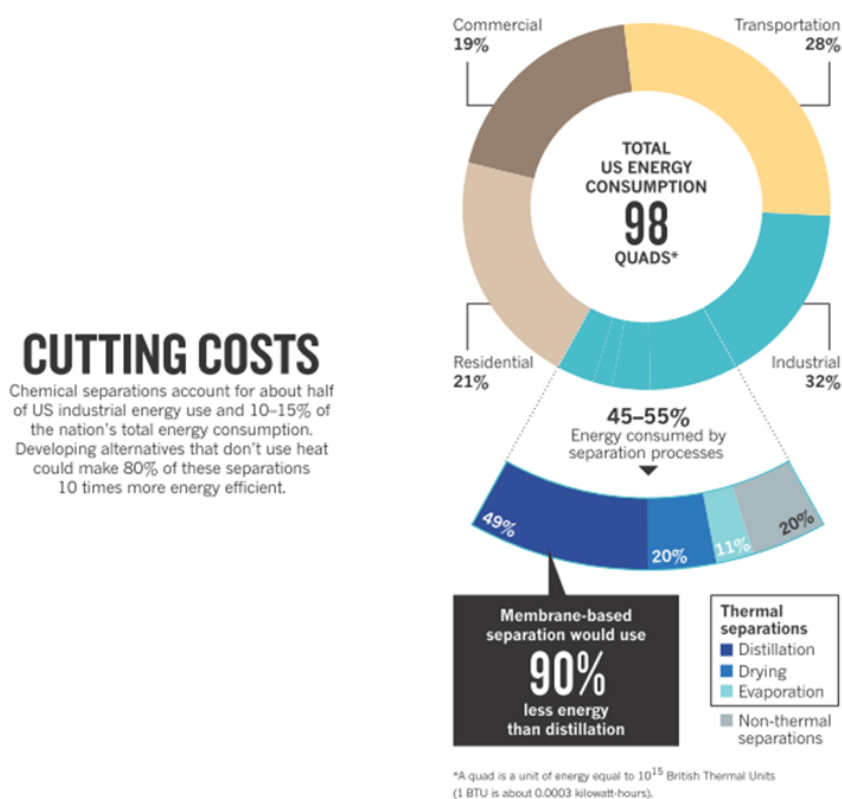
Figure 1–1. Total US energy consumption and the potential of membrane separation for energy reduction. [4]

As discussed in general introduction, several efforts have performed to prepare pure-MOF membranes, where the thin MOF active layer is synthesized on the porous substrate such as ceramic supports through secondary growth, seeded growth or direct growth methods.[1, 2, 5-7] As an uniform pore size and versatile functionalities of MOFs are suitable for separating molecules, pure-MOF membranes show excellent separation performances such as permeability and selectivity. However, due to their crystalline nature, the brittleness and poor processability limit the industrial applications. In addition, expensive rigid porous ceramic substrates are widely used to support the brittle MOF active layer, which also hampers pure-MOF membranes from the commercialization. Though there are some efforts to use organic polymer substrates instead of inorganic substrates,[8-11] the complicated processes to deposit MOF active layer on the polymer substrate and the careful handling of fragile MOF active layer still limit the application of the membrane in the industry.

One of the alternative route toward fabricating MOF membranes is Mixed-matrix membranes (MMMs) (**Figure 1**, see General introduction).[12-14] MMMs consist of dispersed inorganic porous solids and polymer matrix to make hybrid materials having flexible form factor of polymer and the desired properties of porous solids. MMMs have shown a potential to obtain an outstanding separation performance derived from size-sieving effects of porous solids with a good processability and flexibility. Additionally, fabricating free-standing MMMs or MMMs on flexible polymer substrates can avoid the use of expensive inorganic substrates, which is a significant advantage towards commercial applications. To surpass the upper bound that is the trade-off relationship of the permeability and the selectivity in conventional polymeric membranes, selecting the suitable combinations of porous solids and polymers for separating molecules is required, which have been studied for decades.[15]

For maximizing the potential of MOF-based MMMs, it is essential to synthesize "ideal" MMMs, and avoid suboptimal structures and non-uniform morphologies (vide supra). In ideal MMMs, gas molecules permeate through the MOF pore and are separated with MOF properties such as size-sieving effects.[16-18] However, suboptimal structures such as "sieve-in-a-cage" or "plugged sieves" and non-uniform morphologies such as particle aggregations often hamper the ideal structure, as discussed in general introduction (**Figure 2**).[17] In these undesired structures, MOF particles cannot control the gas permeation in the membrane. The "sieve-in-cage" scenario and non-uniform morphologies such as particle aggregations often cause critical pinhole defects with a non-selective convection transport, resulting in the significant decrease of the selectivity especially in MMMs at high MOF loadings with

submicron-scale thickness.   On the other hand, in "plugged sieves" structures, the gas molecules cannot enter the pore of the filler, having to circumvent the blocked particles, passing through longer pathway, resulting in the decrease of gas permeability without increasing selectivity.

Therefore, the control of MOF/polymer interface is crucial to achieve defect-free high-MOF loaded MMMs.[16, 19]   By taking advantage of the MOF modification methods discussed in General introduction, the surface functionalization of MOF particles can be readily achieved, which differs from the conventional inorganic particles such as zeolites (**Figure 7**).   Therefore, MOFs are attractive materials to control MOF/polymer interfaces and create the ideal MMMs with high-MOF loading.

Recently, MOF-based MMMs with improved particle dispersibility and the MOF/polymer interface have been reported.   The improvement of MOF/polymer interaction has been achieved with π-π stacking, van der Waals forces, hydrogen bonding and so on.   For example, preparing polymers with hydroxyl groups has reported to introduce hydrogen bonding between MOF/polymer interface.   Another example shows the positive effect of π-π stacking between MOF particles and polymer matrix via introducing the aromatic substituents on the MOF particles.[20-23] Some efforts have demonstrated improved MOF/polymer interaction via polymer grafting on the surface of MOF particles.   The grated polymer can physically interact with polymer matrix, resulting in the improved interaction between MOF and polymer matrix.   For example, MMMs with polymer-grafted UiO-66 (UiO: University of Oslo) type MOFs have been reported; poly(ethylene glycol methacrylate) (PEGMA) was grafted on the initiator-functionalized UiO-66 through controlled radical polymerization (**Figure 1–2a**), poly(methyl methacrylate) (PMMA) was also grafted through glycidyl methacrylate functionalized UiO-66-NH$_2$, and polyimides (PI) brushes was introduced on the surface of UiO-66-NH$_2$ via step growth polymerization (**Figure 1–2b**). [24-26]   In the latter example, the covalently grafting of PI brushes produced the core-shell MOF, showing the PI brush amount was ~12 wt % of the MOF particles (**Figure 1–2b**).[26]   As the selected PI polymer matrix for MMMs was compositionally identical to PI brushes, PI-grafted UiO-66-NH$_2$ showed excellent dispersibility in the PI polymer matrix.   As PI brushes are not covalently crosslinking with polymer matrix, the interaction between PI brushes and polymer matrix is van der Waals force.   The obtained MMMs demonstrated an improved plasticization resistance under CO$_2$ high pressure condition, ductility and an improved gas separation performance for CO$_2$/N$_2$ and CO$_2$/CH$_4$.   However, though this strategy produced MMMs with 43 wt % MOF loadings, clear macrovoids are observed in scanning electron microscopy (SEM)

images, indicating the complete MOF/polymer integration was not achieved.   And the ability to form thin films using this material was not reported.

(a)

(b)
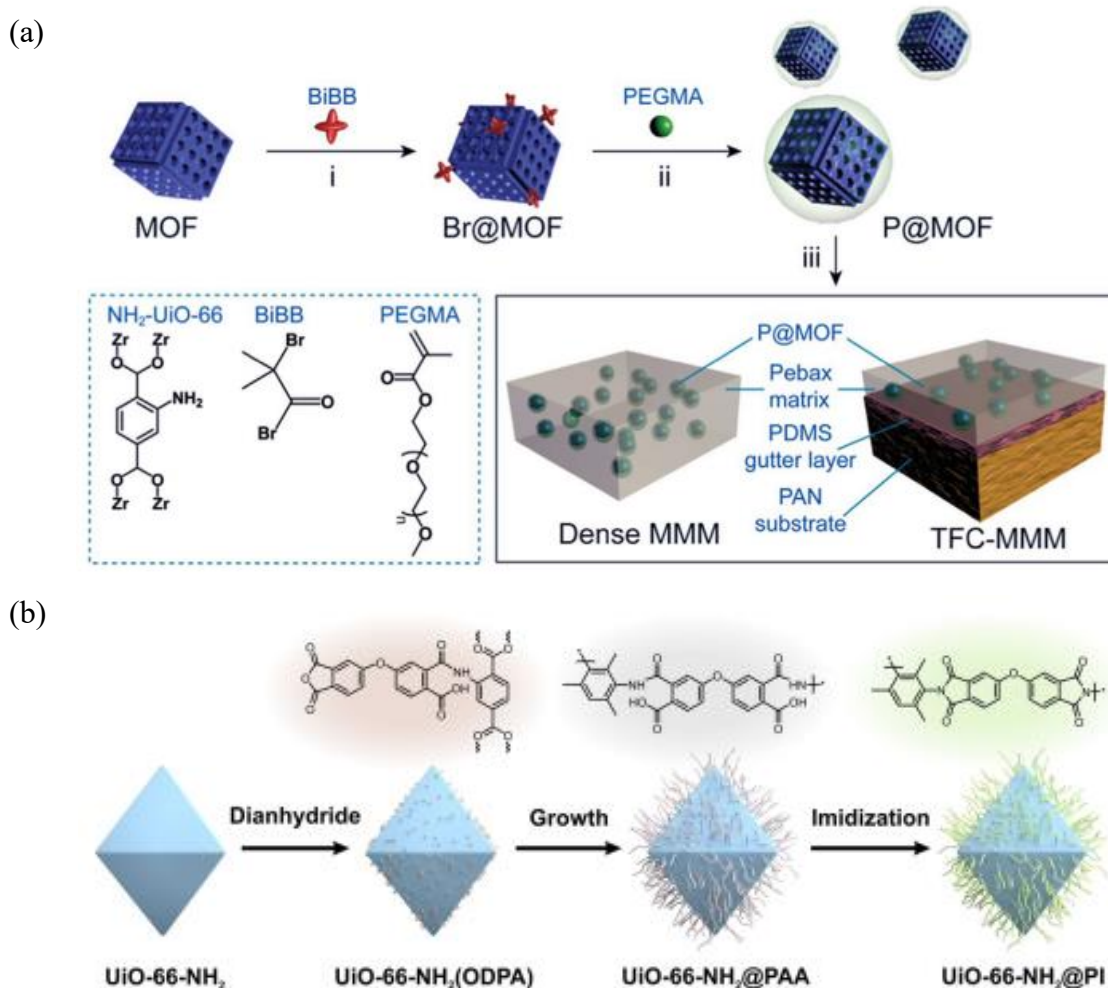
Figure 1−2. Example of MOF-based MMMs with controlled surface properties of MOF particles: (a) MMMs using MOFs grafted with PEGMA thorough surface-initiated atom transfer radical polymerization (ATRP).[24]   (b) UiO-66-NH$_2$ grafted with polyimide, which is used for fabricating MMMs.[27]

To obtain the improved MOF/polymer interaction, several reports have introduced covalent bonds between them using methods such as cross-linking with heat treatment,[28] condensation reactions,[27, 29] photopolymerization,[30-32] in situ cross-linking during polymer synthesis,[25, 33] or ring-opening metathesis polymerization (ROMP).[34]

For example, Gao et al. introduced covalent bonds between MOF and polymer matrix with ROMP as a postsynthetic polymerization (PSP), producing 50wt% MOF loaded MMMs.   The MMMs demonstrated improved gas separation performance for H_2/CO_2 and H_2/N_2 (**Figure 1–3**).[34]   However, SEM images of MMMs show macroscopic voids between the MOF particles, demonstrating the poor dispersibility and the aggregation of MOF particles, which indicates a suboptimal "sieve-in-a cage" morphology.   The 20 wt% MOF-loaded thin MMMs with 5 μm thickness were also fabricated on porous supports, however, high MOF-loaded thin MMMs such as 50 wt % MOF-loaded thin MMMs were not reported.

Yao et al. also reported MMMs with UiO-66 functionalized with imidazolium-based ionic liquids. (**Figure 1–4**).[27]   The covalent linkage was introduced by cross-linking of hydroxy groups of the functional MOF particles and isocyanate groups in polymer matrix of polyurethane oligomers, and the resulting MMMs with 50 wt% MOF loading demonstrated improved selectivity and permeability compared to the polymer-only membranes.   However, the poor permeability of polyurethane polymer matrix caused low permeability of MMMs.
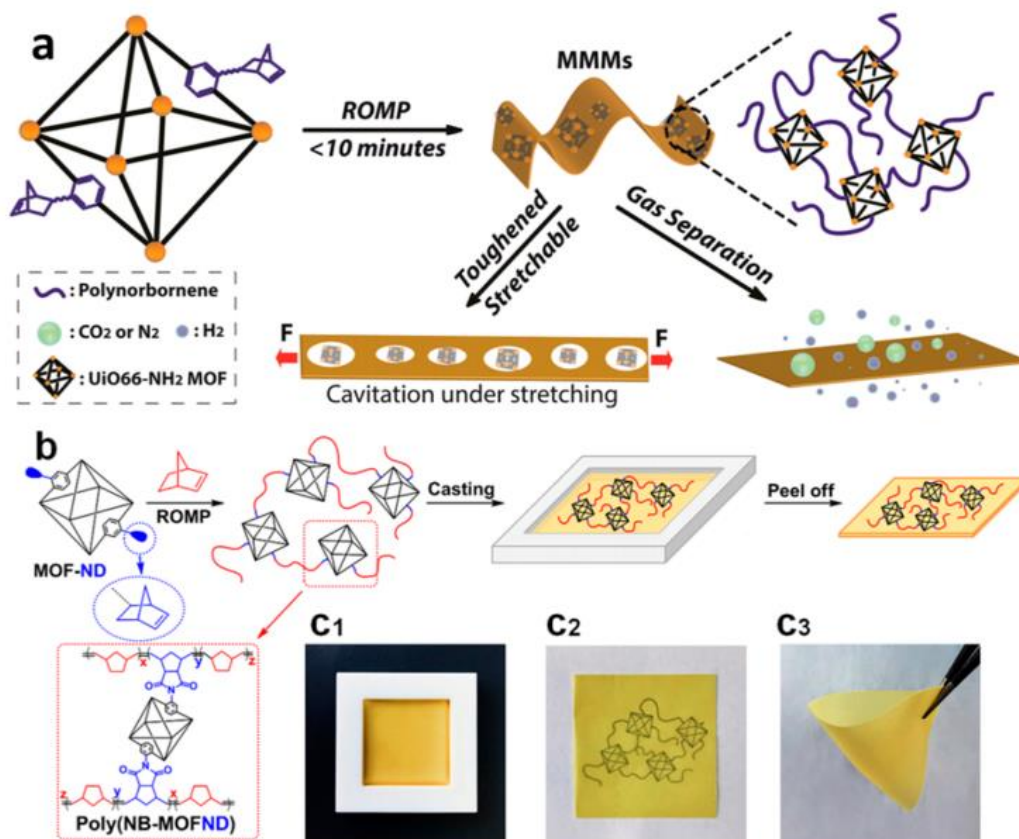
Figure 1–3. (a) MOF-based MMMs synthesized through ring-opening metathesis polymerization (ROMP).　(b) Fabrication of MMMs via ROMP.　(c) Optical images of MMMs.[34]
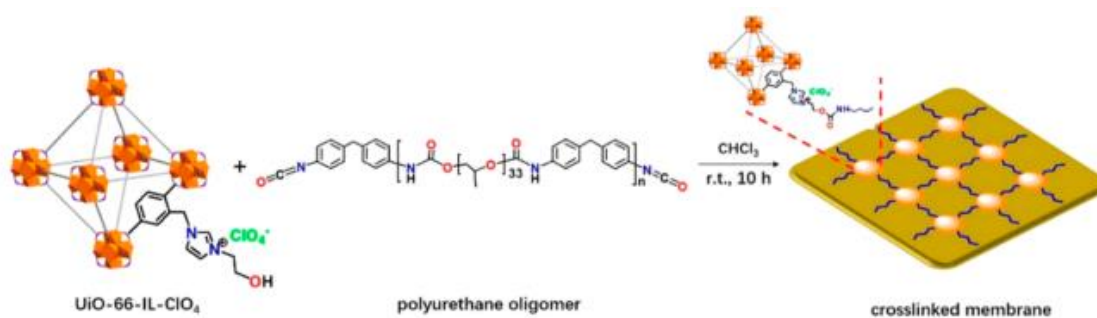
Figure 1–4. Fabrication of covalently cross-linked MMMs with the polyurethane oligomer.[27]

The careful selection of polymer matrix is essential to design high-MOF loaded MMMs for gas separation, because the polymer matrix should have both capabilities of gas separation performance and processability including flexibility. Among a bunch of polymers, poly(dimethylsiloxane) (PDMS) is one of the attractive membrane materials, as this rubbery polymer readily forms flexible thin films with high gas permeability. PDMS is one of silicone polymers having excellent flexibility and the most widely used silicone polymer in practical applications. Therefore, a variety of functional silicones are commercially available, such as PDMS functionalized with acrylate, vinyl, alcohol, hydride, vinyl groups, and branched PDMS and so on, allowing for the diverse ways for the modification (**Figure 1−5**). In rubbery materials including PDMS, condensable gases such as CO_2 can permeate faster than poorly condensable gases such as N_2, resulting in solubility selectivity.[35, 36] Since silicone membranes have already been commercialized for several applications such as organic solvent nanofiltration and gas separation, MMMs with PDMS potentially have an ability to scale. [37, 38]
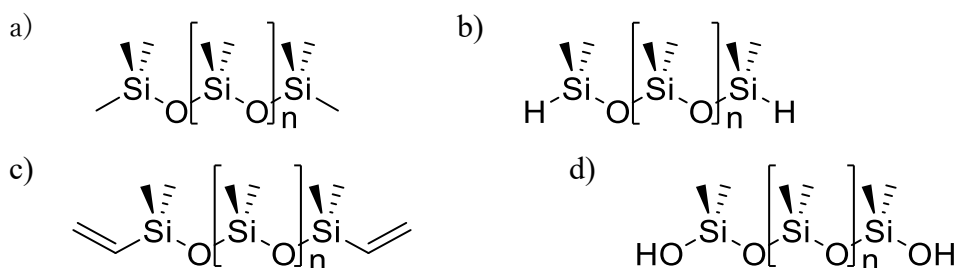
Figure. 1−5 Chemical structure of various PDMSs; (a) trimethylsiloxy terminated PDMS, (b) hydride terminated PDMS, (c) vinyl terminated PDMS, (d) silanol terminated PDMS.

Though there are a number of studies on PDMS MMMs, few studies about MMMs with MOF particles and PDMS have been reported. MOF-PDMS MMMs also suffer from the suboptimal structures like "sieve-in-a-cage" or "plugged sieves" structures and the particle aggregation as with the example of MMMs with other inorganic particles such as zeolites. One of the challenges of MOF-PDMS MMMs is the integration of relatively hydrophilic MOF particles and hydrophobic PDMS polymer matrix. To date, MOF-PDMS MMMs with 40 wt % MOF loading have been achieved using physical mixing method.[39] However, these MMMs demonstrated a decreased selectivity due to the macrovoids derived from the insufficient MOF/polymer interaction. Bae et al. reported MOF-PDMS MMMs with Mg_2(dobdc) (MOF-74(Mg)), fabricating MMMs with 20 wt % MOF loading via physical mixing method.[40] However the MMM demonstrated decreased permeability, indicating the "plugged sieves" suboptimal structure. Therefore, in order to avoid theses undesired structures,

the precise control of the MOF/polymer interface in MOF-PDMS MMMs is required.

In this study, in order to improve MOF/polymer interaction and particle dispersibility and to avoid suboptimal structures and non-uniform morphologies, hydride-terminated PDMS was grafted to the surface of MOF particles, generating core-shell structured MOFs (termed here "corona-MOF"); and the corona-MOF was used to fabricate PDMS MMMs with 50 wt % MOF-loading (**Figure 1−6**). In corona-MOF MMMs, the corona is connected to both MOF particles and PDMS polymer matrix with covalent bonds, acting as a bridge between the MOF particles and polymer matrix, resulting in the strong MOF/polymer matrix connection. Additionally, the PDMS corona is compositionally identical to PDMS polymer matrix, which eliminates any boundary between the corona and the polymer matrix, resulting in an excellent particle dispersion in the polymer matrix. These benefits of corona strategy can generate defect-free high MOF-loaded MMMs. In addition, this corona-MOF MMM avoids "plugged sieves" suboptimal structure due to the steric buffer of the corona, resulting in the improved gas permeability. Although some studies about PDMS-grafted MOF particles have been reported,[41-46] this is the first study that achieved the covalent integration of MOF particles and PDMS polymer matrix, and also the first report about defect-free MOF-PDMS MMMs with 50 wt% MOF loading without any suboptimal structures. Moreover, due to the excellent MOF/polymer interactions and strong MOF/polymer linkage with covalent bonds, flexible MMMs with the thickness of <1 μm was fabricated without macrovoids, which demonstrates the potential of this corona-MOF approach towards thin MMMs for practical applications.
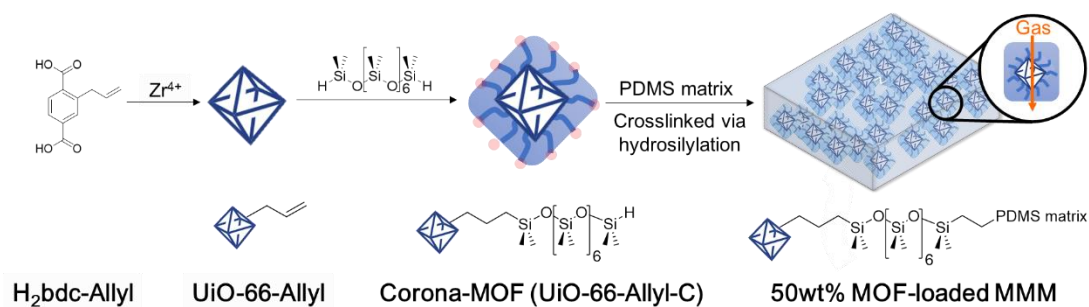
Figure 1−6. Corona-MOF MMMs with PDMS polymer matrix.

Experimental Section

Ligand Synthesis

Starting materials were purchased and used from commercially available suppliers (Sigma-Aldrich, Matrix Scientific, Acros Organics, and others) and used without further purification.

Dimethyl 2-bromoterephthalate (1). Compound **1** was synthesized according to literature procedures (*Inorganic Chemistry* **2011,** *50*, 729-731). Yield: 90 %. ^{1}H NMR (400 MHz, CDCl$_3$): δ 8.31 (d, J = 1.5 Hz, 1H), 8.00 (dd, J = 8.1, 1.4 Hz, 1H), 7.81 (d, J = 8.1 Hz, 1H), 3.95 (d, J = 4.4 Hz, 6H).

2-Allylterephthalic acid (3). To a 250 mL round bottom flask was added compound **1** (7.00 g, 25.6 mmol), tetrakis(triphenylphosphine) palladium (0) (0.59 g, 0.51 mmol, 0.02 eq), and allyltributylstannane (8.74 mL) in 120 mL of toluene. The solution was heated to reflux under N$_2$ for 5 days. After cooling, the reaction solution was quenched using 30 mL of a 4% CsF solution and the obtained precipitate was removed by filtration. The filtrate was extracted with ethyl acetate and dried with magnesium sulfate. The crude product was purified using flash chromatography with silica gel to give the desired product dimethyl 2-allylterephthalate (**2**), which was used for the next reaction without further purification.

To a 500 mL of round bottom flask was added compound **2** in 100 mL of THF and 100 mL of 4% KOH solution. The solution was stirred at room temperature for 24 h. 100 mL of water was added and THF was removed by evaporation, and the aqueous solution was washed twice with hexane. The aqueous layer was acidified to pH ~1 with conc. HCl to precipitate a white solid that was collected by filtration and dried under vacuum to give the desired product (compound **3**). Yield: 81 % (over two steps from **1**). ^{1}H NMR (400 MHz, d$_6$-DMSO): δ 7.97 – 7.83 (m, 3H), 6.18 – 5.81 (m, 1H), 5.16 – 4.98 (m, 2H), 3.78 (d, J = 6.5 Hz, 2H). ESI-MS Experimental: 205.06. Calculated for [C$_{12}$H$_{15}$O$_5$]$^-$: 205.06.

Model reaction for Postsynthetic modification (PSM) (4). To a 3.7 mL vial were added compound **2** (10 mg, 0.043 mmol), hydride terminated polydimethylsiloxane (average M_n ~580, Sigma-Aldrich) (50 mg, 0.085 mmol) and platinum(0)-1,3-divinyl-1,1,3,3-tetramethyldisiloxane complex solution (in xylene, Pt ~2%, 5 μL, Karstedt's Catalyst), in 2 mL of toluene. The capped vial was heated to 100 °C for 30 min in an oven. After cooling to room temperature, toluene was removed by evaporation to give a crude compound **4**. Conversion of the allyl group of dimethyl-2-allylterephthalate was calculated by measuring a crude compound **4** with ^{1}H NMR (400 MHz, CDCl$_3$). The allyl group of crude compound **4** disappeared after the reaction (**Figure 1-9**).

MOF Syntheses

UiO-66-Allyl. **3** (43 mg, 0.21 mmol) and Zirconium(IV) chloride (48 mg, 0.21 mmol) were dissolved in the mixture of 12 mL DMF, 3.6 mL glacial acetic acid and 7.5 μL water in a 20 mL vial. The capped vial was heated to 120 °C for 24 h in an oven. After cooling to room temperature, the particles were collected with centrifugation (fixed-angle rotor, 6500 rpm, 15 min). The particles were washed with 3×10 mL portions of MeOH, and dried under vacuum at room temperature. Yield: 83%. The crystallinity was confirmed by PXRD to be UiO-66 (**Figure 1−9**), and the particle shapes were confirmed by SEM to be octahedral ~300 nm particles (**Figure 1−10**). BET surface area (m^2/g) was measured to be 783 m^2/g. The pore size distribution was measured with N$_2$ at 77 K on a Micromeritics ASAP 2020 (**Figure 1−28**).

UiO-66-Allyl-C. UiO-66-Allyl (200 mg) was dispersed in 20 mL toluene using sonication in an ultrasonic bath for 30 min. Hydride terminated polydimethylsiloxane (average M_n ~580, Sigma-Aldrich, 40 mg) was added to the MOF suspension. The combined suspension was sonicated for 30 min. Platinum(0)-1,3-divinyl-1,1,3,3-tetramethyldisiloxane complex solution (Karstedt's Catalyst, in xylene, Pt ~2%, 40 μL) was then added to the suspension. The suspension was sonicated for 30 min with an ultrasonic bath, and then the suspension was stirred and the capped vial was heated to 100 °C for 24 h. After cooling to room temperature, the particles were collected with centrifugation (fixed-angle rotor, 6500 rpm, 15 min). The collected particles were washed with 3×40 mL portions of THF, soaked with THF for 24h, and dried under vacuum at room temperature. Yield: 91% based on the UiO-66-Allyl quantity (PDMS quantity was subtracted using the digestion results (**Table 1−1**)). The crystallinity was confirmed by PXRD to be UiO-66 (**Figure 1−9**), and the particle shapes were confirmed by SEM to be octahedral ~300 nm particles (**Figure 1−10**).

BET surface area (m^2/g) was measured to be 734 m^2/g.   The pore size distribution was measured with a Micromeritics ASAP 2020 (**Figure 1−28**).

UiO-66-Allyl+PDMS.   UiO-66-Allyl (200 mg) was dispersed in 20 mL toluene using sonication for 30 min.   Hydride terminated polydimethylsiloxane (40 mg, average M_n ~580, Sigma-Aldrich) was then added to the MOF suspension.   The combined suspension was sonicated for 30 min in an ultrasonic bath.   Then the suspension was stirred, and the capped vial was heated to 100 °C for 24 h in an oven.   After cooling to room temperature, the particles were collected by centrifugation (fixed-angle rotor, 6500 rpm, 15 min).   The collected particles were washed with 3×40 mL portions of THF, soaked with THF for 24 h, and dried under vacuum at room temperature.   Yield: 99% based on the UiO-66-Allyl quantity (PDMS quantity was subtracted using the digestion results (**Table 1−1**)).   The crystallinity was confirmed by PXRD to be UiO-66 (**Figure 1−9**), and the particle shapes were confirmed by SEM to be octahedral ~300 nm particles (**Figure 1−10**).   BET surface area (m^2/g) was measured to be 767 m^2/g.

UiO-66.   Terephthalic acid (35 mg, 0.21 mmol) and zirconium (IV) chloride (48 mg, 0.21 mmol) were dissolved in the mixture of 12 mL DMF and 3.6 mL glacial acetic acid.   The capped vial was heated to 120 °C for 24 h in an oven.   After cooling to room temperature, the particles were collected by centrifugation (fixed-angle rotor, 6500 rpm, 15 min). The collected particles were washed with 3×10 mL portions of MeOH, and dried under vacuum at room temperature. Yield: 83 %.   The pore size distribution was measured using a Micromeritics ASAP 2020 (**Figure 1−28**).

Digestion of MOF particles.   10.0 mg of dry MOF particles were immersed in mixture of 350 μL NaOD solution (40 wt % in D_2O) with bath sonication for at least 3 h.   Next, 350μL of D_2O was added, the residue was removed by centrifugation (fixed-angle rotor, 10000 rpm, 5 min), and collected supernatant was used as the solution for NMR analysis (**Figure 1−11**).

Membrane Fabrication

Mixed matrix membranes (MMMs). In a 20 ml vial, 200 mg of dry MOF powder was dispersed in 5.0 mL of acetone using sonication for 30 min. A mixture of 182 mg of RTV615A and 18 mg of RTV615B in 0.87 mL of toluene was added to the MOF suspension such that the final MOF:PDMS ratio was 1:1 w/w. The combined MOF/PDMS suspension was sonicated for 1 h in an ultrasonic bath. Then acetone was removed by evaporation until the total solution weight was ~1 g, resulting in a MOF 'ink' which consists of MOF, PDMS and toluene. Coatings were prepared on BYTAC substrates (Teflon Resin Surface Protectors, Aluminum Backing, purchased from Saint Gobain Performance Plastics) and a glass plate. The Teflon surface of BYTAC was effective to prevent MMM films from sticking to the substrate. The ink was cast onto BYTAC which was put on the glass plate. Films were formed by bar coating with spacer thickness of 200 μm. The coated films were then heated in an isothermal oven to crosslink the polymer and remove the solvent (at 100 °C for 24h. The thickness of the MMMs prepared this way were ~20-60 μm determined with Mitutoyo Digital Micrometer (0.001 mm resolution, 0-25 mm range, IP 54 standard) and also checked via cross section SEM image. PXRD patterns of these MMMs are shown in **Figure 1−19** and SEM images are shown in **Figure 1−20 − 1−22**.

PDMS membranes for gas separation tests. The mixture of 500 mg of RTV615A, 50 mg of RTV615B, and 250 mg of toluene was cast onto BYTAC substrates. Films were formed by bar coating with 300 μm thickness. Then the coated films were heated to crosslink and remove solvent in an isothermal oven at 100 °C for 24 h. The thickness of the freestanding membrane was ~100 μm. Since thin PDMS membranes are difficult to handle, PDMS membranes were prepared to be thicker than MMMs.

PDMS membrane for DMA. A mixture of 2.13 g of RTV615A, 213 mg of RTV615B, and 4.26 g of toluene was cast into a PTFE evaporating dish purchased from VWR International. The casted solution was then heated and dried to crosslink and remove solvent (60 °C, 24h) using a hotplate, then heated to 100 °C, 24h in an isothermal oven. The thickness of PDMS membranes was 620 μm.

Thin MMMs. 45 mg of dry MOF powder was dispersed in 1 mL acetone using sonication in a 20 ml vial for 30 min. A mixture of 41 mg of RTV615A, 4.1 mg of RTV615B, and 340 mg of toluene was added to the MOF suspension such that the final MOF:PDMS matrix ratio was 1:1 w/w. The combined MOF/PDMS suspension was

sonicated with an ultrasonic bath for 1 h, then the acetone was removed by evaporation until total solution mass was 300 mg, resulting in a MOF 'ink' which consist of MOF, PDMS and toluene.   The ink was cast onto BYTAC to prevent MMM films from sticking to the substrate (**Figure 1–32**).   Films were formed by bar coating with wet film applicator rods No. 4 (AP-JR-04 purchased from Gardco, wet film thickness is 10 μm).   The coated films were then heated to crosslink and remove solvent at 100 °C for 24 h in an isothermal oven.   The obtained thin MMMs were peeled off from the coating substrate with masking tape which reinforced the edge of the thin film for easy handling. SEM images of thin MMMs are shown in **Figures 1–34 – 1–36**.

Characterization

Nuclear magnetic resonance (NMR).   400 MHz Varian FT-NMR spectrometer was used to record proton nuclear magnetic resonance spectra (^{1}H NMR).   Chemical shifts are measured in parts per million (ppm) with a reference of the appropriate solvent peak.

Powder X-ray diffraction (PXRD).   For the analysis with PXRD, ~50 mg of dry MOF powder or 0.5 cm^2 of MMM was put on silicon sample holder.   A Bruker D8 Advance diffractometer was used and PXRD data was collected at room temperature, at 40 kV, 40 mA for Cu Ka (l = 1.5418 Å), with a scan speed of 2 sec/step, a step size of 0.05° in 2θ, and a 2θ range of 2-50°.

Brunauer-Emmett-Teller (BET) surface area analysis and pore size distribution measurement.   Prior to analysis, samples were evacuated on a vacuum line at room temperature overnight.   Then, ~50 mg samples were put to pre-weighed sample tubes and degassed at 105 °C until the outgas rate was less than 5 mmHg on a Micromeritics ASAP 2020 Adsorption Analyzer.   After degassing, the sample tubes were re-weighed to get a mass for the samples.   BET surface area (m^2/g) were measured with N_2 at 77 K with a Micromeritics ASAP 2020 Adsorption Analyzer using volumetric techniques. Pore size distribution data were calculated from the N_2 sorption isotherms at 77K based on N_2-DFT model (density functional theory model, slit pore geometry, regularization=0.001) in the MicroActive software provided from Micromeritics.

Scanning electron microscopy (SEM). MOF particles or MMM films (~3 mm^2) were put on conductive carbon tape attached to a SEM sample holder disk and coated using an Iridium-sputter coating for 8 s. A FEI Quanta 250 SEM instrument was used to measure images with an energy source of 5 kV at a working distance at 10 mm under vacuum.

Dispersibility test of MOF particles. ~7 mg MOF particles were dispersed in 7 mL of toluene. After 30 min sonication, the solutions were allowed to settle and dispersibility was visually confirmed at every various times (**Figure 1−12**).

Contact angle measurements. Contact angle were measured with a CAM Micro (Tantec). The MOF powder (approximately 5-10 mg) was pressed onto a glass plate with another glass plate. A drop of water was slowly dropped on the pressed sample with a microsyringe and then the contact angle was measured (**Figure 1−12**).

Dynamic light scattering (DLS). 10 mg/mL solutions of UiO-66-Allyl, UiO-66-Allyl+PDMS, and UiO-66-Allyl-C in toluene were prepared and hydrodynamic diameters were measured to determine the degree of dispersibility of the particles. The MOF solution of 10 mg/mL MOF particles in toluene was sonicated for 30 min to disperse MOF particles, in pre-cleaned quartz cuvettes prior to analysis. DLS was performed on a Malvern Zetasizer ZS90 (Malvern, UK) at 90° (**Figures 1−13 − 1−15**), and hydrodynamic diameters were obtained from number-averaged weighted calculations from fitting the autocorrelation functions to distribution fits.

Scanning electron microscopy - Energy dispersive X-ray spectroscopy (SEM-EDX). MMMs were adhered to a SEM sample holder disk with conductive carbon tape to measure cross sectional views. To obtain images , an FEI Quanta FEG 250 ESEM instrument was used under vacuum with a 10 kV energy source at a working distance at 10 mm for SEM. Energy dispersive X-ray spectroscopy (EDX) spectra were measured with a 10 kV energy source via the attached Thermo Scientific Pathfinder EDX system (**Figure 1−17, Table 1−2**).

Dynamic mechanical analysis.   Storage moduli data were acquired using Perkin Elmer Dynamic Mechanical Analyzer 8000 (Waltham, MA).   Sample thickness was measured using a Mitutoyo Digital Micrometer (0-25 mm range, 0.001 mm resolution, IP 54 standard).   Measurement areas were approximately 5mm width and 5mm length. Frequency sweeps at 0.1Hz to 35 Hz with strains of 0.05 mm were used.   All samples were run in triplicate and the average of all measurements was shown with error bars calculated as a standard deviation(**Figure 1–23**).   The dynamic elastic modulus, also known as storage modulus, E', is a quantity that describes the resistance of a material to elastic deformation, or more generally is related to the stiffness of a material. Application of a sinusoidal stress, σ, to a material results in a sinusoidal strain response, ε, shifted by a quantity δ, known as the phase angle.   The ratio of the applied stress to strain response gives the complex modulus, E*.   Finally, the storage modulus at any particular frequency, ω, is given by:

$$E'(\omega) = |E^*| \cdot \cos \delta$$

where cos δ represents the real, in-phase, component of the strain response.

Gas separation experiments.   Single gas permeation equipment was used for the gas separation experiments (**Figure 1–7**).   Membrane cells were purchased from EMD Millipore (25 mm In-Line Stainless Steel Filter Holders, the filtration area is 2.2 cm^2). CO_2, N_2, and propane gas tanks were purchased from Sigma-Aldrich.   To measure the thickness of the membranes, a Mitutoyo Digital Micrometer (0.001 mm resolution, 0-25 mm range, IP 54 standard) was used.   Filter paper with 12.5 mm diameter was placed under the membranes.   After setting the membranes, upstream of the membrane was pressurized to the desired pressure (400 kPa for CO_2 and N_2, 80 kPa for propane) and the membranes were stabilized at pressure for at least 3 h.   After checking that the permeability was stabilized, each gas flux was measured at least 5 times at room temperature with a soap-flow meter.   The permeability and selectivity were calculated with averaged flux.   Gas separation data were collected and averaged over at least 3 independent samples (**Figure 1–24**).
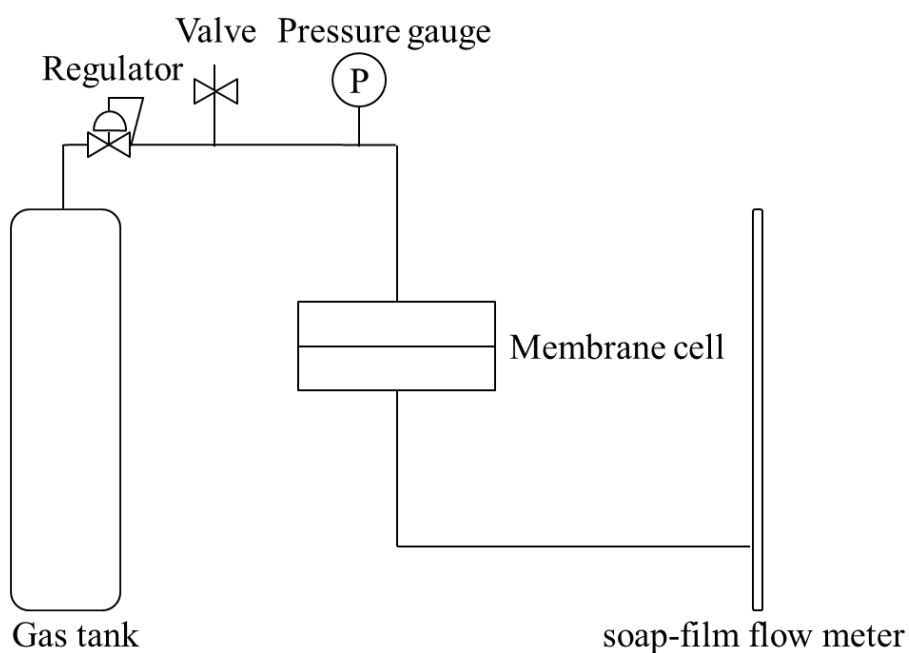
Figure 1–7.   Schematic diagram of the equipment for the single gas permeation test.

Pressure dependent permeation experiment. Single gas permeation equipment was used for the gas separation experiments (**Figure 1−7**). Membrane cells were purchased from EMD Millipore (25 mm In-Line Stainless Steel Filter Holders, the filtration area is 2.2 cm^2). CO_2, N_2, and propane gas tanks were purchased from Sigma-Aldrich. To measure the thickness of the membranes, a Mitutoyo Digital Micrometer (0.001 mm resolution, 0-25 mm range, IP 54 standard) was used. Filter paper with 12.5 mm diameter was placed under the membranes. After setting the membranes, upstream of the membrane was pressurized to the desired pressure (100-400 kPa) and the membranes were stabilized at pressure for at least 3 h. After checking that the permeability was stabilized, each gas flux was measured at least 5 times at room temperature with a soap-flow meter. Gas separation data were collected and averaged over at least 3 independent samples (**Figure 1−25, 1−26, Table 1−4**).

Results and Discussion

As PDMS shows high gas permeability, excellent flexibility, an ability to form thin film, and the potential to scale, PDMS was selected for the polymer matrix. PDMS has been used for fabricating MMMs, however, most efforts about PDMS-MMMs have focused on pervaporation and few studies have reported MOF-PDMS MMMs for gas separation.

Generally, there are two types of cross-linking PDMS: addition-cure PDMS and condensation-cure PDMS. In the case of addition cure PDMS, vinyl-terminated PDMS is crosslinked with a cross-linking agent of hydride terminated PDMS. The reaction proceeds with heating using a platinum catalyst via hydrosilylation reaction. This reaction does not produce any small-molecule byproducts. On the other hand, in the case of condensation-cure PDMS, the reaction needs the atmospheric moisture and tin catalyst, releasing alcohol molecules during crosslinking. For this study, in order to create MOF/polymer covalent bonds, the addition-cure PDMS was selected as the hydrosilylation reaction proceeds with simpler condition. To synthesis corona-MOF particles, UiO-66-Allyl which is UiO-66 derivative having an allyl group in the organic linker was selected (**Figure 1–6**). Because UiO-66 is one of the most widely studied MOFs and shows excellent stability, [47] it is appropriate to evaluate the potential of corona-MOF strategy. Additionally, the high porosity of MOFs including UiO-66 derivatives would increase the permeability of MMMs compared to the polymer-only membrane. Ideally, in order to obtain the size-sieving ability, the pore size of the MOF particle should be between the size of small gas molecules and that of large gas molecules in the gas mixture of interest. As the pore size of UiO-66 (0.6 nm) is too large to show the excellent size-sieving ability against most gas molecule of interest such as CO_2 (0.33 nm) and N_2 (0.36 nm), the derivatives of UiO-66 may not show the desired size-sieving ability.[48] However, UiO-66-Allyl was used to show the potential of the corona-MOF strategy, because this strategy can be applied to other MOF MMMs with MOF particles with better size-sieving ability.[48]

The terminal alkene functionality of UiO-66-Allyl allows for forming the corona-MOF via the reaction with hydride terminated PDMS using hydrosilylation. As hydrosilylation proceeds quickly only using a small amount of Platinum (Pt) catalyst and heat, and avoids the degradation of MOF particles or any side reactions, it is suitable for the "graft-to" method as a postsynthetic modification (PSM). Additionally, as explained in General introduction, the "graft to" method has advantages such as a simple procedure and ability to control the corona size with polymers with

predetermined molecular weight and dispersity, in contrast to "grafting from" techniques.[24, 25]   For the "graft-to" PSM reaction, hydride-terminated PDMS with average molecular weight of Mn ~580 Da (purchased from Sigma-Aldrich) was selected.

The ligand for UiO-66-Allyl, 2-allylterephthalic acid (H$_2$bdc-allyl), was synthesized from 2-bromoterephthalic acid in three reactions with a good yield (**Scheme 1-1**).   The hydrosilylation reaction was checked with a model reaction using hydride-terminated PDMS and dimethyl-2-allylterephthalate with Karstedt's catalyst as a Pt-based catalyst (**Scheme 1-2**).   The hydrosilylation reaction proceeded rapidly (<30 min) confirmed with the conversion of the allyl group of dimethyl-2-allylterephthalate using Proton nuclear magnetic resonance spectra (^{1}H NMR) (**Figure 1–8**).
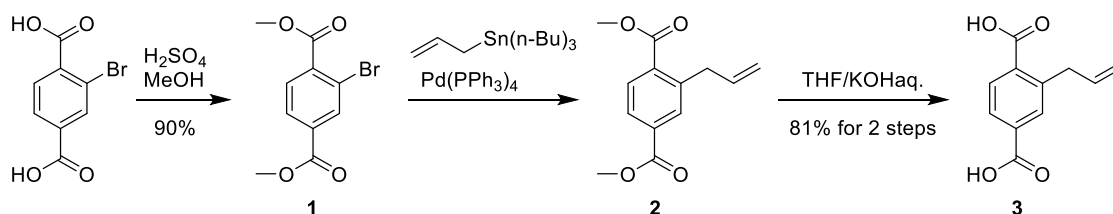
Scheme 1–1.   Synthesis of 2-allylterephthalic acid (H$_2$bdc-allyl).
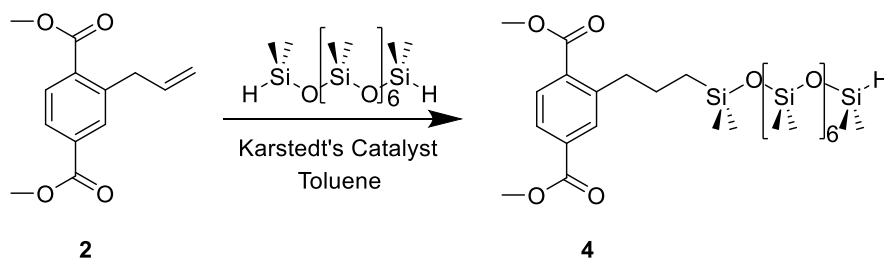
Scheme 1-2.   Model PSM reaction via hydrosilylation.
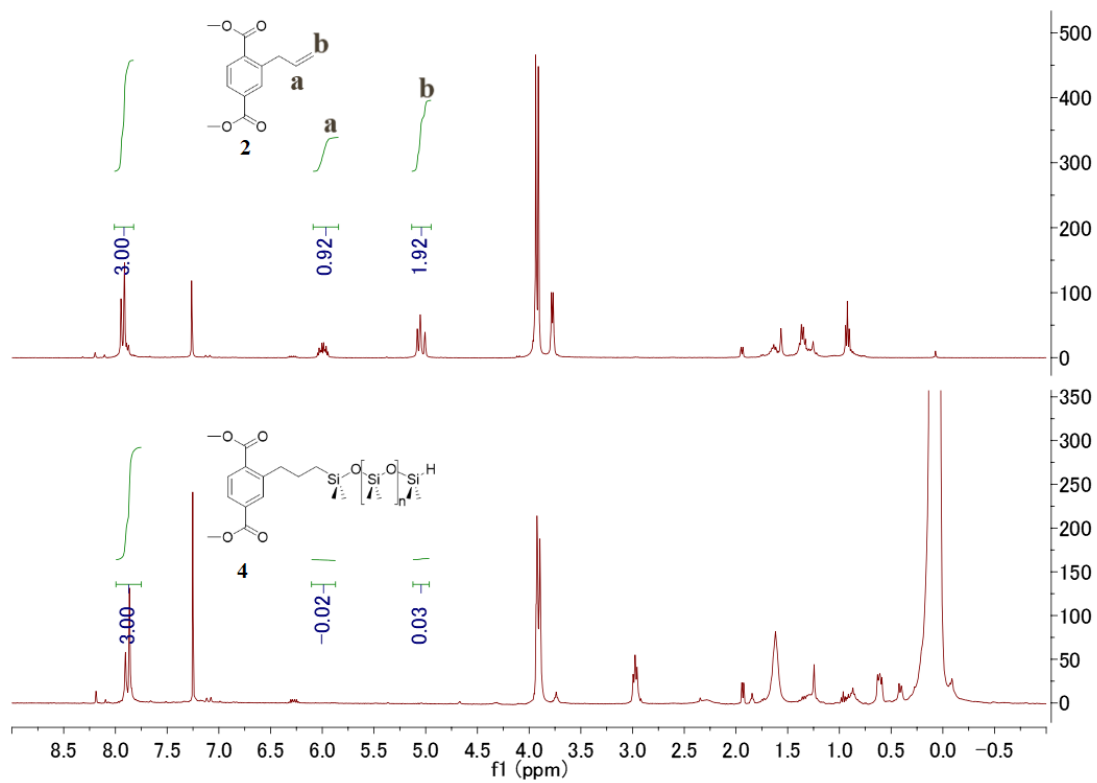
Figure 1–8. NMR spectra of compound **2** and crude compound **4**. Vinyl peaks of **a** and **b** were nearly fully consumed after 30 minutes reaction time.

An allyl-functionalized UiO-66 derivative, UiO-66-Allyl, was synthesized with H$_2$bdc-allyl (1 equiv), ZrCl$_4$ (1 equiv), glacial acetic acid (300 equiv), and water (0.003 equiv) in dimethylformamide at 120 °C for 24 h.[49]   The addition of small amount of water enhanced the formation of UiO-66-Allyl.   As the hydrosilylation reaction was checked to proceed quickly (vide supra), UiO-66-Allyl-C (C = corona) was synthesized with UiO-66-Allyl and hydride-terminated PDMS through "graft-to" hydrosilylation reaction with Karstedt's catalyst as PSM reaction.   In the PSM reaction, as hydride-terminated PDMS possesses two terminal hydride groups, an excess amount of hydride-terminated PDMS was used to avoid the crosslinking between MOF particles.   As there are two hydride groups in the hydride-terminated PDMS, the remained hydride group on the corona in the obtained UiO-66-Allyl-C was still able to undergo additional reactions with vinyl-terminated PDMS in polymer matrix, which results in MMMs with desired covalently connected structures between MOF particles and PDMS polymer matrix.

To elucidate the advantage of the corona strategy, three kinds of MOF particles were prepared: unmodified UiO-66-Allyl, UiO-66-Allyl with PDMS physically attached on the surface of the particles (UiO-66-Allyl+PDMS), and the corona-MOF which consists of MOF particles with covalently grafted PDMS (UiO-66-Allyl-C) (**Table 1–1**).   UiO-66-Allyl+PDMS was synthesized via mixing UiO-66-Allyl and hydride-terminated PDMS without Karstedt's catalyst in order to obtain MOF particles with physically adsorbed PDMS and eliminate any possibility of the formation of covalent bonds between MOF particles and hydride-terminated PDMS.   As the hydrosilylation reaction cannot proceed without Pt catalyst, only a small amount of hydride-terminated PDMS was adsorbed on the surface of the MOF particles after extensive wash to remove remained non-adsorbed polymer, which is a good contrast to corona-MOF of UiO-66-Allyl-C.

Table 1–1. PDMS mass fraction (wt %), contact angle measurement, and Brunauer-Emmett-Teller (BET) surface area of MOF particles.

Material	PDMS wt %[a]	Contact angle (°)	BET (m²/g)
UiO-66-Allyl	-	0	783
UiO-66-Allyl+PDMS	0.70	114	767
UiO-66-Allyl-C	3.81	134	734

[a] (mass of PDMS)/(mass of UiO-66-Allyl + mass of PDMS) × 100, calculated from ^{1}H NMR spectra .

The crystallinity of these MOF particles was measured with Powder X-ray diffraction (PXRD) analysis, demonstrating all three MOFs retained UiO-66-type crystallinity (**Figure 1−9**). N_2 sorption experiments analysis showed the maintained porosities of these MOF particles, which indicates that MOF pores were not completely blocked with hydride-terminated PDMS during the hydrosilylation reaction.   (**Table 1−1**).   SEM images of all three MOF particles showed the octahedral particles with approximately 300 nm particle size, which is a typical UiO-66 particle size and shape (**Figure 1−10**).
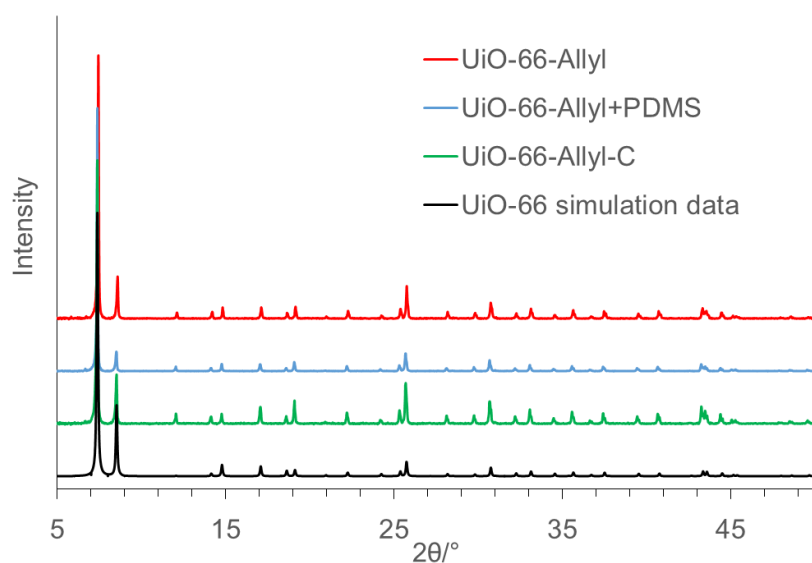
Figure 1−9.   PXRD spectra of UiO-66 (calculated), UiO-66-Allyl, UiO-66-Allyl+PDMS, UiO-66-Allyl-C particles.
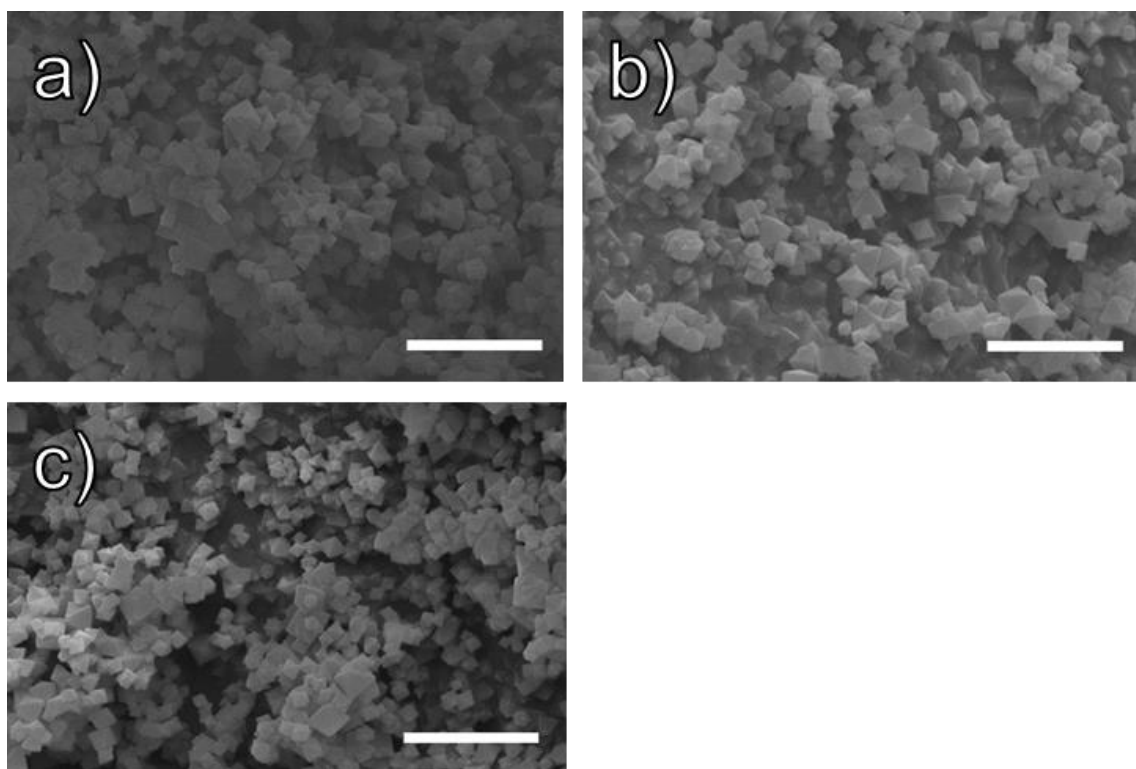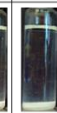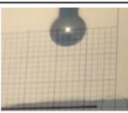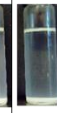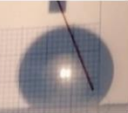
Figure 1–10. SEM images of synthesized MOF particles: a) UiO-66-Allyl, b) UiO-66-Allyl+PDMS, and c) UiO-66-Allyl-C. Scale bars are 2 μm.

The mass fractions of PDMS in these three samples were determined with ^{1}H NMR spectra (**Table 1−1 and Figure 1−11**).   MOF particles were digested using 40 wt % NaOD/D$_2$O solution, and the PDMS mass fraction in each sample was determined by calculating the ratio of the Si−CH$_3$ groups of the PDMS and the aromatic groups of the MOF linkers.   The PDMS mass fraction of UiO-66-Allyl-C was determined to be 3.8 wt %, which is much larger than the PDMS mass fraction of UiO-66-Allyl+PDMS (0.7 wt %), indicating the hydrosilylation using platinum catalyst successfully forms the covalent bonds between hydride-terminated PDMS and the surface of the UiO-66-Allyl during the hydrosilylation PSM reaction.
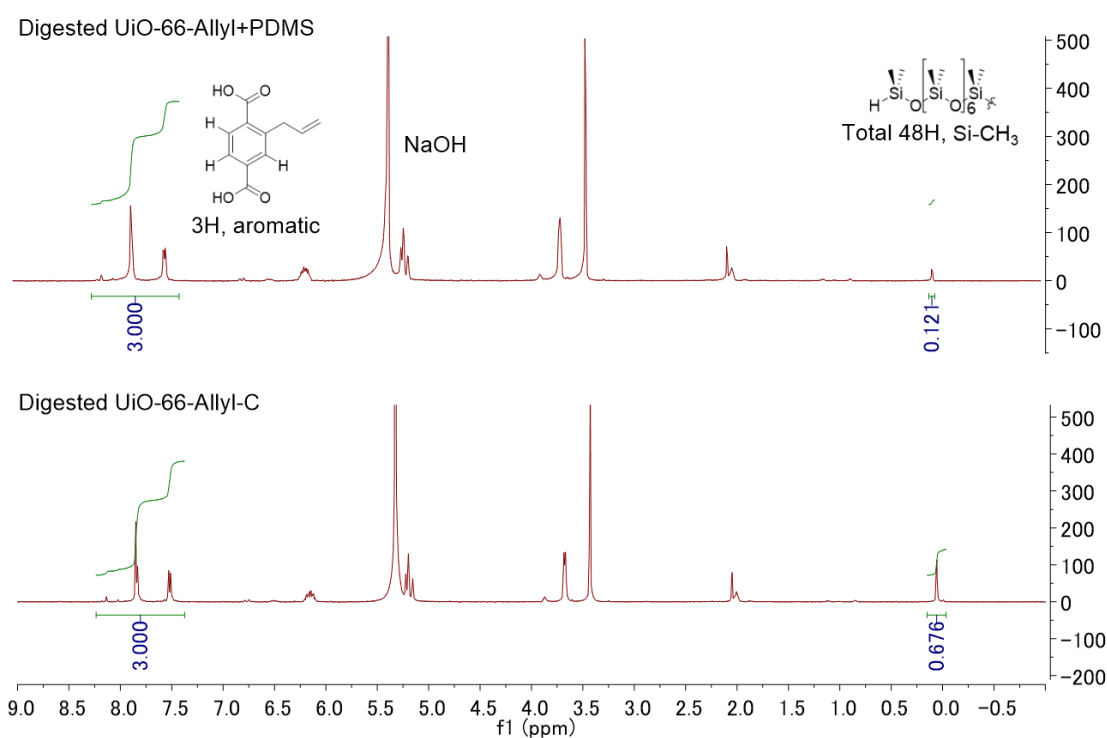
Figure 1−11.   NMR spectra of digested UiO-66-Allyl-C and digested UiO-66-Allyl+PDMS.   The ratio of PDMS and ligands were calculated based on the integral value of 0 ppm of hydrogen peak of dimethyl siloxane group and 7.3-8.25 ppm of aromatic hydrogen peak of H$_2$bdc-Allyl.   PDMS quantity was calculated via the equation: ((Integral value of Si-CH$_3$ / 48) × PDMS molecular weight) / ((Integral value of aromatic hydrogen / 3) × (Molecular weight of UiO-66-Allyl secondary building unit / 6) + (Integral value of Si-CH$_3$ / 48) × PDMS molecular weight)).   PDMS M_n = 580 and molecular weight of UiO-66-Allyl secondary building unit M_n = 1903.64.

As PDMS is hydrophobic polymer, the corona-MOF also displayed excellent hydrophobicity, which results in the greater dispersibility in PDMS polymer matrix and toluene (toluene was used as the casting solvent of MMM fabrications, vide infra). Contact angles of UiO-66-Allyl+PDMS and UiO-66-Allyl-C were measured to be 114 ° and 134 °, respectively; which showed improved hydrophobicity compared to the unmodified UiO-66-Allyl particles (0 °) (**Table 1−1 and Figure 1−12**). Dynamic light scattering (DLS) was measured to evaluate the particle dispersibility and the aggregation in the casting solvent for the MMM fabrication (**Figures 1−13 − 1−15**). DLS measurement demonstrated the hydrodynamic diameter, D_h, of UiO-66-Allyl-C to be 467 nm, which is the reasonable value considering the particle size measured from SEM images (**Figure 1−10**). On the other hand, non-corona MOFs such as UiO-66-Allyl and UiO-66-Allyl+PDMS showed D_h values of 799 and 687 nm, respectively, which indicates the particles formed severe aggregations in the casting solvent. In the dispersibility test (**Figure 1−12**), UiO-66-Allyl-C particles remained well dispersed in toluene for up to 2 days. In contrast, UiO-66-Allyl and UiO-66-Allyl+PDMS particles remained well dispersed for only 10 min and 2 h, respectively. These results clearly show the corona strategy improves the particle dispersibility in the casting solvent. Compared to UiO-66-Allyl-C, less improvement of the hydrophobicity and dispersibility of UiO-66-Allyl+PDMS was observed, suggesting that UiO-66-Allyl+PDMS particles were partially covered with small amount of PDMS via physical adsorption.

MOF particles	Settling time										Contact angle	
	0min	10min	0.5h	1h	2h	5h	1d	2d	4d	7d		
UiO-66-Allyl												0°
UiO-66-Allyl+ PDMS												114°
UiO-66-Allyl-C												134°

Figure 1−12. Dispersibility test in toluene and contact angle measurement of MOF particles.
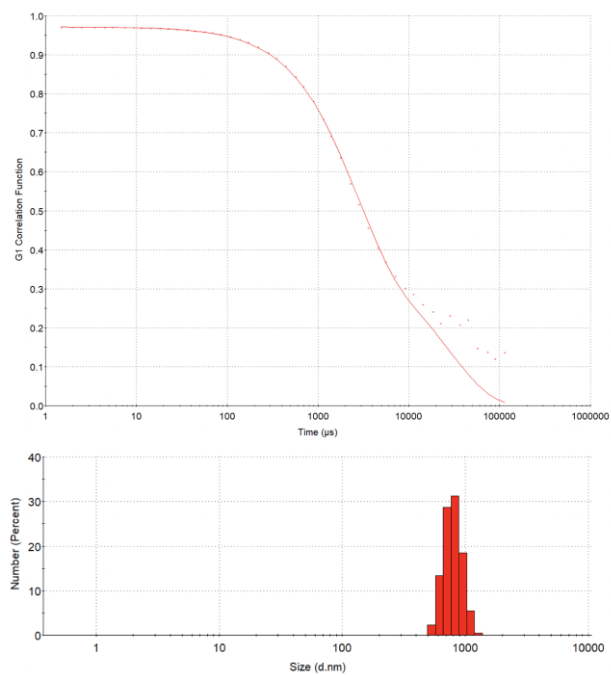
Figure 1−13.   Correlation function and distribution fit (top), and number-average size distribution (bottom) at 90 ° for UiO-66-Allyl.
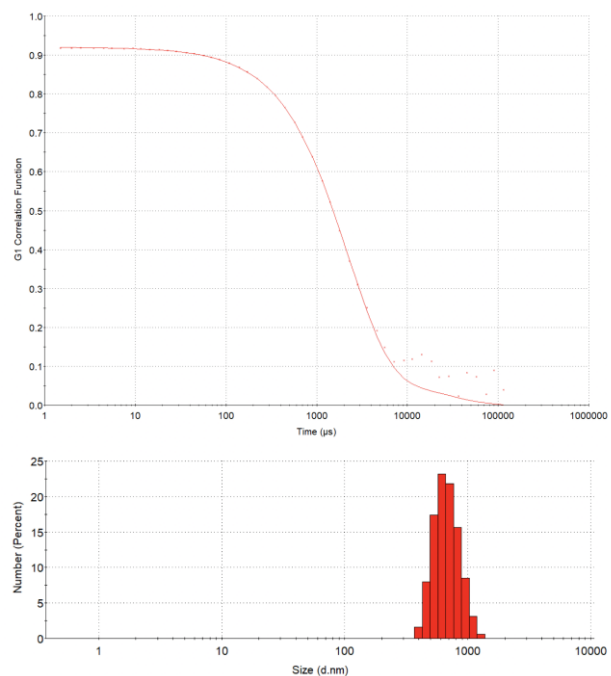
Figure 1−14.   Correlation function and distribution fit (top), and number-average size distribution (bottom) at 90 ° for UiO-66-Allyl+PDMS.
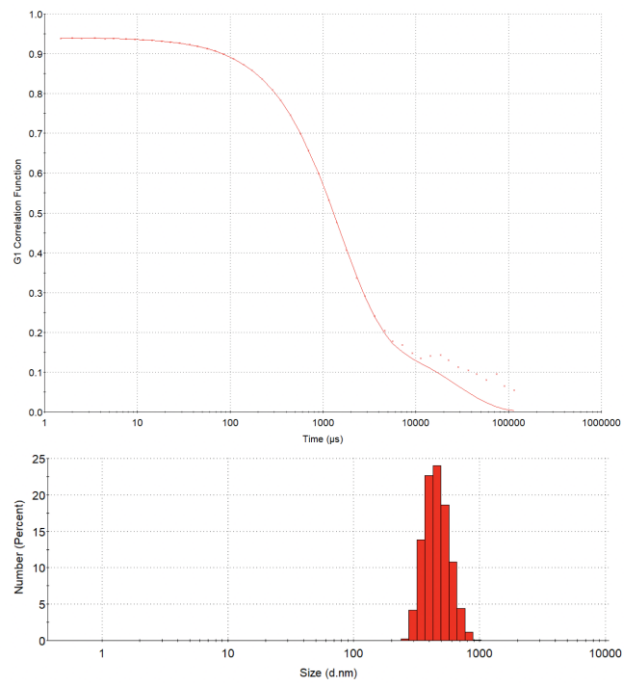
Figure 1–15. Correlation function and distribution fit (top), and number-average size distribution (bottom) at 90 ° for UiO-66-Allyl-C

The corona formation of UiO-66-Allyl-C was verified by calculating the PDMS-grafting density. Based on the particle identification results, it is hypothesized that the grafted PDMS was predominantly localized on the surface of the particles. Average particle facet length of octahedral UiO-66-Allyl-C particle is roughly 300 nm as determined by SEM. The volume of each particle was calculated by (volume of an octahedron):

$$\frac{\sqrt{2}}{3} \times (300 \; nm)^3 = 1.27 \times 10^7 \; nm^3/particle$$

The length of a side of the unit cell of UiO-66 is 2.07 nm based on data from the Cambridge Structural Database. Therefore, the volume of the unit cell is calculated by:

$$(2.07 \; nm)^3 = 8.87 \; nm^3/unit \; cell$$

The number of H_2bdc-Allyl in each unit cell is 24. Therefore, the number of H_2bdc-Allyl in each particle is calculated by:

$$\frac{1.27 \times 10^7 \; nm^3/particle \times 24 \; bdc/unit \; cell}{8.87 \; nm^3/unit \; cell} = 3.44 \times 10^7 \; bdc/particle$$

The mole ratio of PDMS to H_2bdc-Allyl in UiO-66-Allyl-C is 1.41 mol% as determined by NMR (**Figure 1−11**). The number of PDMS chain is calculated by:

$$3.44 \times 10^7 \; bdc/particle \times 0.0141 = 4.85 \times 10^5 \; chain/particle$$

The surface area of each particle is given by:

$$2 \times \sqrt{3} \times 300 \; nm^2 = 3.12 \times 10^5 \; nm^2/particle$$

Therefore, PDMS chain density is calculated by:

$$\frac{4.85 \times 10^5 \; chain/particle}{3.12 \times 10^5 \; nm^2/particle} = 1.56 \; chains/nm^2$$

From the above calculation, the grafting density of PDMS chains on the surface of the UiO-66-Allyl-C particle was calculated to be 1.56 chains/nm^2, which is a reasonable value for "graft-to" reaction with flexible low-molecular weight polymers.[50, 51] Therefore, based on the results of BET surface area, contact angle measurements, dispersibility test and the calculation of chain density, it is reasonable to consider that the grafted PDMS was predominantly localized on the surface of UiO-66-Allyl-C particles.

For the polymer matrix, addition-cure type PDMS (RTV615A/B purchased from Momentive Materials, two-component PDMS) was used, as the flexible films can be readily obtained with RTV615A/B via hydrosilylation using the heat treatment at 100 °C. RTV615A is composed of vinyl-terminated PDMS with a Pt catalyst, while RTV615B is composed of a hydride-terminated-PDMS-crosslinking agent. The vinyl-terminated PDMS and hydride-terminated-PDMS-crosslinking agent are readily crosslinked by heat treatment. To prepare the casting solvent (termed here "MOF-based ink") for fabricating MMMs, MOF particles were dispersed in the solution of 10:1 (wt/wt) of RTV615A and RTV615B in toluene using the reported procedure with slight modification.[52] The MOF-based ink was coated on the substrate with a bar coater, then cured at 100 °C for 24 h and peeled off, producing the flexible self-standing MMMs with 25−60 μm thickness (**Figure 1−16**)[52].

Figure 1−16. Process for formation of MMM.[52] A MOF-based ink is applied to a BYTAC substrate (Teflon resin surface protectors, purchased from Saint Gobain Performance Plastics) on a glass plate by bar coating to create a uniform film. The applied MOF-based ink is heated to cure the RTV615 A/B and remove solvent, producing the MMM on the substrate. MMM film is delaminated from substrate giving a freestanding MMM.

The MOF quantity in MOF-based ink is controlled in order to obtain MMMs with 50 wt % MOF loading, therefore the same quantities of MOF particles and RTV615A/B were used for MMMs fabrication. The actual mass fraction of MOF particles in the MMMs was determined with energy dispersive X-ray spectroscopy (EDX). The atom percent abundances of Si and Zr were measured with the cross-sectional images of MMMs via EDX; and the average values and errors were reported with three different areas (**Figure 1–17** and **Table 1-2**). The PDMS quantities were calculated with the molecular weight of the dimethyl siloxane repeating unit of PDMS and the obtained Si atom percent abundance, while, MOF quantities were calculated with UiO-66-Allyl molecular weight and the obtained Zr atom percent abundance. The MOF contents of each MMM were calculated to be 48.5 ± 0.6, 47.8 ± 0.9, and 46.7 ± 0.7 wt % for UiO-66-Allyl, UiO-66-Allyl + PDMS, and UiO-66-Allyl-C MMMs, respectively.
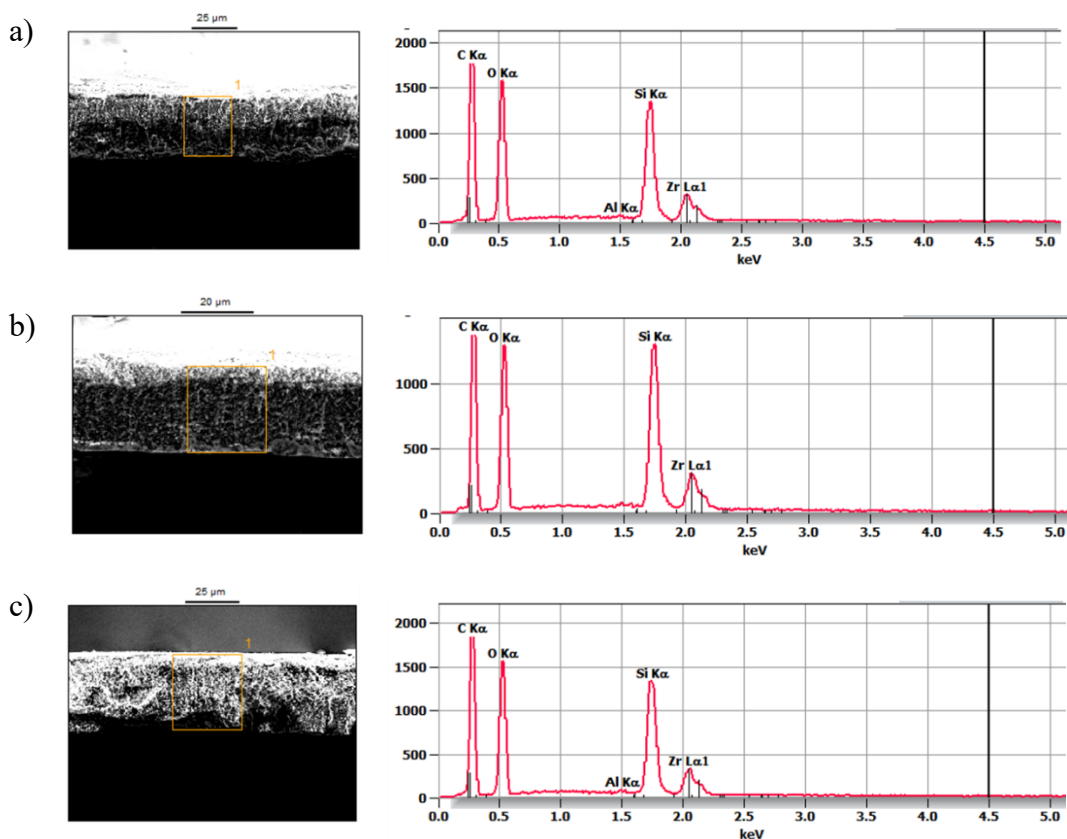

Figure 1–17. EDX of cross section MMMs. a) UiO-66-Allyl MMM, b) UiO-66-Allyl+PDMS MMM, c) UiO-66-Allyl-C MMM. EDX was measured without Ir-sputter coating.

Table 1−2. UiO-66-Allyl contents of UiO-66-Allyl MMM, UiO-66-Allyl+PDMS MMM, UiO-66-Allyl-C MMM calculated via EDX.

	Si	Zr	UiO-66-Allyl content
	atm %	atm %	Wt %
UiO-66-Allyl MMM	30.9	6.8	48.5 ± 0.62
UiO-66-Allyl-PDMS MMM	31.3	6.7	47.8 ± 0.93
UiO-66-Allyl-C MMM	29.4	6.0	46.7 ± 0.69

All three self-standing MMMs including UiO-66-Allyl-C MMM are flexible and easy to handle, showing the rubbery nature of PDMS material (**Figure 1−18**). The retained crystallinity of MOF particles in MMMs were observed via PXRD, while PDMS-only membrane did not show any crystallinity (**Figure 1−19**). BET surface measurements showed that all MMMs possessed low BET surface areas (<15 m^2/g) (**Table 1−3**), which indicates that the most MOF particles are embedded in the polymer matrix. The value of BET surface area is calculated by measuring a physical adsorption of N$_2$ molecules onto the sample surface where known amounts of gas are dosed into the sample under vacuum until ambient pressure is reached. As a subambient pressure is employed in BET surface area measurements, the diffusion of gas molecules in the bulk PDMS polymer is slow in this subambient pressure condition. Therefore, the MMMs embedded with porous particles generally demonstrate low BET surface area, in part, due to the slow diffusion of gas molecules through PDMS polymer matrix. However, in the case of separation membrane, the gas permeation proceeds by taking advantage of the high transmembrane pressure via a solution-diffusion mechanism, where the gas molecules dissolve to the membrane and diffuse using the high transmembrane pressure.[35] Hence, the gas molecules can diffuse the bulk polymer faster with transmembrane pressure compared to the case of BET surface area measurements. Therefore, gas molecules can permeate the polymer matrix and porous particles, even though MMMs shows the low BET surface area.
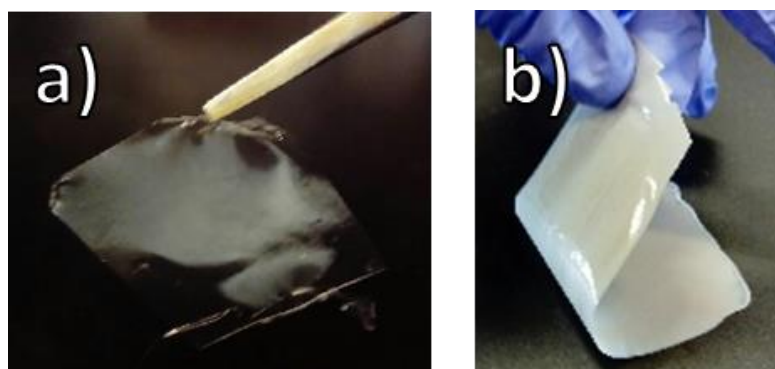
Figure 1–18. Photograph of free-standing membranes: a) PDMS-only membrane, b) UiO-66-Allyl-C MMM with 50 wt % MOF loading.
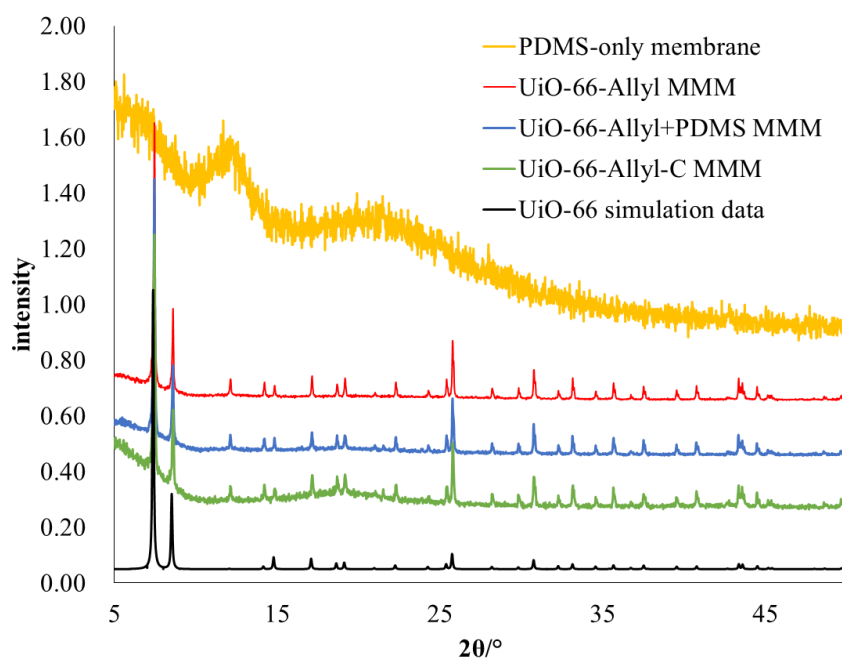
Figure 1–19. PXRD spectra of PDMS-only membrane, UiO-66-Allyl MMM, UiO-66-Allyl+PDMS MMM, UiO-66-Allyl-C MMM and UiO-66 simulation data.

Table 1–3. BET surface area measurements of UiO-66-Allyl MMM, UiO-66-Allyl+PDMS MMM, UiO-66-Allyl-C MMM.

	BET (m^2/g)
UiO-66-Allyl MMM	~14
UiO-66-Allyl + PDMS MMM	~2.5
UiO-66-Allyl-C MMM	<1

SEM images were measured to observe the membrane morphologies. The SEM images of the top side of the MMMs (upper side in MMMs fabrication) show clear macroscopic difference between UiO-66-Allyl-C MMM and other non-corona MOF MMMs (**Figure 1–20**). On the surface of non-corona MOF such as UiO-66-Allly MMM and UiO-66-Allyl+PDMS MMM, a lot of apparent macrovoids are observed between particles and polymer matrix, due to the insufficient control of MOF/polymer interaction and the particle aggregation. On the other hand, no macrovoids are observed in UiO-66-Allyl-C MMMs, which indicates the strong MOF/particle adhesion and the excellent particle dispersibility. Additionally, UiO-66-Allyl-C MMM displayed much better particle dispersibility in the polymer matrix compared to the reported studies about high MOF-loaded PDMS MMMs, which also supports the advantage of the corona-MOF strategy.[53, 54]
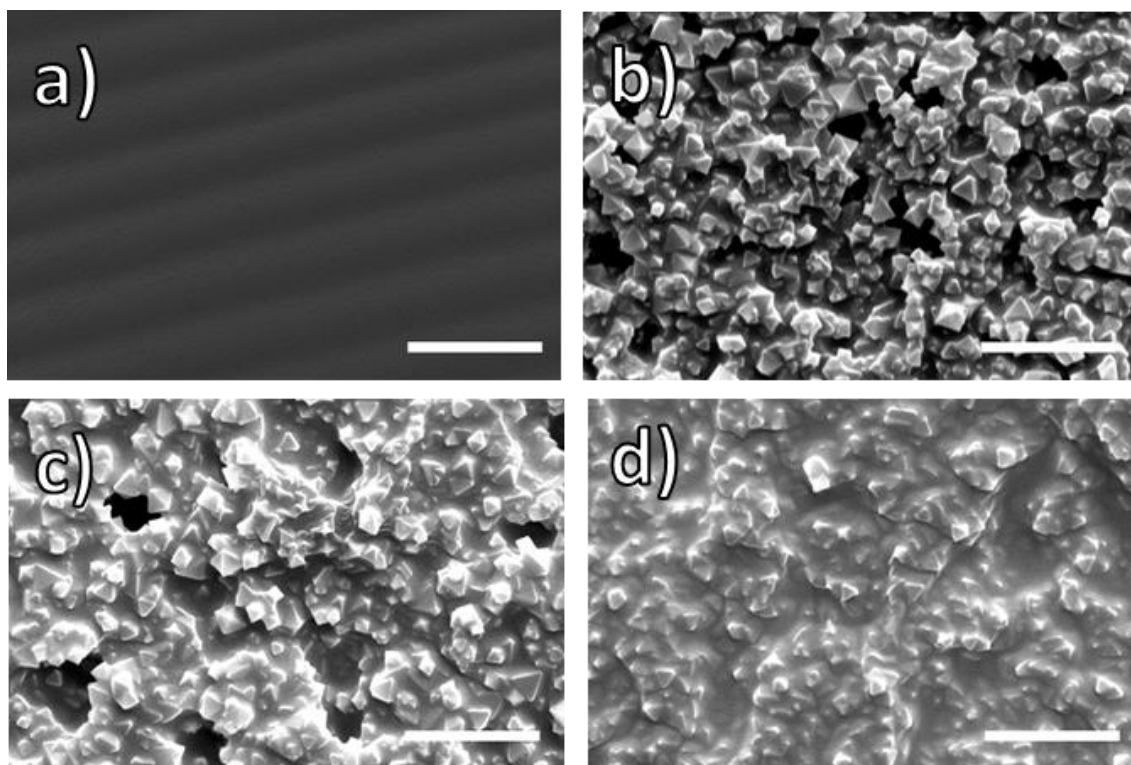
Figure 1–20. SEM images of the top side of MMMs: (a) PDMS-only membrane, (c) UiO-66-Allyl MMM, (d) UiO-66-Allyl + PDMS MMM, (e) UiO-66-Allyl-C MMM. All MOF-loadings are ~50 wt %. Scale bars are 2 μm.

Additionally, the bottom-side SEM images (side facing the substrate in MMMs fabrication) and cross-sectional SEM images also show the clear macroscopic differences between three MMMs.   The obvious macroscopic voids are observed on the bottom side of UiO-66-Allyl MMM (**Figure 1−21**), which can be the fatal defects causing the serious decrease of the selectivity in gas separation.   Small voids are also observed in the cross-sectional SEM images of UiO-66-Allyl MMM and UiO-66-Allyl+PDMS MMM (**Figure. 1−22**).   In contrast, UiO-66-Allyl-C MMM demonstrates the best MOF/polymer compatibility and the particle dispersion, showing no macrovoids.
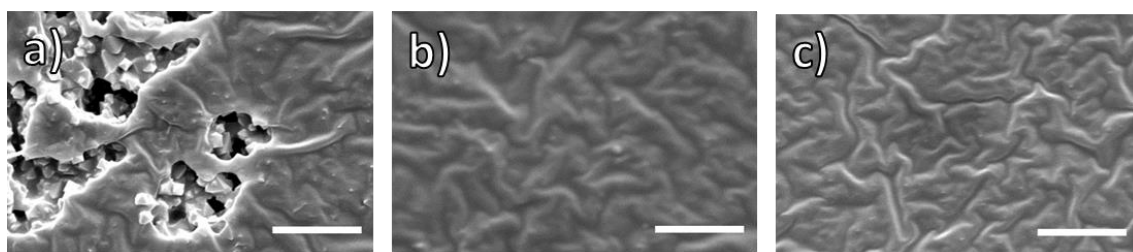
Figure 1−21.   SEM image of bottom side of the MMMs: (a) UiO-66-Allyl MMM; (b) UiO-66-Allyl+PDMS MMM; (c) UiO-66-Allyl-C MMM.   Scale bars are 2 μm.
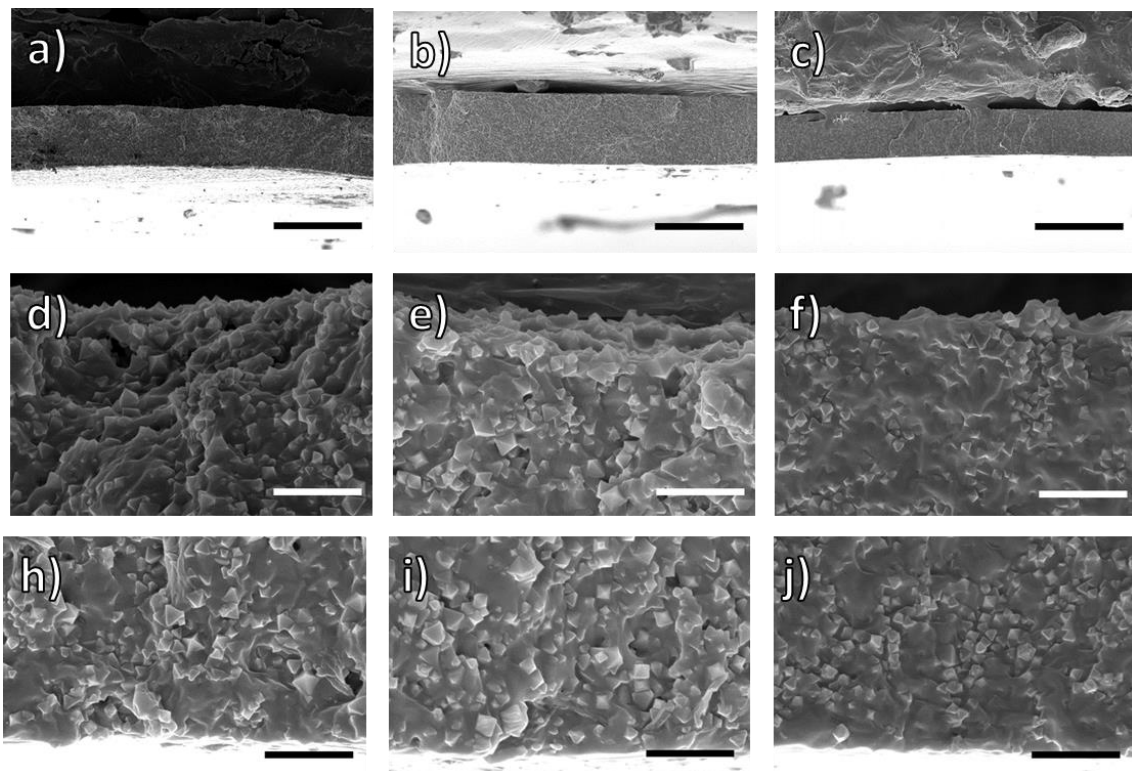
Figure 1–22. (a-c) Cross-sectional SEM images of MMMs: (a) UiO-66-Allyl MMM; (b) UiO-66-Allyl+PDMS MMM, (c) UiO-66-Allyl-C MMM. Scale bars are 50 μm. (d-f) SEM enlarged view of MMM cross sections (top side of membrane): (d) UiO-66-Allyl MMM; (e) UiO-66-Allyl+PDMS MMM; (f) UiO-66-Allyl-C MMM. Scale bars are 2 μm. (h-j) SEM enlarged view of MMM cross sections (bottom side of membrane): (h) UiO-66-Allyl MMM; (i) UiO-66-Allyl+PDMS MMM; (j) UiO-66-Allyl-C MMM. Scale bars are 2 μm.

In order to elucidate the covalent crosslinking of corona-MOF and PDMS polymer matrix, the mechanical properties of the MMM was measured with dynamic mechanical analysis (DMA) (**Figure 1–23**).   The storage modulus of a PDMS-only membrane was 1.60 ± 0.17 MPa.   While, the storage moduli of MMMs were measured to be 25.65 ± 0.96, 26.85 ± 2.93, and 36.91 ± 2.42 MPa for UiO-66-Allyl, UiO-66-Allyl + PDMS, and UiO-66-Allyl-C MMMs, respectively, which are much higher than that of the PDMS-only membrane.   The introduction of MOF particles to the polymer matrix dramatically enhanced the moduli of the MMMs, which is a typical trend when reinforcing polymer blends with inorganic fillers.   Interestingly, the modulus of UiO-66-Allyl-C MMM is 1.4-fold higher than that of non-corona-MOF MMMs such as UiO-66-Allyl and UiO-66-Allyl+PDMS.   This increase suggests the presence of stronger MOF/polymer matrix linkage with covalent bonds, highlighting the benefit of corona-MOF strategy under these analysis conditions.
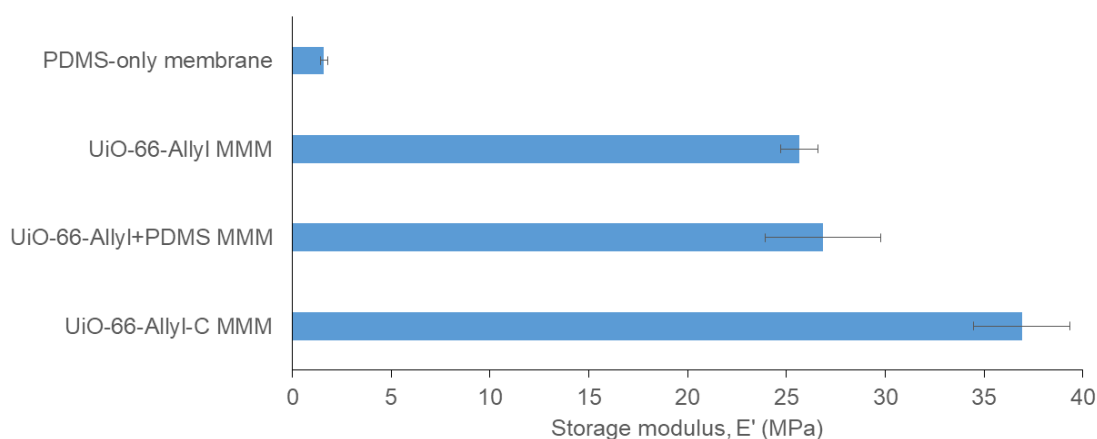
Figure 1–23.   DMA of MMMs. Storage moduli at 1 Hz.

The gas separation abilities such as gas permeability and selectivity were measured with single gas permeation tests to clarify the potential of the MMMs for gas separation membranes. The home-made single gas permeation equipment was prepared with a filter holder, a pressure gauge and a soap-flow meter. Stabilization of gas flux with each membrane was conducted over 3 h and the gas flux was checked five times with soap-flow meter, then the permeability was calculated using the average flux and the membrane thickness. To obtain the average permeabilities and errors, the fluxes of three independently synthesized membranes were measured (**Figure 1−24**). CO_2/N_2 separation ability was measured for the MMMs, because CO_2/N_2 separation has been attracting enormous attention recently to reduce the negative environmental effects of greenhouse gas effects. In addition, as there are other reports about CO_2/N_2 separation with MOF-PDMS MMMs, the CO_2/N_2 separation performance of this study can be easily compared with other MOF PDMS MMMs, revealing the potential and the permeation mechanism of corona-MOF MMMs. In order to determine the ideal CO_2/N_2 selectivity, both CO_2 and N_2 permeability were measured and the ratio of them was calculated . PDMS-only membrane showed a CO_2 permeability of 3013 ± 104 barrer and a CO_2/N_2 ideal selectivity of 10.4 ± 0.9, which are in good agreement with the literature value.[40] UiO-66-Allyl MMMs demonstrated an increased permeability of 20115 ± 9275 barrer, however, the ideal selectivity considerably decreased to be 1.0 ± 0.20. Substantial increased permeability and decreased selectivity to non-selective permeation are good evidences of the presence of non-selective macroscopic voids / pinhole defects which is also observed in SEM images of UiO-66-Allyl MMMs (**Figure 1−20 − 1−22**). UiO-66-Allyl+PDMS MMMs showed decreased CO_2 permeability of 2409 ± 472 barrer, which is lower than the CO_2 permeability of PDMS-only membrane. This decrease of CO_2 permeability indicates the suboptimal structure of "plugged sieves". In this suboptimal structure, the gas molecules need to circumvent the pore-blocked MOF particles and permeate through the longer pathway compared to the PDMS-only membrane, which results in the decrease of permeability. Actually, PDMS MMMs with Mg_2(dobdc) demonstrated the same trend in the reported literature.[40] UiO-66-Allyl+PDMS MMMs also displayed the slight decrease of selectivity to be 8.8 ± 0.7, indicating that there are some small macrovoid defects in the MMMs, which is also supported with SEM images (**Figure 1−20 − 1−22**). Based on these results, the UiO-66-Allyl+PDMS MMMs demonstrate insufficient control of MOF/polymer interface. On the other hand, corona-MOF MMMs with UiO-66-Allyl-C demonstrated improved CO_2 permeability of 4573 ± 727 barrer, while maintained CO_2/N_2 selectivity of 10.0 ± 1.0. The CO_2 permeability was enhanced compared to

PDMS-only membrane, which suggests that the gas molecules permeate the unblocked MOF pore, indicating UiO-66-Allyl-C MMM avoids "plugged sieve" suboptimal structure. Additionally, the maintained selectivity suggests there are no critical pinhole or macrovoids in this membrane, which is also supported the SEM images (**Figure 1−20 − 1−22**). Compared to the previous reports about MOF-PDMS MMMs, the corona-MOF MMMs showed outstanding improvements on the separation performance. Few studies on MOF-PDMS MMM have been reported for gas separations including CO_2/N_2 separation (**Figure 1−24**).[39, 40] For example, Bae and co-workers synthesized 20 wt% MOF-loaded MMMs with $Mg_2(dobdc)$, however, the MMMs showed decreased permeability, indicating the "plugged sieves" suboptimal structure.[40] Another effort on MOF-PDMS MMMS shows the fabrication of MMMs with ~10-40 wt% $Cu_3(BTC)_2$ (BTC = benzene-1,3,5-tricarboxylate) loading, however, 40 wt % $Cu_3(BTC)_2$ loaded MMMs displayed a slight decrease of selectivity probably due to the macrovoids formation between the MOF and polymer matrix, which was derived from insufficient MOF/polymer interaction.[39] In addition, 40 wt % $Cu_3(BTC)_2$ loaded MMMs also showed the decreased CO_2 permeability, indicating the "plugged sieves" suboptimal structure. In contrast, UiO-66-Allyl-C MMM showed the increased permeability and maintained selectivity, preventing the undesired suboptimal structures, which indicates the distinctive advantage of the corona-MOF strategy towards high MOF-loaded MMMs.
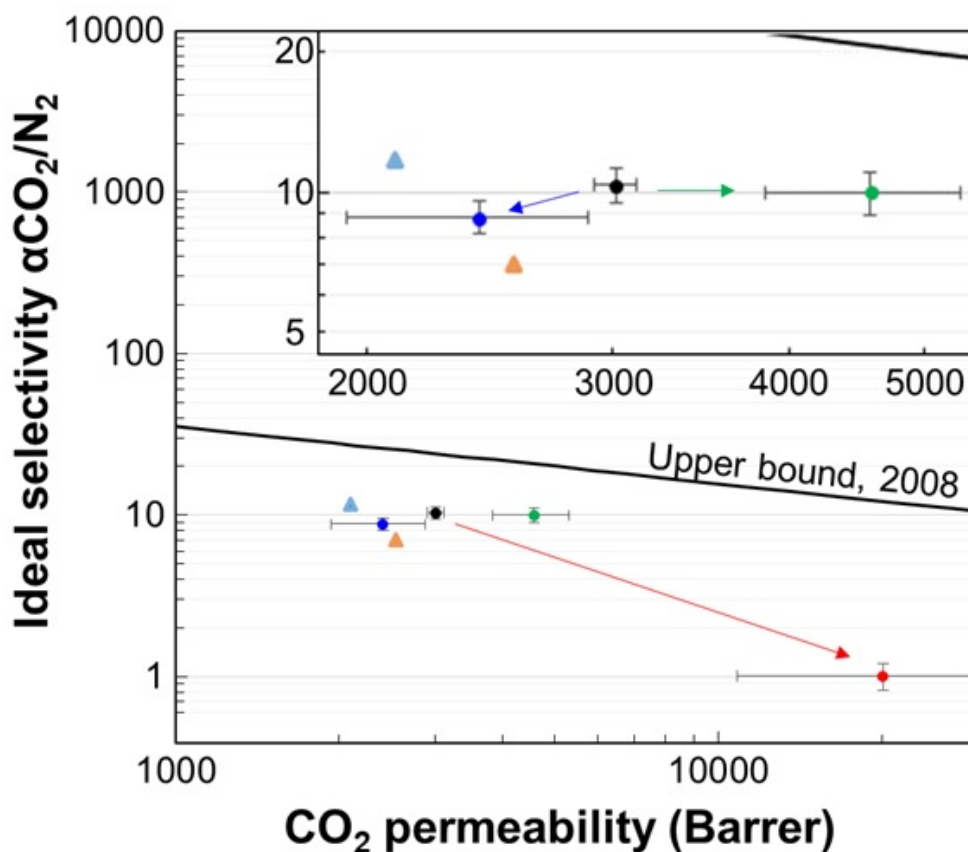
Figure 1–24. CO_2/N_2 separation performance of PDMS-only membrane and MMMs; PDMS-only membrane (black circle), 50 wt% UiO-66-Allyl MMM (red circle), 50 wt% UiO-66-Ally+PDMS MMM (blue circle), 50 wt% UiO-66-Allyl-C MMM (green circle).   Reported literature data; 40 wt% $Cu_3(BTC)_2$/PDMS MMM (orange triangle), 20 wt% Mg_2(dobdc)/PDMS MMM (light blue triangle).[15, 39, 40]   The CO_2 and N_2 flux was measured with CO_2 and N_2 single gas.   The enlarged view is shown in the inset.

To elucidate the transport mechanism of corona-MOF MMMs in detail, pressure-dependent N_2 and CO_2 permeation experiments, propane permeation tests, and the effect of MOF loading were assessed.

First, in order to demonstrate the defect-free MMMs, pressure-dependent N_2 permeation experiments with the feed pressure ranging from 100 to 400 kPa were tested (**Figure 1−25** and **Table 1−4**).   If there are pinhole defects which cause a convection transport, the apparent increase of N_2 permeability would be observed with increasing the feed pressure; because the pressurized N_2 gas would permeate through the pinhole defects with the undesired convection transport.   However, UiO-66-Allyl-C MMM demonstrated the constant permeability even if the feed pressure was increased, which suggests that UiO-66-Allyl-C MMM avoids the formation of the defects.
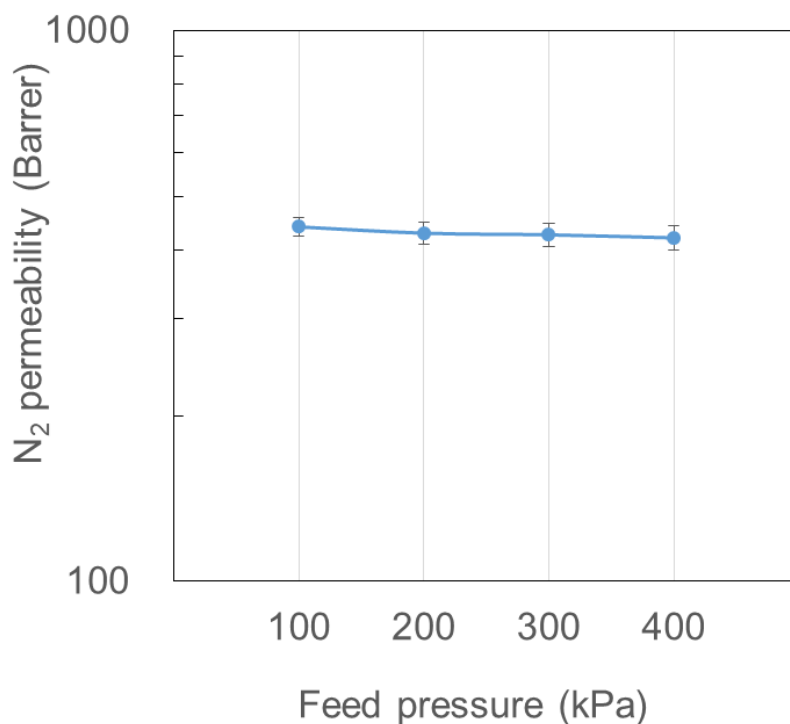
Figure 1−25.   The pressure-dependent N_2 permeation experiment with UiO-66-Allyl-C MMM.

Table 1-4. The pressure-dependent N_2 and CO_2 permeation experiment with UiO-66-Allyl-C MMM.

Feed pressure (kPa)	Feed gas	
	N_2 (Barrer)	CO_2 (Barrer)
100	440±17	4859±99
200	429±20	4390±95
300	426±21	4226±49
400	420±21	4080±59

        To confirm that UiO-66-Allyl-C MMM avoids "plugged sieve" architectures, pressure-dependent CO_2 permeation experiments with feed pressures ranging from 100 to 400 kPa were also tested (**Figure 1–26** and **Table 1-4**). UiO-66-Allyl-C MMMs showed the CO_2 permeability of 4859 ± 99 barrer in 100 kPa feed pressure, while CO_2 permeabilities at increased pressure were decreased to be 4390 ± 95 barrer in 200 kPa, 4226 ± 49 barre in 300kPa, 4080 ± 59 barrer in 400 kPa. This trend that CO_2 permeability of MMMs decreased at higher feed pressure is known as a dual-mode sorption response, which is a combination of the factors of Henry's law and the Langmuir-type sorption response.[55-59] Henry's law is generally applied to a highly gas-soluble rubbery polymer including PDMS, while Langmuir-type sorption response is generally applied to rigid, porous materials such as MOFs. In this case, as MMMs have both nature of the rubbery polymer of PDMS and rigid porous materials of MOFs, Langmuir-type sorption response can be applied to the MOF particles embedded in the polymer matrix. Therefore, at high CO_2 pressure condition, highly soluble CO_2 gas saturates the adsorption site of MOF pores based on the Langmuir-type sorption, which results in the decrease of CO_2 solubility in the MMMs. As the permeability is the product of the gas diffusivity and the gas solubility, the decrease of CO_2 solubility results in the decrease of permeability. These results strongly suggest that the gas molecules certainly pass through MOF pores and the UiO-66-Allyl-C MMMs forms ideal MMMs, preventing the "plugged sieve" structure.
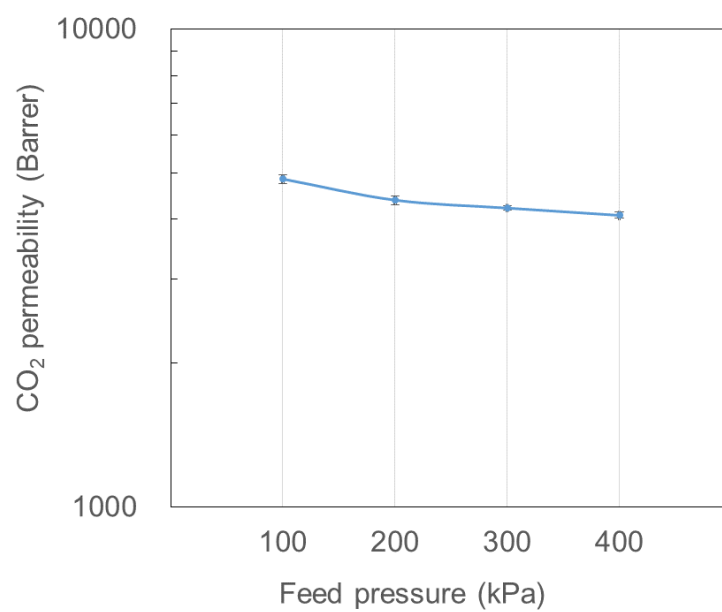
Figure 1–26. CO_2 permeability of UiO-66-Allyl-C MMM with different feed pressures.

In order to elucidate the detailed separation mechanism including size-sieving ability, separation tests with larger molecules were performed (**Figure 1−27**).　Propane gas was selected for the test because the size of propane molecule is 0.49 nm, which is much larger than that of CO_2 (0.33 nm) and N_2 (0.36 nm).　Though the pore size of UiO-66 (0.6 nm) is too large for separating those gases, the pore size of UiO-66-Allyl can be smaller than that of UiO-66 due to the functional allyl groups.　The pore-size distribution measurements also supported the smaller pore size of UiO-66-Allyl compared to the UiO-66 (**Figure 1−28**).　Therefore, UiO-66-Allyl MMMs can possess the size-sieving ability for the separation of smaller gases such as CO_2 or N_2 and larger gases such as propane.　In the results of propane gas permeation test (**Figure 1−27**), UiO-66-Allyl-C MMMs showed the decreased propane permeability of 2830 ± 228 barrer.　As PDMS-only membrane showed the propane permeability of 5822 ± 562 barrer, the permeability of UiO-66-Allyl-C MMM is ~50% that of PDMS-only membranes.　In contrast, N_2 and CO_2 permeability of UiO-66-Allyl-C MMMs increased to be both ~168% and ~168% of PDMS-only membranes, respectively. Therefore, these results suggest that MOF particles can hinder the permeation of the larger gas such as propane and enhance the permeation of smaller gases such as CO_2 and N_2, which clearly indicates the UiO-66-Allyl-C MMMs showed the size-sieving effect and are operated with an ideal MMM morphology avoiding the suboptimal MMM structures.

a)

b)

c)
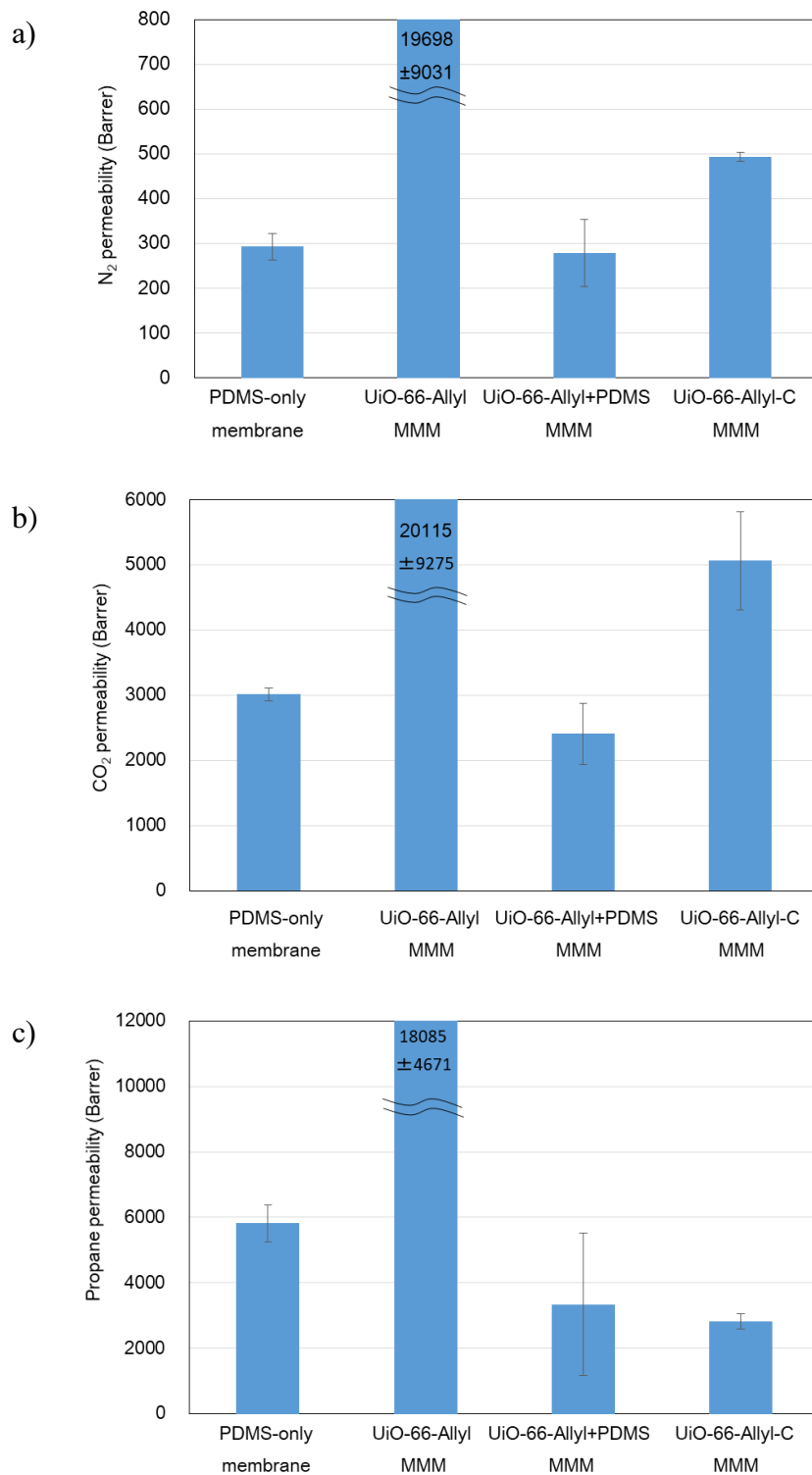
Figure 1–27. N₂, CO₂, Propane permeability of PDMS-only membrane, UiO66-Allyl MMM, UiO-66-Allyl+PDMS MMM and UiO-66-Allyl-C MMM.
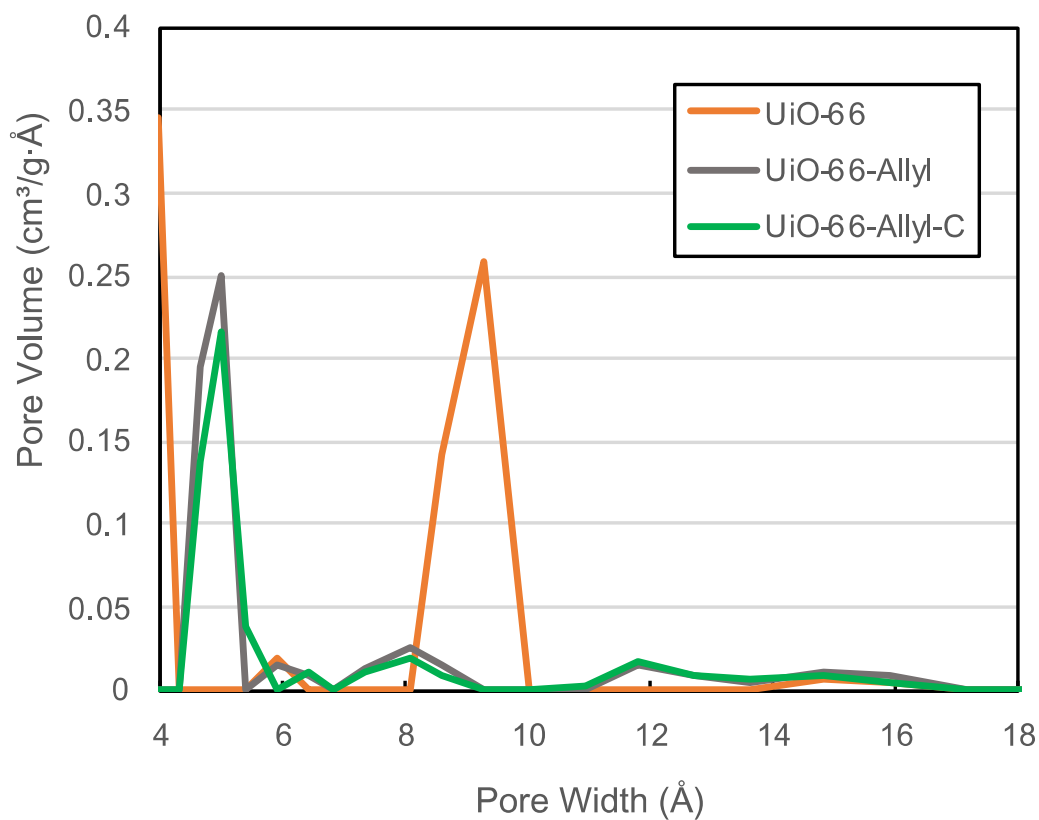
Figure 1–28. Pore size distribution of UiO-66 particles, UiO-66-Allyl particles and UiO-66-Allyl-C particles. Pore size distribution data were calculated from the N_2 sorption isotherms at 77K based on N_2-DFT model (density functional theory model, slit pore geometry, regularization=0.001) in the MicroActive software.

To further clarify the transport mechanism, the effect of MOF loading was assessed by fabricating UiO-66-Allyl-C MMMs with 40 wt % MOF-loading, which is less MOF loading compared to the 50 wt % UiO-66-Allyl-C loaded MMMs.   In the SEM images, 40 wt % MOF-loaded UiO-66-Allyl-C MMMs displayed the good particle dispersibility and no macrovoid defects (**Figure 1−29**).   In the single gas permeation tests, CO_2 and N_2 permeabilities of 40 wt % UiO-66-Allyl-C loaded MMMs were measured to be 3569 ± 169 barrer and 372 ± 42 barrer, respectively, and the ideal selectivity of CO_2/N_2 was measured to be 9.7 ± 1.0 (**Figures 1−30** and **1−31**).   The UiO-66-Allyl-C MMMs with 40 wt % MOF loading demonstrated the lower CO_2 and N_2 permeability compared to UiO-66-Allyl-C MMMs with 50 wt % MOF loading (CO_2 and N_2 permeability of 50 wt % UiO-66-Allyl-C loaded MMMs were 4573 ± 727 barrer and 457 ± 40, respectively).   On the other hand, interestingly, 40 wt % MOF-loaded UiO-66-Allyl-C MMMs demonstrated the larger propane permeability of 4517 ± 211 barrer compared to the propane permeability of 2830 ± 228 barrer in 50 wt % MOF-loaded UiO-66-Allyl-C MMM (**Figure 1−31**).   These trends are reasonable as the separation properties of 40 wt% UiO-66-Allyl-C loaded MMMs are positioned between PDMS-only membrane and 50 wt% MOF loaded UiO-66-Allyl-C MMMs (**Figures 1−30** and **1−31)**.   These results strongly suggest that the UiO-66-Allyl-C has the size-sieving ability, because the incorporation of UiO-66-Allyl-C in the MMMs increases the permeation of the small gases such as CO_2 and N_2 and hinder the permeation of the large gas such as propane.   Additionally, these results also suggest that the MMMs with better gas separation performance can be obtained with MMMs with higher corona-MOF loading.

Collectively, the improved separation performance without the decrease of selectivity, the experimental trends of pressure-dependent N_2 and CO_2 transport experiments, propane permeation tests and the permeability trends of different MOF loading MMMs all strongly support that the corona-MOF strategy can avoid "plugged sieves" and "sieve-in-a-cage" suboptimal structures, showing the benefit for the fabrication of the defect-free high MOF-loaded MMMs with the ideal morphology.
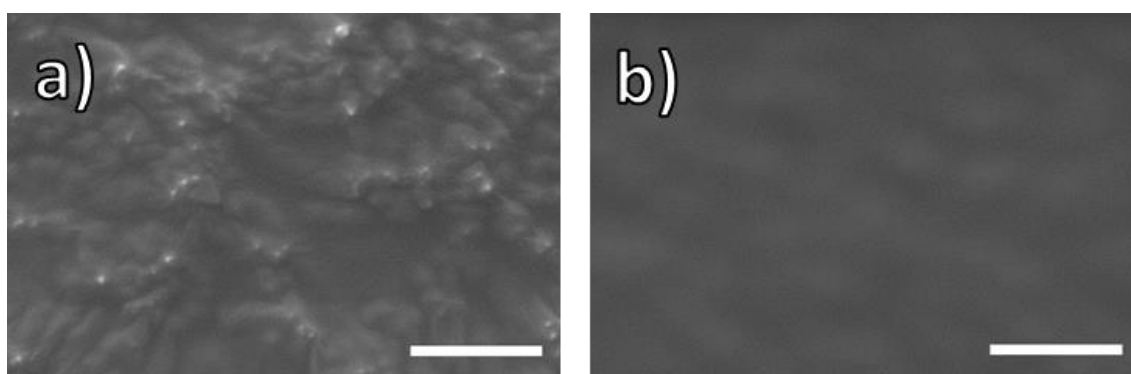
Figure 1–29. SEM image of UiO-66-Allyl-C MMMs with 40 wt % MOF loading:
a) top view, b) bottom view.   Scale bars are 2 μm.
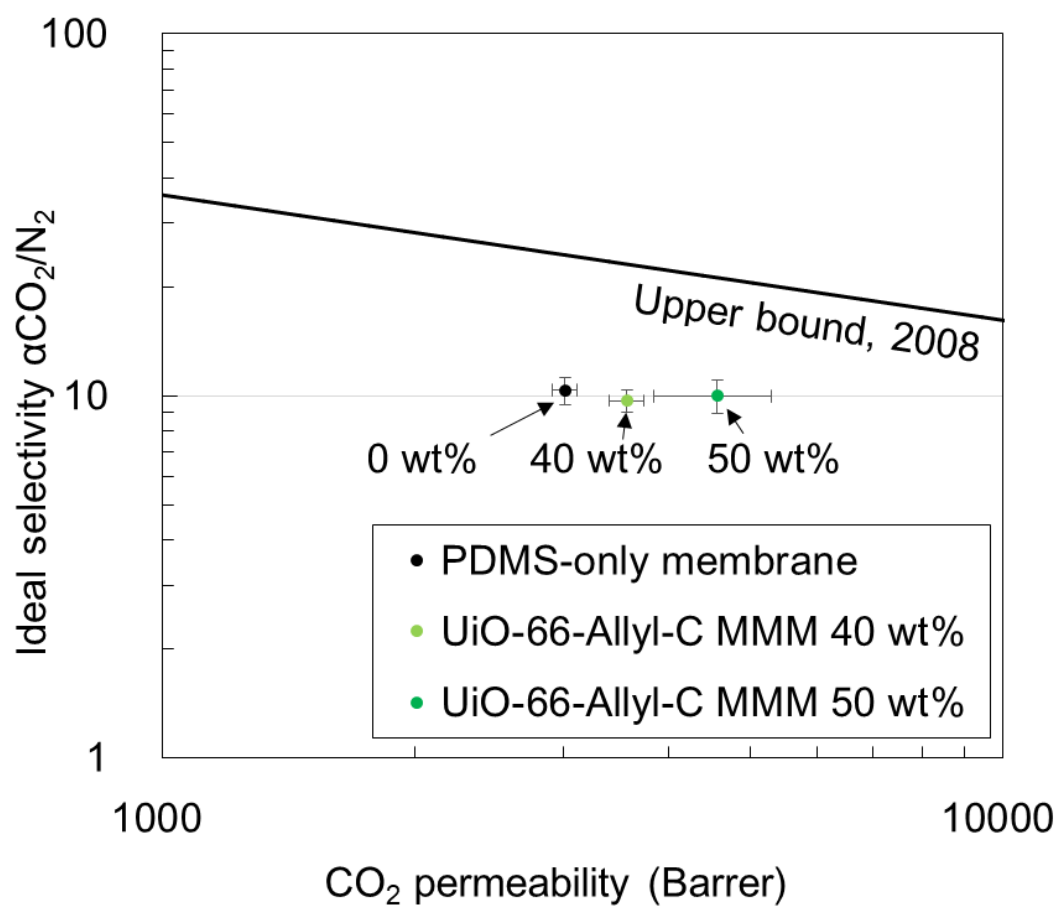
Figure 1–30. Gas permeation measurements of PDMS-only membrane, UiO-66-Alllyl-C MMMs with 40 wt % MOF loading, UiO-66-Alllyl-C MMMs with 50 wt % MOF loading using CO_2 and N_2 single gas.

71
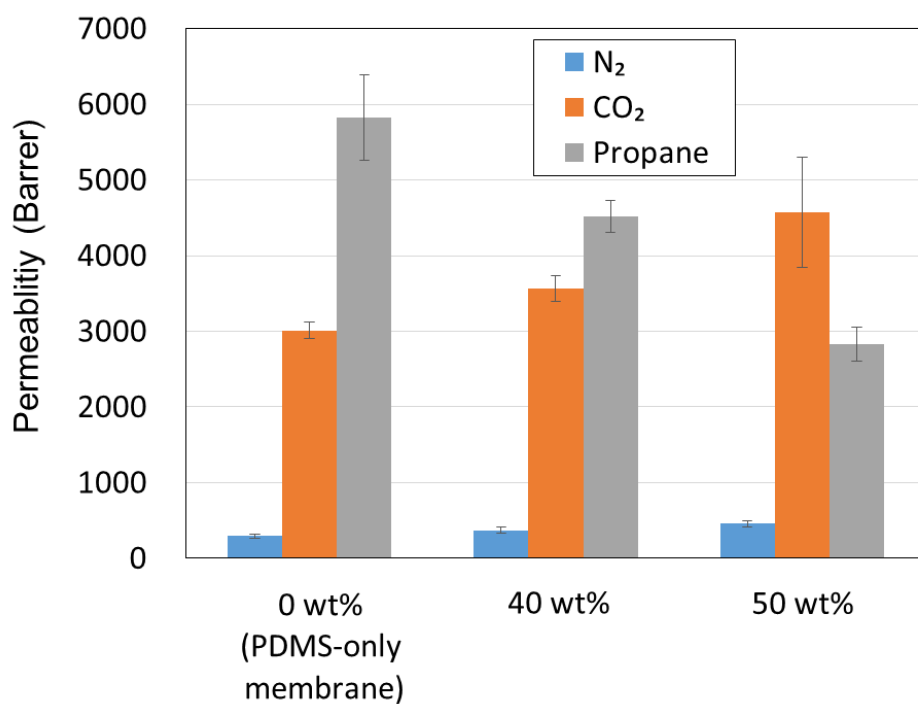
Figure 1–31. The effect of MOF loading; N_2, CO_2, Propane permeability of PDMS-only membrane (0 wt % MOF loading), UiO-66-Alllyl-C MMMs with 40 wt % MOF loading and UiO-66-Alllyl-C MMMs with 50 wt % MOF loading.

Furthermore, in order to show the applicability of this corona-MOF strategy towards the thin film fabrication, 50 wt % MOF-loaded thin MMMs with a thickness of < 3 μm were fabricated (**Figure 1–32**). The MOF-ink was casted on the substrate with the wet film applicator rod, heated at 100 °C, and the edge of the thin MMM was reinforced with masking tape for the easy handling (**Figure 1–33**). The free-standing thin MMMs were obtained via carefully delaminating thin MMMs from the substrates. Thin MMMs with UiO-66-Allyl could not be obtained as the free-standing thin MMMs as it was too brittle to be peeled off from the substrate, even if the masking tape was applied (**Figure 1–33a**). On the other hand, free-standing thin MMMs with excellent flexibility could be obtained using UiO-66-Allyl+PDMS and UiO-66-Allyl-C particles.
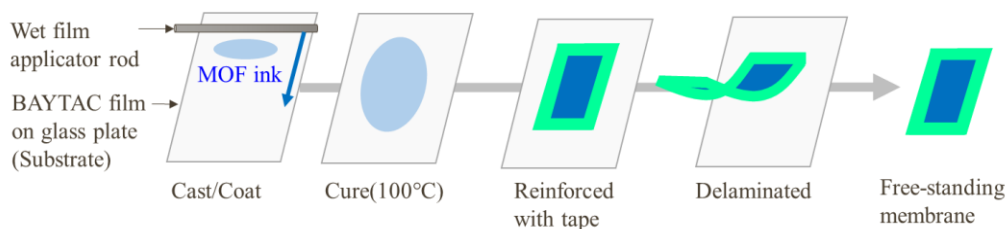
Figure 1–32. Process for formation of a free-standing thin MMM. A MOF-based ink is applied to BYTAC substrates on a glass plate by a wet film applicator rod to create a uniform thin film and heated to cure and remove solvent by evaporation, producing a thin MMM on the substrate. The thin MMM film is reinforced with masking tape and delaminated from substrate giving a freestanding MMM.
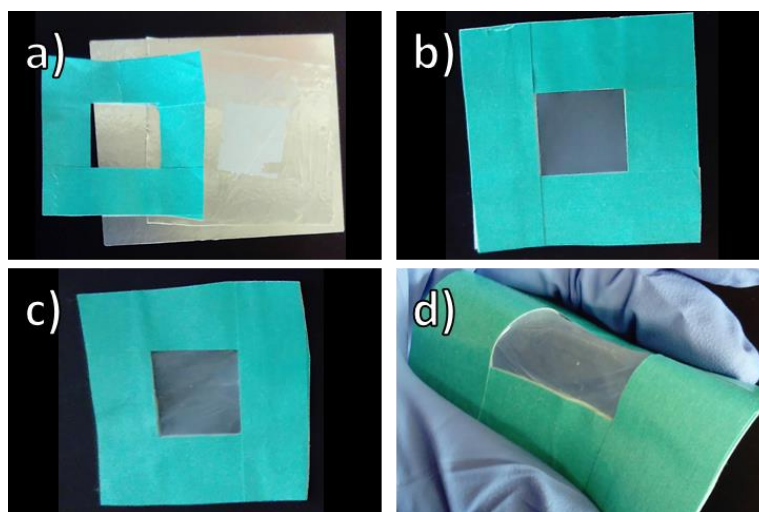
Figure 1–33. Photos of self-standing 50 wt% MOF-loaded thin MMMs: (a) UiO-66-Allyl thin MMM; UiO-66-Allyl thin film was too brittle to be peeled off from the substrate. (b) UiO-66-Allyl+PDMS thin MMM, (c, d) UiO-66-Allyl-C thin MMM. For easy handling, the green masking tape was used to reinforce the thin film.

The SEM images of the top and the bottom view of these MMMs show the clear benefits of the corona-MOF strategy (**Figure 1−34, Figure 1−35**). In the SEM images of UiO-66-Allyl-C thin MMM, there are no apparent macrovoids. On the other hand, there are clear macroscopic voids in the other-MOF thin MMMs. Additionally, in contrast to the UiO-66-Allyl+PDMS thicker MMMs which show no apparent macroscopic voids in the bottom side of the membrane (**Figure 1−21b**), the SEM images of the bottom side of UiO-66-Allyl+PDMS thin MMMs display a lot of clear macrovoids (**Figure 1−35c, d**). As the dimensions of MOF particles are on the order of the membrane thickness, the thin film is susceptible to the void formation. Therefore, it is suggested that physically PDMS-attached UiO-66-Allyl+PDMS MMMs does not have enough MOF/polymer compatibility or particle dispersibility for making defect-free high MOF-loaded thin MMMs. These results clearly show that the formation of the defect-free thin films does not allow any degree of insufficient MOF/polymer interfaces or particle aggregation. In addition, in the cross-sectional SEM images, UiO-66-Ally-C MMM displays the densely packed particles and thin thickness (<1 μm), showing no voids around the particles (**Figure 1−36c**). In contrast, clear macroscopic voids are observed around the MOF particles in the cross-sectional SEM images of other-MOF thin MMMs (**Figure 1−36a, 1−36b**). These results indicate that the good particle dispersibility in the polymer matrix and the controlled particle/polymer matrix interfaces are crucial to fabricate high MOF loaded thin MMMs. The corona-MOF strategies show clear advantages to achieve the thin MMMs fabrication which is important for commercial applications.
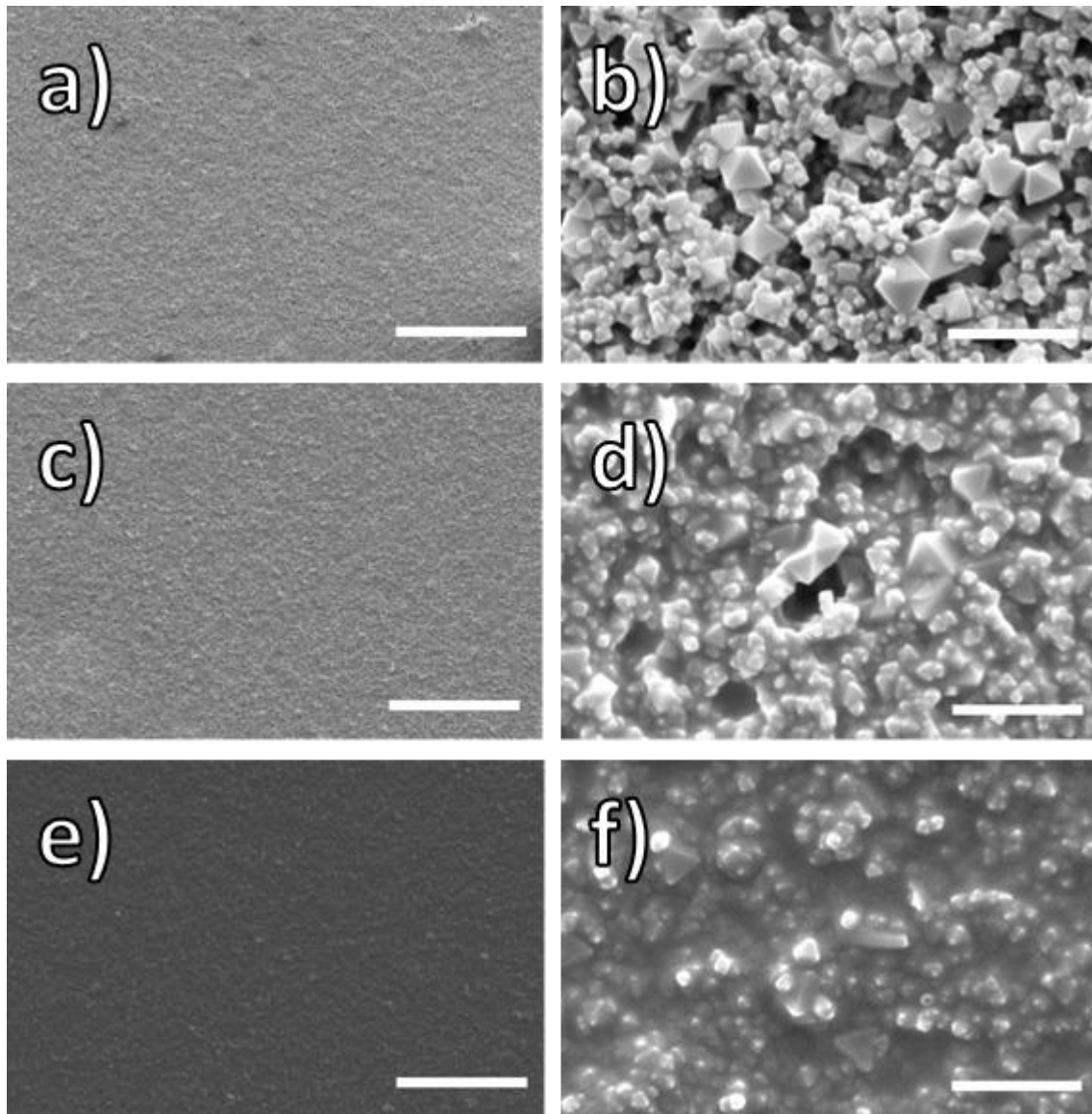
Figure 1–34. SEM images of the top view of thin MMMs at low and high magnification. (a, b) UiO-66-Allyl thin MMM: (a) Scale bar is 50 μm. (b) Scale bar is 2 μm. (c, d) UiO-66-Allyl+PDMS thin MMM: (c) Scale bar is 50 μm. (d) Scale bar is 2 μm. (e, f) UiO-66-Allyl-C thin MMM: (e) Scale bar is 50 μm. (f) Scale bar is 2 μm.
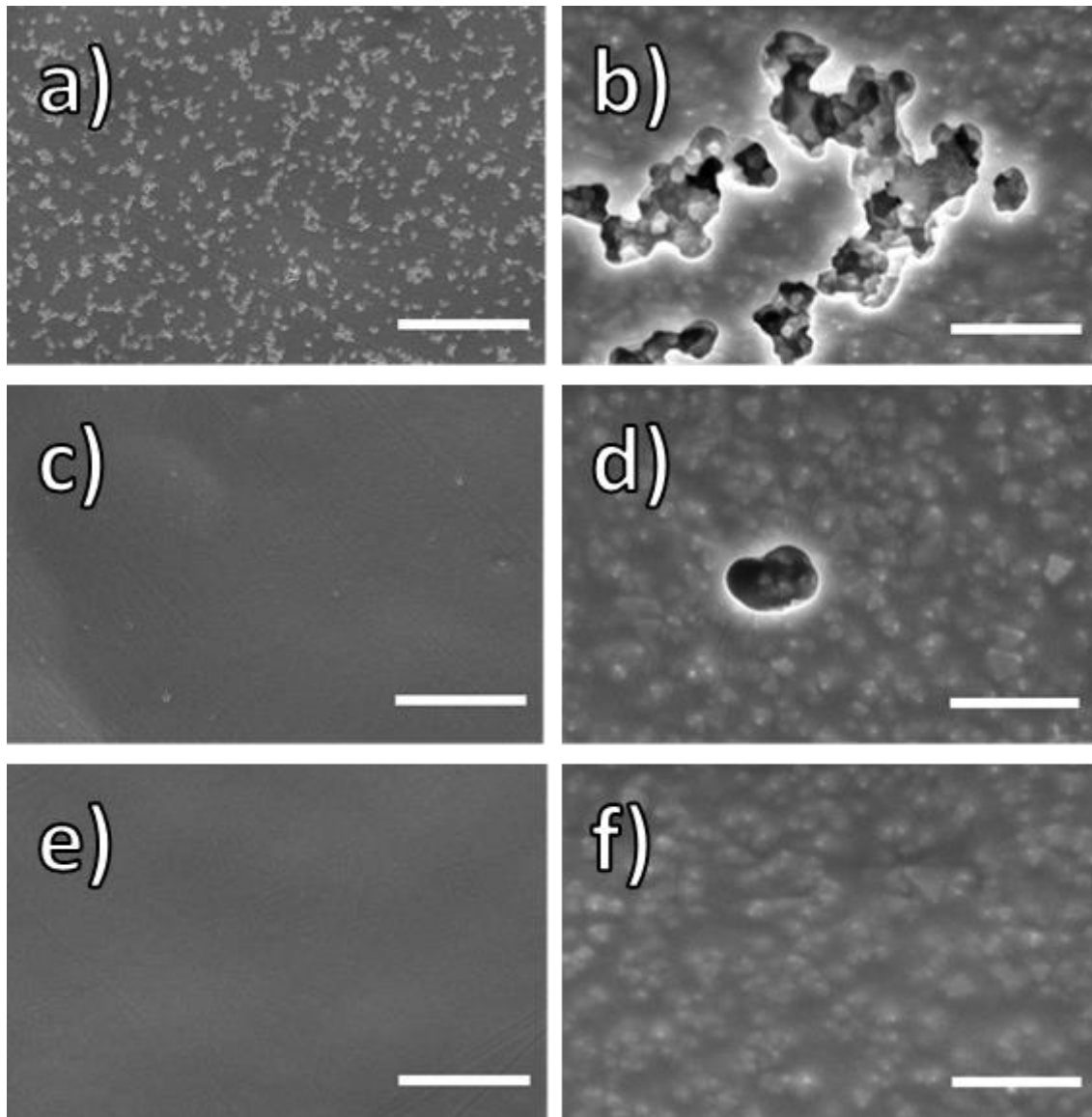
Figure 1–35. SEM images of the bottom view of thin MMMs at low and high magnification. (a, b) UiO-66-Allyl thin MMM: (a) Scale bar is 50 μm. (b) Scale bar is 2 μm. (c, d) UiO-66-Allyl+PDMS thin MMM: (c) Scale bar is 50 μm. (d) Scale bar is 2 μm. (e, f) UiO-66-Allyl-C thin MMM: (e) Scale bar is 50 μm. (f) Scale bar is 2 μm.
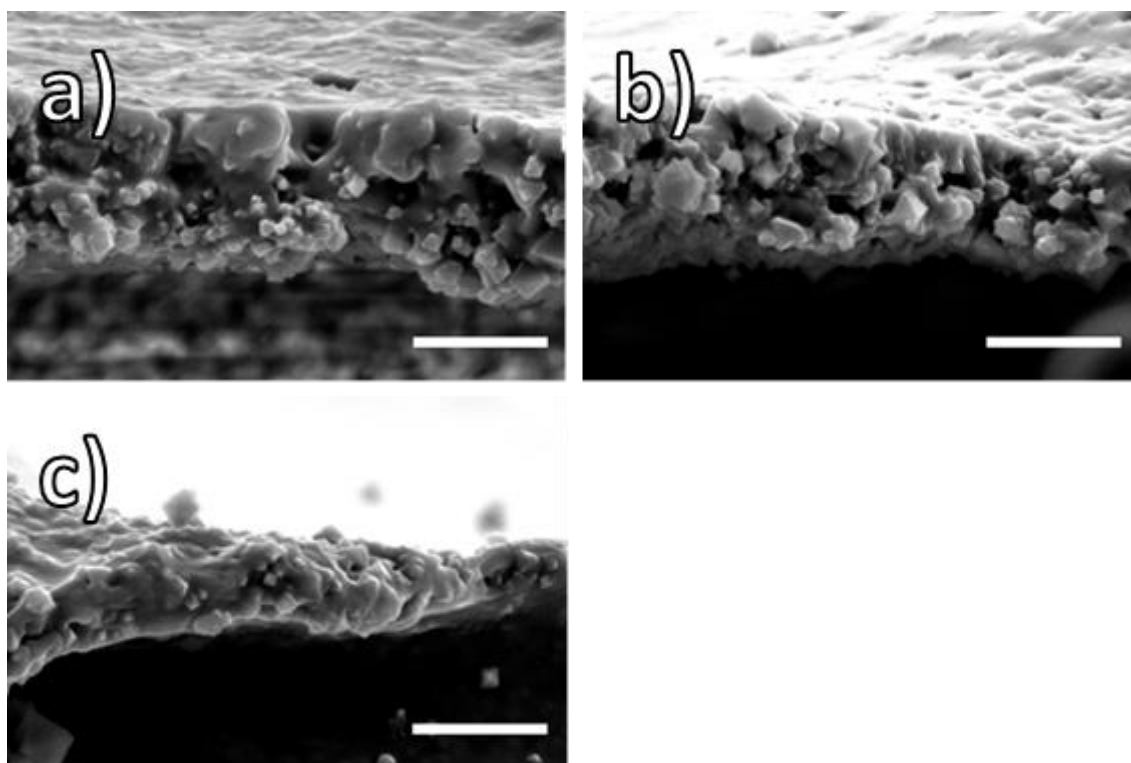
Figure 1–36. SEM images of the cross sectional view of thin MMMs: a) UiO-66-Allyl thin MMM, b) UiO-66-Allyl+PDMS thin MMM, c) UiO-66-Allyl-C thin MMM. Scale bars are 2 μm.

Conclusions

In this study, defect-free high MOF-loaded MMMs with corona-MOF particles and PDMS matrix have been developed.   UiO-66-Allyl-C (corona-MOF) was synthesized via Postsynthetic modification using hydrosilylation with hydride-terminated PDMS ("graft-to" method).   Because the PDMS corona is compositionally identical to the PDMS polymer matrix, corona MOF particles showed excellent dispersibility in the polymer matrix.   Additionally, as the reaction between the corona and PDMS polymer matrix generates the covalent bonds, the MOF particles are connected to polymer matrix with covalent bonds through the corona.   Therefore, the corona MOF showed the good dispersibility in the polymer matrix and the excellent MOF/particle compatibility, which result in the defect-free MMMs with 50 wt % MOF loading.   The free-standing flexible 50 wt % MOF-loaded UiO-66-Allyl-C MMMs demonstrated the improved CO_2 gas permeability without loss of CO_2/N_2 selectivity. The experimental trends of the pressure-dependent N_2 and CO_2 transport experiments, propane permeation tests and the permeability measurements of different MOF loading MMMs support that the corona-MOF MMMs avoid the suboptimal structures such as "plugged sieves" and "sieve-in-a-cage" and achieve the MMMs with the ideal morphology.

Corona-MOF strategy highlights the three advantages over traditional non-functionalized MOF MMMs for fabricating the defect-free MMMs: (1) good particle dispersibility in the casting solvent and polymer matrix; (2) favorable and strong MOF/polymer matrix interaction with covalent bonds; (3) avoiding the pore-blocking of the MOF particles during the MMMs formation.   Importantly, only small amount of the PDMS corona (less than 5 wt %) is necessary for the control of the MOF/polymer interfaces.   Furthermore, free-standing flexible thin MMMs (<1 μm thickness) with no apparent macroscopic voids were achieved using corona-MOF strategy, which shows the potential for the practical applications.   This distinctive corona-MOF strategy for fabricating MOF-MMMs has a potential to be applied to a variety of MOFs.

References

1.   Qiu, S.;   Xue, M.; Zhu, G., Metal–Organic Framework Membranes: From Synthesis to Separation Application. *Chem. Soc. Rev.* **2014,** *43*, 6116-6140.

2.   Denny Jr, M. S.;   Moreton, J. C.;   Benz, L.; Cohen, S. M., Metal–organic frameworks for membrane-based separations. *Nat. Rev. Mater.* **2016,** *1*, 16078.

3.   Furukawa, H.;   Cordova, K. E.;   O'Keeffe, M.; Yaghi, O. M., The Chemistry and Applications of Metal-Organic Frameworks. *Science* **2013,** *341*, 123044.

4.   Sholl, D. S.; Lively, R. P., Seven chemical separations to change the world. *Nature* **2016,** *532* (7600), 435-7.

5.   Zhu, Y.;   Gupta, K. M.;   Liu, Q.;   Jiang, J.;   Caro, J.; Huang, A., Synthesis and Seawater Desalination of Molecular Sieving Zeolitic Imidazolate Framework Membranes. *Desalination* **2016,** *385*, 75-82.

6.   Kwon, H. T.; Jeong, H.-K., In Situ Synthesis of Thin Zeolitic–Imidazolate Framework ZIF-8 Membranes Exhibiting Exceptionally High Propylene/Propane Separation. *J. Am. Chem. Soc.* **2013,** *135*, 10763-10768.

7.   Liu, X.;   Demir, N. K.;   Wu, Z.; Li, K., Highly Water-Stable Zirconium Metal–Organic Framework UiO-66 Membranes Supported on Alumina Hollow Fibers for Desalination. *J. Am. Chem. Soc.* **2015,** *137*, 6999-7002.

8.   Brown, A. J.;   Brunelli, N. A.;   Eum, K.;   Rashidi, F.;   Johnson, J. R.;   Koros, W. J.;   Jones, C. W.; Nair, S., Interfacial Microfluidic Processing of Metal-Organic Framework Hollow Fiber Membranes. *Science* **2014,** *345* (6192), 72-75.

9.   Hou, J.;   Sutrisna, P. D.;   Zhang, Y.; Chen, V., Formation of Ultrathin, Continuous Metal–Organic Framework Membranes on Flexible Polymer Substrates. *Angew. Chem. Int. Ed.* **2016,** *55*, 3947-3951.

10.   Zhang, C.;   Li, Y.;   Wang, H.;   He, S.;   Xu, Y.;   Zhong, C.; Li, T., Adhesive Bacterial Amyloid Nanofiber-Mediated Growth of Metal–Organic Frameworks on Diverse Polymeric Substrates. *Chem. Sci.* **2018,** *9*, 5672-5678.

11.   Shamsaei, E.;   Lin, X.;   Low, Z.-X.;   Abbasi, Z.;   Hu, Y.;   Liu, J. Z.;   Wang, H., Aqueous Phase Synthesis of ZIF-8 Membrane with Controllable Location on an Asymmetrically Porous Polymer Substrate. *ACS Appl. Mater. Interfaces* **2016,** *8*, 6236-6244.

12.   Dechnik, J.;   Gascon, J.;   Doonan, C. J.;   Janiak, C.; Sumby, C. J., Mixed-Matrix Membranes. *Angew. Chem. Int. Ed.* **2017,** *56*, 9292-9310.

13.   Zornoza, B.;   Tellez, C.;   Coronas, J.;   Gascon, J.; Kapteijn, F., Metal

Organic Framework Based Mixed Matrix Membranes: An Increasingly Important Field of Research with a Large Application Potential. *Micropor. Mesopor. Mater.* **2013,** *166,* 67-78.

14.   Denny Jr., M. S.;   Kalaj, M.;   Bentz, K. C.; Cohen, S. M., Multicomponent Metal–Organic Framework Membranes for Advanced Functional Composites. *Chem. Sci.* **2018,** *9,* 8842-8849.

15.   Robeson, L. M., The Upper Bound Revisited. *J. Membr. Sci.* **2008,** *320,* 390-400.

16.   Lin, R.;   Villacorta Hernandez, B.;   Ge, L.; Zhu, Z., Metal Organic Framework Based Mixed Matrix Membranes: An Overview on Filler/Polymer Interfaces. *J. Mater. Chem. A* **2018,** *6,* 293-312.

17.   Rezakazemi, M.;   Ebadi Amooghin, A.;   Montazer-Rahmati, M. M.; Ismail, A. F.; Matsuura, T., State-of-the-Art Membrane Based CO2 Separation Using Mixed Matrix Membranes (MMMs): An Overview on Current Status and Future Directions. *Prog. Polym. Sci.* **2014,** *39,* 817-861.

18.   Aroon, M. A.;   Ismail, A. F.;   Matsuura, T.; Montazer-Rahmati, M. M., Performance Studies of Mixed Matrix Membranes for Gas Separation: A Review. *Sep. Purif. Technol.* **2010,** *75,* 229-242.

19.   Semino, R.;   Moreton, J. C.;   Ramsahye, N. A.;   Cohen, S. M.; Maurin, G., Understanding the Origins of Metal–Organic Framework/Polymer Compatibility. *Chem. Sci.* **2018,** *9,* 315-324.

20.   Tien-Binh, N.;   Vinh-Thang, H.;   Chen, X. Y.;   Rodrigue, D.; Kaliaguine, S., Polymer Functionalization to Enhance Interface Quality of Mixed Matrix Membranes for High CO2/CH4 Gas Separation. *J. Mater. Chem. A* **2015,** *3,* 15202-15213.

21.   Wang, Z.;   Ren, H.;   Zhang, S.;   Zhang, F.; Jin, J., Polymers of Intrinsic Microporosity/Metal–Organic Framework Hybrid Membranes with Improved Interfacial Interaction for High-Performance CO2 Separation. *J. Mater. Chem. A* **2017,** *5,* 10968-10977.

22.   Zhu, H.;   Wang, L.;   Jie, X.;   Liu, D.; Cao, Y., Improved Interfacial Affinity and CO2 Separation Performance of Asymmetric Mixed Matrix Membranes by Incorporating Postmodified MIL-53(Al). *ACS Appl. Mater. Interfaces* **2016,** *8,* 22696-22704.

23.   Venna, S. R.;   Lartey, M.;   Li, T.;   Spore, A.;   Kumar, S.;   Nulwala, H. B.;   Luebke, D. R.;   Rosi, N. L.; Albenze, E., Fabrication of MMMs with Improved Gas Separation Properties Using Externally-Functionalized MOF Particles. *J. Mater.*

Chem. A **2015,** *3*, 5014-5022.

24.   Xie, K.; Fu, Q.; Kim, J.; Lu, H.; He, Y.; Zhao, Q.; Scofield, J.; Webley, P. A.; Qiao, G. G., Increasing both selectivity and permeability of mixed-matrix membranes: Sealing the external surface of porous MOF nanoparticles. *J. Membr. Sci.* **2017,** *535*, 350-356.

25.   Molavi, H.; Shojaei, A.; Mousavi, S. A., Improving Mixed-Matrix Membrane Performance via PMMA Grafting from Functionalized NH2–UiO-66. *J. Mater. Chem. A* **2018,** *6*, 2775-2791.

26.   Wang, H.; He, S.; Qin, X.; Li, C.; Li, T., Interfacial Engineering in Metal–Organic Framework-Based Mixed Matrix Membranes Using Covalently Grafted Polyimide Brushes. *J. Am. Chem. Soc.* **2018,** *140*, 17203-17210.

27.   Yao, B.-J.; Ding, L.-G.; Li, F.; Li, J.-T.; Fu, Q.-J.; Ban, Y.; Guo, A.; Dong, Y.-B., Chemically Cross-Linked MOF Membrane Generated from Imidazolium-Based Ionic Liquid-Decorated UiO-66 Type NMOF and Its Application toward CO2 Separation and Conversion. *ACS Appl. Mater. Interfaces* **2017,** *9*, 38919-38930.

28.   Tien-Binh, N.; Vinh-Thang, H.; Chen, X. Y.; Rodrigue, D.; Kaliaguine, S., Crosslinked MOF-Polymer to Enhance Gas Separation of Mixed Matrix Membranes. *J. Membrane Sci.* **2016,** *520*, 941-950.

29.   Yao, B.-J.; Jiang, W.-L.; Dong, Y.; Liu, Z.-X.; Dong, Y.-B., Post-Synthetic Polymerization of UiO-66-NH2 Nanoparticles and Polyurethane Oligomer toward Stand-Alone Membranes for Dye Removal and Separation. *Chem. Eur. J.* **2016,** *22*, 10565-10571.

30.   Zhang, Y.; Feng, X.; Li, H.; Chen, Y.; Zhao, J.; Wang, S.; Wang, L.; Wang, B., Photoinduced Postsynthetic Polymerization of a Metal–Organic Framework toward a Flexible Stand-Alone Membrane. *Angew. Chem. Int. Ed.* **2015,** *54*, 4259-4263.

31.   Jiang, W.-L.; Ding, L.-G.; Yao, B.-J.; Wang, J.-C.; Chen, G.-J.; Li, Y.-A.; Ma, J.-P.; Ji, J.; Dong, Y.; Dong, Y.-B., A MOF-Membrane Based on the Covalent Bonding Driven Assembly of a NMOF with an Organic Oligomer and its Application in Membrane Reactors. *Chem. Commun.* **2016,** *52*, 13564-13567.

32.   Satheeshkumar, C.; Yu, H. J.; Park, H.; Kim, M.; Lee, J. S.; Seo, M., Thiol–Ene Photopolymerization of Vinyl-Functionalized Metal–Organic Frameworks Towards Mixed-Matrix Membranes. *J. Mater. Chem. A* **2018,** *6*, 21961-21968.

33.   Tien-Binh, N.; Rodrigue, D.; Kaliaguine, S., In-Situ Cross Interface Linking of PIM-1 Polymer and UiO-66-NH2 for Outstanding Gas Separation and Physical Aging Control. *J. Membrane Sci.* **2018,** *548*, 429-438.

34. Gao, X.; Zhang, J.; Huang, K., ROMP for Metal–Organic Frameworks: An Efficient Technique toward Robust and High-Separation Performance Membranes. *ACS Appl. Mater. Interfaces* **2018,** *10*, 34640-34645.

35. Wijmans, J. G.; Baker, R. W., The Solution-Diffusion Model: A Review. *J. Membr. Sci.* **1995,** *107*, 1-21.

36. Merkel, T. C.; Bondar, V. I.; Nagai, K.; Freeman, B. D.; Pinnau, I., Gas sorption, diffusion, and permeation in poly(dimethylsiloxane). *J. Polym. Sci. B: Polym. Phys.* **2000,** *38*, 415-434.

37. Bernardo, P.; Drioli, E.; Golemme, G., Membrane Gas Separation: A Review/State of the Art. *Ind. Eng. Chem. Res.* **2009,** *48*, 4638-4663.

38. Rozicka, A.; Niemistö, J.; Keiski, R. L.; Kujawski, W., Apparent and Intrinsic Properties of Commercial PDMS Based Membranes in Pervaporative Removal of Acetone, Butanol and Ethanol from Binary Aqueous Mixtures. *J. Membr. Sci.* **2014,** *453*, 108-118.

39. Car, A.; Stropnik, C.; Peinemann, K.-V., Hybrid Membrane Materials with Different Metal–Organic Frameworks (MOFs) for Gas Separation. *Desalination* **2006,** *200*, 424-426.

40. Bae, T.-H.; Long, J. R., CO2/N2 Separations with Mixed-Matrix Membranes Containing Mg2(dobdc) Nanocrystals. *Energy Environ. Sci.* **2013,** *6*, 3565-3569.

41. Huang, G.; Yang, Q.; Xu, Q.; Yu, S.-H.; Jiang, H.-L., Polydimethylsiloxane Coating for a Palladium/MOF Composite: Highly Improved Catalytic Performance by Surface Hydrophobization. *Angew. Chem. Int. Ed.* **2016,** *55*, 7379-7383.

42. Wen, G.; Guo, Z., Facile Modification of NH2-MIL-125(Ti) to Enhance Water Stability for Efficient Adsorptive Removal of Crystal Violet from Aqueous Solution. *Colloids Surf. A* **2018,** *541*, 58-67.

43. Hu, Y.; Dai, L.; Liu, D.; Du, W., Rationally Designing Hydrophobic UiO-66 Support for the Enhanced Enzymatic Performance of Immobilized Lipase. *Green Chem.* **2018,** *20*, 4500-4506.

44. Wu, P.; Jiang, M.; Li, Y.; Liu, Y.; Wang, J., Highly Efficient Photocatalytic Hydrogen Production from Pure Water via a Photoactive Metal–Organic Framework and its PDMS@MOF. *J. Mater. Chem. A* **2017,** *5*, 7833-7838.

45. Zhang, W.; Hu, Y.; Ge, J.; Jiang, H.-L.; Yu, S.-H., A Facile and General Coating Approach to Moisture/Water-Resistant Metal–Organic Frameworks with Intact Porosity. *J. Am. Chem. Soc.* **2014,** *136*, 16978-16981.

46. Lee, Y.-R.; Cho, S.-M.; Ahn, W.-S., Effects of Polydimethylsiloxane Coating

of Ni-MOF-74 on CH4 Storage. *Korean J. Chem. Eng.* **2018,** *35*, 1542-1546.

47.   Cavka, J. H.;   Jakobsen, S.;   Olsbye, U.;   Guillou, N.;   Lamberti, C.; Bordiga, S.; Lillerud, K. P., A New Zirconium Inorganic Building Brick Forming Metal Organic Frameworks with Exceptional Stability. *J. Am. Chem. Soc.* **2008,** *130*, 13850-13851.

48.   Wu, D.;   Maurin, G.;   Yang, Q.;   Serre, C.;   Jobic, H.; Zhong, C., Computational Exploration of a Zr-Carboxylate Based Metal–Organic Framework as a Membrane Material for CO2 Capture. *J. Mater. Chem. A* **2014,** *2*, 1657-1661.

49.   Kronast, A.;   Eckstein, S.;   Altenbuchner, P. T.;   Hindelang, K.;   Vagin, S. I.; Rieger, B., Gated Channels and Selectivity Tuning of CO2 over N2 Sorption by Post-Synthetic Modification of a UiO-66-Type Metal–Organic Framework. *Chem. Eur. J.* **2016,** *22*, 12800-12807.

50.   Bentz, K. C.; Savin, D. A., Chain Dispersity Effects on Brush Properties of Surface-Grafted Polycaprolactone-Modified Silica Nanoparticles: Unique Scaling Behavior in the Concentrated Polymer Brush Regime. *Macromolecules* **2017,** *50*, 5565-5573.

51.   Landherr, L. J. T.;   Cohen, C.;   Agarwal, P.; Archer, L. A., Interfacial Friction and Adhesion of Polymer Brushes. *Langmuir* **2011,** *27*, 9387-9395.

52.   Denny Jr., M. S.; Cohen, S. M., In Situ Modification of Metal–Organic Frameworks in Mixed-Matrix Membranes. *Angew. Chem. Int. Ed.* **2015,** *54*, 9029-9032.

53.   Fan, H.;   Shi, Q.;   Yan, H.;   Ji, S.;   Dong, J.; Zhang, G., Simultaneous Spray Self-Assembly of Highly Loaded ZIF-8–PDMS Nanohybrid Membranes Exhibiting Exceptionally High Biobutanol-Permselective Pervaporation. *Angew. Chem. Int. Ed.* **2014,** *53*, 5578-5582.

54.   Yin, H.;   Lau, C. Y.;   Rozowski, M.;   Howard, C.;   Xu, Y.;   Lai, T.; Dose, M. E.;   Lively, R. P.; Lind, M. L., Free-Standing ZIF-71/PDMS Nanocomposite Membranes for the Recovery of Ethanol and 1-Butanol from Water Through Pervaporation. *J. Membr. Sci.* **2017,** *529*, 286-292.

55.   Moore, T. T.; Koros, W. J., Gas Sorption in Polymers, Molecular Sieves, and Mixed Matrix Membranes. *J. Appl. Polym. Sci.* **2007,** *104*, 4053-4059.

56.   Seoane, B.;   Coronas, J.;   Gascon, I.;   Benavides, M. E.;   Karvan, O.; Caro, J.;   Kapteijn, F.; Gascon, J., Metal–Organic Framework Based Mixed Matrix Membranes: A Solution for Highly Efficient CO2 Capture? *Chem. Soc. Rev.* **2015,** *44*, 2421-2454.

57.   Adams, R. T.;   Lee, J. S.;   Bae, T.-H.;   Ward, J. K.;   Johnson, J. R.; Jones, C. W.;   Nair, S.; Koros, W. J., CO2–CH4 Permeation in High Zeolite 4Å

Loading Mixed Matrix Membranes. *J. Membrane Sci.* **2011,** *367*, 197-203.

58.   Etxeberria-Benavides, M.;   David, O.;   Johnson, T.;   Łozińska, M. M.;
Orsi, A.;   Wright, P. A.;   Mastel, S.;   Hillenbrand, R.;   Kapteijn, F.; Gascon, J.,
High Performance Mixed Matrix Membranes (MMMs) Composed of ZIF-94 Filler and
6FDA-DAM Polymer. *J. Membrane Sci.* **2018,** *550*, 198-207.

59.   Barbari, T. A.;   Koros, W. J.; Paul, D. R., Polymeric Membranes Based on
Bisphenol-A for Gas Separations. *J. Membrane Sci.* **1989,** *42*, 69-86.

Chapter 2

Self-Assembly of Metal-Organic Framework (MOF) Nanoparticle Monolayers and Free-Standing Multilayers

Abstract

In this study, the first self-assembled porous monolayer and free-standing multilayer films with Metal-organic framework (MOF) nanoparticles were achieved. Self-assembled MOF monolayers (termed here "SAMMs") were fabricated via self-assembly at a liquid-air interface, producing the flexible films with 87 wt % (89 vol %) MOFs with the maintained porosity. SAMMs were fabricated with core-shell MOF particles which consist of ZIF-8 core and PMMA shell. Core-shell MOF nanoparticles were synthesized by grafting poly(methyl methacrylate) (PMMA) from the particle surface via atom transfer radical polymerization (ATRP) ("graft-from" method) with ZIF-8 particles functionalized with ATRP-initiator using histamine anchor. The self-assembly monolayer formation was aided with the excellent particle dispersibility derived from the PMMA shell and the physical interaction between each PMMA shell of the core-shell MOF particle. Based on the SAMMs techniques, MOF multilayers consisting of several SAMMs layers, and MOF multilayers with alternating SAMM/PMMA polymer film heterostructures also could be fabricated. SAMMs could be coated on the silicon microparticles in order to show the ability for coating on the three-dimensional objects, and the free-standing films with five-stacked layers of SAMMs were fabricated, showing opalescence. These SAMMs demonstrate the significant advancements towards porous film coatings and functional nanoporous membranes. This is the first report about self-assembled porous monolayer and free-standing multilayer films composed of MOF nanoparticles.

Introduction

The development and application of inorganic nanoparticles (NPs) such as Si nanoparticles (SiNPs) and Au nanoparticles (AuNPs), as well as porous nanoparticles such as Metal-organic frameworks (MOFs) and zeolites, have attracted enormous attention for decades.[1-4] In spite of their distinctive properties, processing them to form certain structures such as films is difficult in most cases because of their crystalline and brittle nature.[5-9] The control of inorganic NPs assemblies is one of the interesting approach to obtain the unique properties such as photonic crystals and dense particle packing towards the applications such as membranes, sensors, and so on.[1, 2] Some studies have focused on the ordered NPs flexible films, often through the synthesis of monolayers which have only one-particle thickness.[1, 2, 10-15] Theses efforts are mostly performed with nonporous SiNPs and AuNPs.[10-15]

To form a self-assembly structure with AuNPs (6 nm), a liquid-air interface approach where a drop of a solution containing hydrophobic NPs and organic solvent such as toluene is dropped on the surface of the water and evaporated, is utilized.[1] In order to form monolayers, the method of adding the hydrophobic polymer such as poly-(methyl methacrylate) (PMMA) to the solvent as a filler is often employed. A core-shell technique where the NPs are covered with hydrophobic polymer or linker is also a strong tool to fabricate monolayers. The polymer shell allows for the good dispersibility in the organic solvent and suitable interactions between each particle. For example, the monolayer using AuNPs with a dodecanethiol capping shell was fabricated.[16] For larger AuNPs (20 nm), oligonucleotides or a protein shell are also utilized as a shell to synthesize AuNP monolayers.[10, 11] The core-shell techniques also have been applied to larger SiNPs (~160 nm) with polystyrene (PS) or poly(N-isopropylacrylamide) (PNiPAm) shell.[15, 17] These monolayers were commonly evaluated with atomic force microscopy (AFM) or transmission electron microscopy (TEM), however, the example of free-standing films with ordered particles have not been reported.[15, 17]

Only a few studies about porous-NPs monolayers prepared with self-assembly have been reported.   Goedel et al. synthesized composite membranes with zeolites and polymer, producing zeolite and polymer monolayers(**Figure 2–1**).[18]   However these membranes require a certain amount of polymer to form continuous membranes, which results in the moderate particle loadings (~50 wt %).   Additionally, the thickness of the membranes was not ultrathin (2 μm), contain defects, and the highly ordered particle assemblies were not achieved because of the polydisperse zeolite particles.   Maspoch et al. reported highly ordered porous-NPs self-assembly structure with ZIF-8 (ZIF: Zeolitic Imidazolate Framework) nanoparticles, showing the potential for sensor applications (**Figure 2–2**). [19, 20]   ZIF-8 was used because the monodisperse particles can be readily obtained with a surfactant such as CTAB (cetyltrimethylammonium bromide).   However, the self-assembly structure was fabricated with weak physical interactions among the particles, which generated the powdery and fragile nature. Therefore, the assembly requires a very careful handling and mostly needs the substrate such as a glass plate.   In order to obtain robust films with self-assembled particles, MOF particles decorated with lipids were mixed with polymers.[21]   However, the obtained films were moderate MOF loading (~45 wt % MOF) and the characterization such as porosity, crystallinity and so on were not reported.   In addition, as discussed in General introduction, a lot of studies on Mixed-matrix membranes (MMMs) containing MOF NPs have been reported, however, most of these membranes are fabricated with heterogeneous MOF particles without a high degree of particle ordering, relatively thick (>30 μm) and moderate MOF loading.[8]
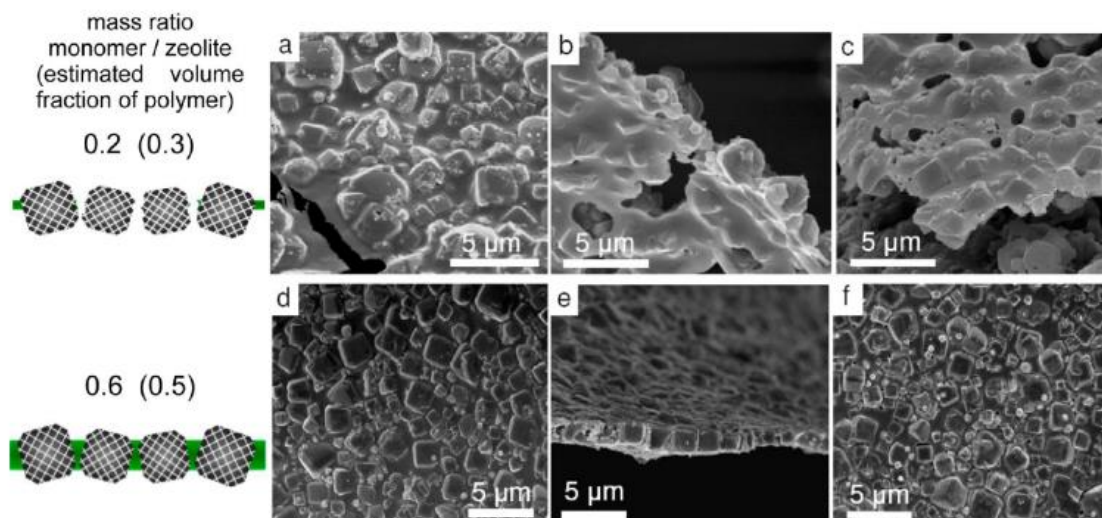
Figure 2–1. Scanning electron microscopy (SEM) images of composite membranes with zeolite particles. From the top to the bottom row, the mass fractions of the monomer are increasing. The first column is the schematic cross-sectional figures of the membranes. (a, d) top views. (b, e) cross section views. (c, f) bottom views.[18]
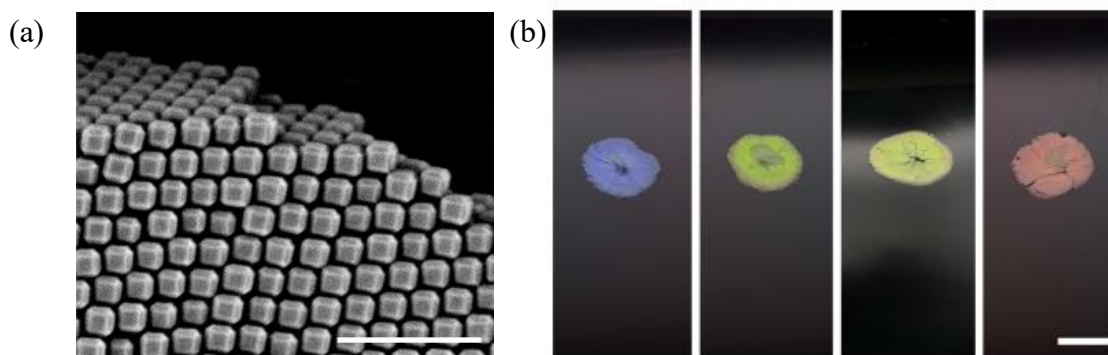
Figure 2–2. Self-assembly structure with monodisperse ZIF-8 particles: (a) SEM image of the self-assembled structure. Scale bar is 1 μm. (b) Photographs of self-assembled structures. As the lattice period is comparable to visible wavelengths, various opalescence is visible to the naked eye depending on the particles sizes: 178 ± 8 nm (blue); 193 ± 8 nm (green); 210 ± 10 nm (yellow); and 227 ± 10 nm (red). Scale bar is 1 cm.[19]

In this chapter, MOF-polymer hybrid materials of core-shell MOF particles were utilized to achieve high MOF-loaded thin films with the ordered assembly, which are flexible monolayer and multilayer films. Monodisperse ZIF-8 nanoparticles are employed here, because the particle size and the dispersity of ZIF-8 particles are controllable with an addition of a surfactant. ZIF-8 is one of the most well-studied MOFs, which consists of Zn ions and 2-methylimidazole, having a zeolite-like topologies as the angle of metal-imidazole-metal in ZIF-8 is similar to that of Si-O-Si (145 °) in zeolites (**Figure 2–3**).[22, 23] Additionally, the unique properties of ZIF-8 have attracted enormous attention; such as the high stability, the mild synthesis conditions, the ability of the modification, and the pore size which is suitable for some applications (e.g., gas separation membranes for propylene/propane separation).[22, 24]

(a)　　　　　　　　　　　　　(b)
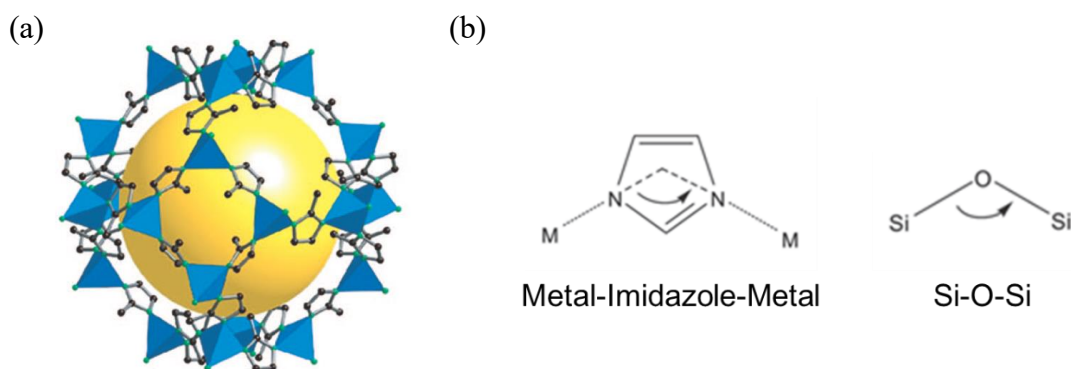
Figure 2–3. (a) ZIF-8 crystal structure.[22] (b) The bridging angles of the metal-imidazole-metal in ZIF-8 and zeolites, and Si-O-Si in zeolites.[23]

By growing PMMA polymer brushes on the surface of ZIF-8 particles using a histamine anchor via atom transfer radical polymerization (ATRP), core-shell MOF nanoparticles with polymer shell were synthesized. In contrast to Chapter 1 where the polymer matrix was utilized for the membrane fabrication, self-assembled MOF monolayers (termed here "SAMMs") were achieved using a liquid-air interface method only with the core-shell MOF particles (**Figure 2–4**). The obtained monolayers predominantly consist of ZIF-8 nanoparticles (87 wt % and 89 vol % MOF) and ultrathin (~200 nm) which is almost the same size of the MOF particles used in this study. Additionally, the SAMMs demonstrated the retained porosity and crystallinity of ZIF-8. The applicability of SAMMs techniques is also shown by fabricating multilayers consisting of several SAMMs, synthesizing the multilayers composed of SAMM/polymer thin film heterostructures, covering three-dimensional objects with SAMMs, and synthesizing free-standing films with only five-stacked SAMMs having

opalescence.　These synthetic controls demonstrate the potential for diverse applications.　To the best of our knowledge, this study is the first report on porous self-assembled monolayers with highly ordered porous inorganic particles.　Based on this study, the concept of SAMMs would create novel porous materials which are beyond conventional nanoparticle-based materials.
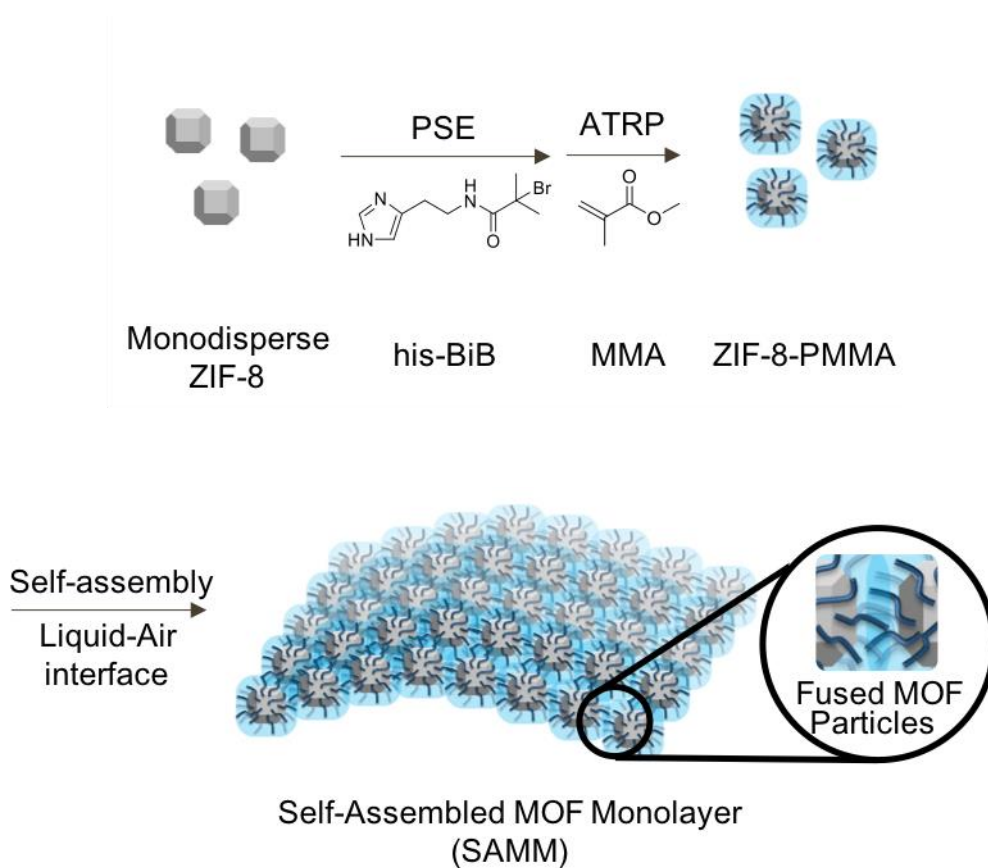
Figure 2–4.　Synthesis of SAMMs with core-shell ZIF-8 PMMA particles.

Experimental Section

Ligand Synthesis

Starting materials were purchased and used from commercially available suppliers (Sigma-Aldrich, Matrix Scientific, Acros Organics, and others) and used without further purification.

N-(2-(1*H*-imidazol-4-yl)ethyl)-2-bromo-2-methylpropanamide (1). Histamine dihydrochloride (5.0 g, 27.2 mmol), triethylamine (12.7 g, 125.7 mmol, 4.6 eq) and $CHCl_3$ (400 mL) were added to a 1 L round bottom flask. The resulting mixture was cooled to 0 ˚C in an ice bath, and a-bromoisobutyryl bromide (BiBB) (12.7g, 55 mmol, 2.0 eq) was added dropwise via a syringe. After adding BiBB, the solution was warmed to room temperature and stirred overnight. The reaction was quenched using 500 mL 10% KOH aqueous solution. The solution was extracted with CH_2Cl_2 and dried with magnesium sulfate. After removing solvent, the crude product was recrystallized with EtOAc to give the desired product (compound **1**). Yield: 5.6 g, 79%. ^{1}H NMR (400 MHz, CD$_3$OD): δ 7.58 (s, 1H), 6.86 (s, 1H), 3.44 (t, J = 7.2 Hz, 2H), 2.80 (t, J = 7.2 Hz, 2H), 1.88 (s, 6H). ESI-MS(+) Experimental: m/z 260.11 [M+H] + , Calculated for [$C_9H_{14}BrN_3O$]: 259.03.

MOF Syntheses

ZIF-8. $Zn(CH_3COO)_2 \cdot 2H_2O$ (1.50 g, 6.8 mmol) dissolved in 25 mL water was added to 2-methylimidazole (5.30 g, 65 mmol) dissolved in 25 mL of 0.54 mM cetyltrimethylammonium bromide (CTAB) aqueous solution with gentle stirring for 1 min. The color of the mixture turned white after 15 s. The solution was left undisturbed at room temperature for 2 h. The white ZIF-8 particles were collected by centrifugation (fixed-angle rotor, 9000 rpm, 10 min), washed with 3×40 mL portions of MeOH. In order to prevent the aggregation, the particles were used for the next reaction without drying. The yield was calculated based on the concentration of ZIF-8 solution by taking a small volume of suspension, drying to determine mass, and calculating total mass from total volume. Yield: 1.17 g, 75% based on $Zn(CH_3COO)_2 \cdot 2H_2O$. The crystallinity was confirmed by PXRD to be ZIF-8 (**Figure 2–12**), and the particle sizes were determined to be ~174 ± 15 nm by SEM (**Figure 2–6**). The BET surface area (m^2/g) was measured to be 1625 ± 55 m^2/g.

ZIF-8-His in synthetic route A. ZIF-8 (0.50 g, 4.4 mmol) was dispersed in 30 mL MeOH with an ultrasonic bath. Histamine (0.98 g, 8.8 mmol) was dissolved in 30mL of MeOH, and ZIF-8 solution and histamine solution were added to a 150 mL round bottom flask. The combined suspension was stirred at room temperature for 24 h. The particles were collected by centrifugation (fixed-angle rotor, 9000 rpm, 10 min), washed with 3×40 mL portions of MeOH, soaked in MeOH for 24 h, and dried under vacuum at room temperature. The particle shapes and sizes were measured by SEM (**Figure 2–8**). Conversion of the PSE reaction was confirmed by measuring the digested ZIF-8-His with ^{1}H NMR (400 MHz, CDCl$_3$). The histamine amount was measured out to be ~17.1 mol%.

ZIF-8-BiB in synthetic route A. ZIF-8-His (0.40 g, 3.5 mmol) was dispersed in 60 mL of THF in 250 mL round bottom flask with an ultrasonic bath. Trimethylamine (0.53g, 5.3 mmol, 1.5 eq) was then added to solution. The resulting mixture was cooled to 0 ˚C in an ice bath, and α-bromoisobutyryl bromide (BiBB) (0.4g, 1.8 mmol, 0.5 eq) in 10 mL THF was added dropwise via a syringe. After the addition, the solution was warmed to room temperature or heated to 50 °C overnight. The particles were collected by centrifugation (fixed-angle rotor, 9000 rpm, 10 min), washed with 2 × 40 mL portions of THF and 2×40 mL portions of MeOH, soaked in MeOH for 24 h, and dried under vacuum at room temperature. The particle shapes and sizes were measured by SEM (**Figure 2–8**). Conversion of the PSE reaction was confirmed by measuring the digested ZIF-8-BiB with ^{1}H NMR (400 MHz, CDCl$_3$). The conversion was measured out to be trace amount in room temperature reaction, and 3.9 mol% in 50 °C reaction.

ZIF-8-BiB via synthetic route B. ZIF-8 (1.12 g, 9.8 mmol) was dispersed in 40 mL 1-BuOH via solvent exchange of ZIF-8 solution from MeOH to 1-BuOH by centrifugation (fixed-angle rotor, 9000 rpm, 10 min). The ZIF-8 solution and the his-BiB mixture (2.55 g, 9.8 mmol, 1.0 eq) were added to a 100 mL round bottom flask. The combined suspension was sonicated for 5 min in an ultrasonic bath, then stirred at 100 °C for 4 h. After cooling to room temperature, the particles were collected by centrifugation (fixed-angle rotor, 9000 rpm, 10 min), washed with 3×40 mL portions of MeOH, and soaked in MeOH for 24 h. To prevent aggregation, the particles were used for next reaction without drying. Yield: 950 mg, 85%. The crystallinity was confirmed by PXRD (**Figure 2–12**), and the particle sizes were confirmed with SEM images (**Figure 2–10**). The BET surface area (m^2/g) was measured to be 1557 ± 158

92

m^2/g.   Conversion of the PSE reaction was confirmed by measuring the digested ZIF-8-BiB with ^{1}H NMR (400 MHz, CDCl$_3$).   The his-BiB amount was measured out to be ~2 mol%.   PSE of ZIF-8 with his-BiB using mild conditions resulted in no evidence of particle degradation.   It is important to note this here as previous attempts in the literature to perform postsynthetic chemistry on ZIF-8 particles have resulted in particle degradation.[25].   The ratio of the his-BiB and the quantity of surface imidazole linker was also calculated, indicating that 33% of the surface was functionalized with his-BiB (vide infra).   The ATRP initiator density which is equal to density of his-BiB on the particle surface was also calculated to be 0.45 initiators/nm^2.

ZIF-8-PMMA.   ZIF-8-BiB (100 mg, 0.017 mmol initiator) was mixed with 3.6 mL methanol in a 10 mL round bottom flask, and dispersed using sonication for 30 min. Purified methyl methacrylate (1.3 g, 13.6 mmol, 800 eq based on the initiator), 0.9 mL of CuCl$_2$-PMDETA (N, N, N', N'', N'''-pentamethyldiethylenetriamine) stock solution (containing 0.0041 mmol CuCl$_2$, 0.041 mmol PMDETA in MeOH) were added sequentially.   The vial was sealed with a rubber plug and carefully degassed by N$_2$ purging.   After 30 min, a degassed ascorbic acid solution (17 mg, 0.1 mmol in 1 mL MeOH) was added using a syringe.   The molar ratio of the reagents was monomer: macroinitiator: catalyst: ligand: reducing agent = 800: 1: 0.24: 2.4: 5.6.   The reaction was kept at room temperature for 18 h.   The particles were collected by centrifugation (fixed-angle rotor, 9000 rpm, 10 min), washed with 3×40 mL portions of MeOH.   The particles were subsequently washed 1x40 mL of toluene to wash off any excess polymer.   The ZIF-8-PMMA particles were dried using a vacuum oven at 60 °C for 24 h.   The particle shapes were confirmed by SEM (**Figure 2–17**).   The crystallinity was confirmed by PXRD (**Figure 2–12**).   BET surface area (m^2/g) was measured to be 1398±80 m^2/g.   After digestion, polymer precipitate was confirmed to be PMMA (**Figure 2–13**) via ^{1}H NMR (400 MHz, CDCl$_3$).   GPC was measured with THF to be M_w =122k g/mol, M_n = 75k, M_w/M_n = 1.63 (**Figure 2–14**).

Digestion of ZIF-8-BiB particles.   10.0 mg of dry ZIF-8-BiB particles were immersed in mixture of 480 µL of MeOD solution and 20 µL of D$_2$SO$_4$ with bath sonication until the solution becomes clear.   The ratio of the integral value of the alkyl group (α-bromoisobutyryl) in his-BiB and the aromatic group of 2-methylimidazole in ZIF-8 was used to determine the conversion with results which showed 1.7±0.3 mol% his-BiB when compared to the total 2-methylimidazole content of ZIF-8 particles.

Digestion of ZIF-8-PMMA.   20.0 mg of dry ZIF-8-PMMA particles were immersed in 480 μL MeOH solution and 20 μL of H_2SO_4 with bath sonication for twenty minutes. Obtained precipitation was collected via centrifugation, washed with 3×10 mL portions of MeOH, and dried under vacuum at 50 °C.

<u>SAMM Film Fabrication</u>

Monolayer film fabrication (Evaporation-induced interfacial assembly).   ZIF-8-PMMA (30 mg) was mixed with 1 mL of toluene in a small vial and dispersed using sonication for 60 min.   The interfacial assembly of ZIF-8-PMMA particles was carried out by dispensing 10 μL of ZIF-8-PMMA solution onto the water in a 4 inch petri dish. After drying for 1 min, the thin SAMM was scooped with SEM carbon tape or TEM grids on the glass plate.

Fabrication of monolayer on SiO_2 microparticles.   An aqueous solution of SiO_2 microparticles (Aldrich, particle size 5 um) was placed onto SEM carbon tape placed on a glass slide.   This carbon tape was used to collect the SAMM using the same procedure shown above.

Homo-multilayer film fabrication.   ZIF-8-PMMA (30 mg) was mixed with 1 mL toluene in a small vial and dispersed using sonication for 60 min.   For the fabrication of the first layer, the interfacial assembly of SAMM was carried out by dispensing 10 μL of ZIF-8-PMMA solution onto the water in petri dish.   After drying for 1 min, the thin film was scooped with a thin cover glass.   After drying the film at 100 °C for 10 min, the same procedure was utilized for the fabrication of the second and third layer sequentially.   The thin cover glass was broken, and the edge of the multi-layer film was exposed for cross-section SEM.

Hetero-multilayer films fabrication.   ZIF-8-PMMA was synthesized using the monolayer procedure above.   After drying for 1 min, the SAMM was scooped with a thin cover glass and dried at 100 °C for 10 min.   PMMA (Aldrich, average M_w ~120,000) was used for the fabrication of the second layer and the fourth layer. PMMA (4.5 mg) was mixed with 1 mL toluene in a small vial.   The thin PMMA film fabrication was carried out by dispensing 20 μL of PMMA solution onto the water in petri dish.   After drying for 1 min, the thin film was scooped with the thin cover glass with the first layer and dried at 100 °C for 10 min.   The third layer and the fourth layer were also fabricated with the same procedure sequentially.   The thin cover glass was

broken, and the edge of the multi-layer film was exposed for the cross-section SEM measurement.

Self-standing film fabrication.   ZIF-8-PMMA (30 mg) was mixed with 1 mL of toluene in a small vial and dispersed using sonication for 60 min.   The interfacial assembly of SAMM was carried out by dispensing 10 μL of ZIF-8-PMMA solution onto the water in 20 mL vial.   After drying for 30 min, the free-standing film was collected with a wire ring, showing opalescence (**Figure 2–30**).   The obtained film was used for SEM measurement.

Characterization

Nuclear magnetic resonance (NMR).   400 MHz Varian FT-NMR spectrometer was used to record proton nuclear magnetic resonance spectra (^{1}H NMR).   Chemical shifts are measured in parts per million (ppm) with a reference of the appropriate solvent peak.

Powder X-ray diffraction (PXRD).   For the analysis with PXRD, ~50 mg of dry MOF powder or SAMM was put on silicon sample holder.   A Bruker D8 Advance diffractometer was used and PXRD data was collected at room temperature, at 40 kV, 40 mA for Cu Ka (l = 1.5418 Å), with a scan speed of 2 sec/step, a step size of 0.05° in 2θ, and a 2θ range of 2-50°.

Brunauer-Emmett-Teller (BET) surface area analysis.   Prior to analysis, samples were evacuated on a vacuum line at room temperature overnight.   Then, ~50 mg samples were put to pre-weighed sample tubes and degassed at 105 °C until the outgas rate was less than 5 mmHg on a Micromeritics ASAP 2020 Adsorption Analyzer.   After degassing, the sample tubes were re-weighed to get a mass for the samples.   BET surface area (m^2/g) were measured with N_2 at 77 K with a Micromeritics ASAP 2020 Adsorption Analyzer using volumetric techniques.

Scanning electron microscopy (SEM).   MOF particles or SAMM films (~3 mm^2) were put on conductive carbon tape attached to a SEM sample holder disk, and coated using an Iridium-sputter coating for 8 s.   A FEI Quanta 250 SEM instrument was used to measure images with an energy source of 5 kV at a working distance at 10 mm under vacuum.   Particle sizes of more than 10 different particles were measured in SEM images and given with error bars as a standard deviation.

Transmission electron microscopy (TEM). TEM was measured with JEOL 1200 EX II TEM equipped with a 35 mm port digital camera (1 megapixel) for capturing almost full-field-of-view images, and a 7 megapixel bottom-mount digital camera that captures a smaller field at higher resolution.

Contact angle measurements. Water contact angles were measured with a Ramé-Hart DROPimage CA v2.5 instrument and the manufacturer's software. Approximately 5-10 mg of the sample was pressed onto a glass slide with another glass plate. A drop of water was slowly dropped on the pressed sample with a microsyringe and the contact angle was measured.

Thermal Gravimetric Analysis (TGA). About 10 mg of samples were used for TGA measurements. TGA was measured with 75 cm^3/min air, a scan rate of 5 °C/min from room temperature to 800 °C using TA Instrument Q600 SDT.

Gel permeation chromatography (GPC). GPC was performed in THF at 35 °C with a flow rate of 1.0 mL/min using an Agilent 1260 HPLC with diode array, Wyatt DAWN HELEOS 8+ light scattering detector, Viscostar III viscometer, and Optilab TrEX refractive index

Results and Discussion

   In order to obtain monodisperse ZIF-8 particles for the self-assembly structures, truncated rhombic dodecahedral ZIF-8 particles were synthesized with CTAB (**Figure 2–5a**).[19, 26]   CTAB is a cationic surfactant and employed as a capping agent which controls the particle size and the shape of ZIF-8 particles.   A hydrophobic hydrocarbon chain of CTAB can selectively attach to the certain facets of the ZIF-8 particle, slowing down the growth of the facet ({100} facets), which results in the controlled particle shape and size.   Therefore, while ZIF-8 crystallizes into the thermodynamically more stable rhombic dodecahedral without CTAB, the addition of CTAB enables the synthesis of monodisperse truncated rhombic dodecahedral ZIF-8 particles (**Figure 2–5b**).[26]   By selecting the suitable concentration of CTAB and 2-methylimidazole, desired monodisperse ZIF-8 particles with truncated rhombic dodecahedral shape could be obtained.   Scanning electron microscopy (SEM) images showed monodisperse ZIF-8 particles with controlled particle sizes (174 ± 15 nm). The average particles size was calculated with the particle sizes of 10 randomly selected particles in the SEM images (**Figure 2–6**).

(a)   (b)
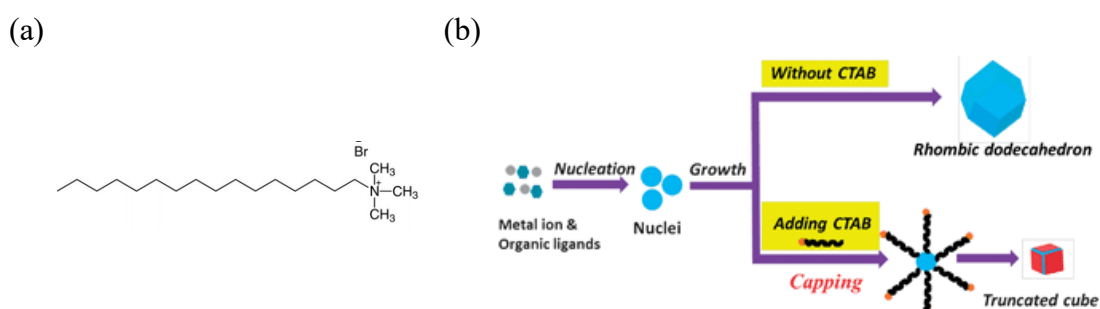

Figure 2–5.   (a) Chemical structure of CTAB.   (b)ZIF-8 growth with and without CTAB.[26]
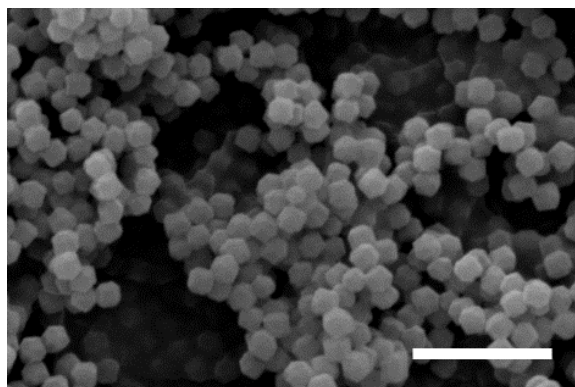
**Figure 2–6.**   SEM images of ZIF-8 particles.   Scale bar is 1 μm.

To obtain ZIF-8 particles functionalized with an alkyl halide as a polymerization initiator of ATRP, postsynthetic methods were applied (**Figure 7** in General introduction).   ATRP was selected for the postsynthetic polymerization (PSP) because the reaction is well established to synthesize polymer brushes on the surface of the particles including MOFs.   Histamine was used as an anchor to connect ZIF-8 with ATRP initiator group.   Two different synthetic routes were performed to obtain desired particles; synthetic route A and B (**Scheme 2−1**).
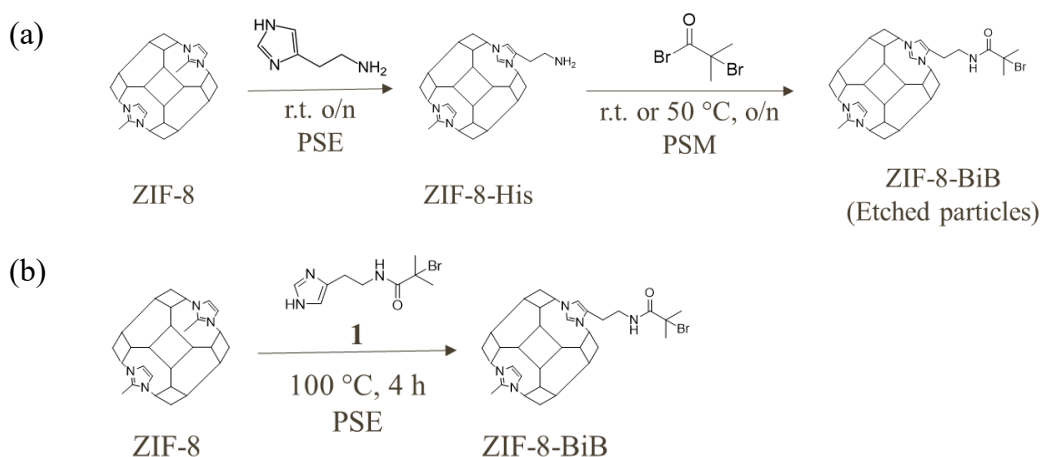
Scheme 2−1.   Synthetic routes of ZIF-8-BiB: (a) Synthetic route A.   (b) Synthetic route B.

In the synthetic route A, the histamine was introduced to ZIF-8 particles using postsynthetic exchange (PSE) reaction in order to produce ZIF-8 containing histamine (ZIF-8-His), then ATRP initiator was introduced to the surface of ZIF-8 particles through postsynthetic modification (PSM) reaction with the amino group of the histamine in ZIF-8-His and α-bromoisobutyryl bromide (BiBB), resulting in ZIF-8-BiB. ZIF-8-His was synthesized via PSE reaction at room temperature for 24 h, showing 17.1% PSE conversion determined with Proton nuclear magnetic resonance spectra (^{1}H NMR) (**Figure 2−7**).   The SEM image shows the particles with a small etching on the surface (**Figure 2−8**) (similar phenomena in PSE reaction with ZIF-8 particles were observed in the literature).[25]   This small etching is probably caused by the amino groups of histamine.   The following PSM reaction with BiBB was performed based on the reported PSM conditions about BiBB functionalization of MOFs.[27-29]   In the case of the reaction at room temperature, the conversion of α-bromoisobutyryl group (BiB group) was revealed to be a trace amount evidenced by ^{1}H NMR (**Figure 2−9**).   While, in the case of the reaction at 50 °C, the PSM conversion was calculated to be 3.9 mol%;

however, the resulting particles showed a severe etching and the degradation of the surface revealed in SEM images (**Figure 2–8c**).   These results suggest that PSM with BiBB causes the severe degradation of the ZIF-8-His particles in the synthetic condition for the improved PSM conversion.   The degradation is probably caused by HBr generated from the reaction between BiBB and amino group of histamine since ZIF-8 is unstable against an acid condition.
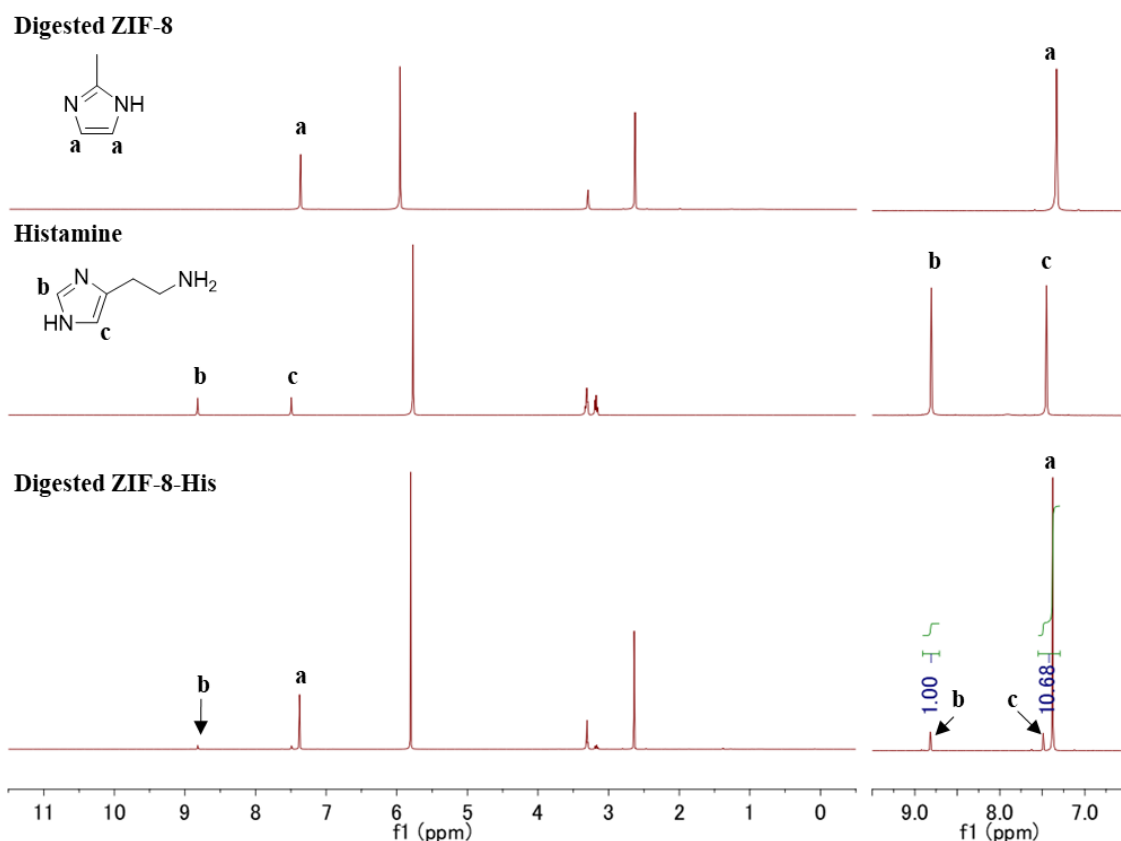

Figure 2–7.   NMR spectra of digested ZIF-8, histamine, digested ZIF-8-His.   The conversion of histamine in the ZIF-8-His was calculated based on the integral value of 7.49 ppm and 8.82 ppm of hydrogen peak of histamine and 7.39 ppm of aromatic hydrogen peak of 2-methylimidazole.   The conversion of histamine was calculated via the equation: (Integral value of aromatic hydrogen peak b of histamine) / ((Integral value of aromatic hydrogen peak b of histamine) + ((Integral value of aromatic hydrogen peaks of 7.39 –7.49 ppm) – (Integral value of aromatic hydrogen peak b of histamine)) / 2) × 100.   The conversion was calculated to be 17.1 %.

99
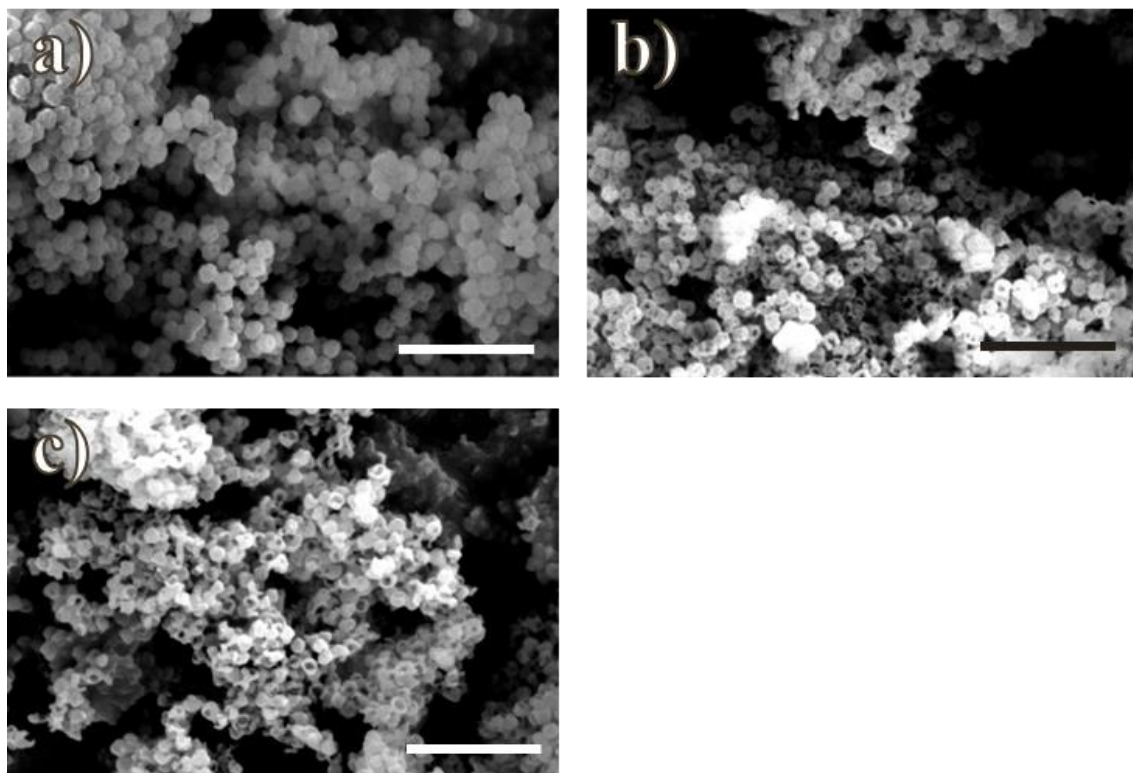
Figure 2–8. SEM images of ZIF-8 derivatives obtained in synthetic route A:　(a) ZIF-8-His particles.　(b, c) ZIF-8-BiB particles; (b) PSM reaction at room temperature for 24 h, (c) PSM reaction at 50 °C for 24 h.　Scale bars are 1 μm.
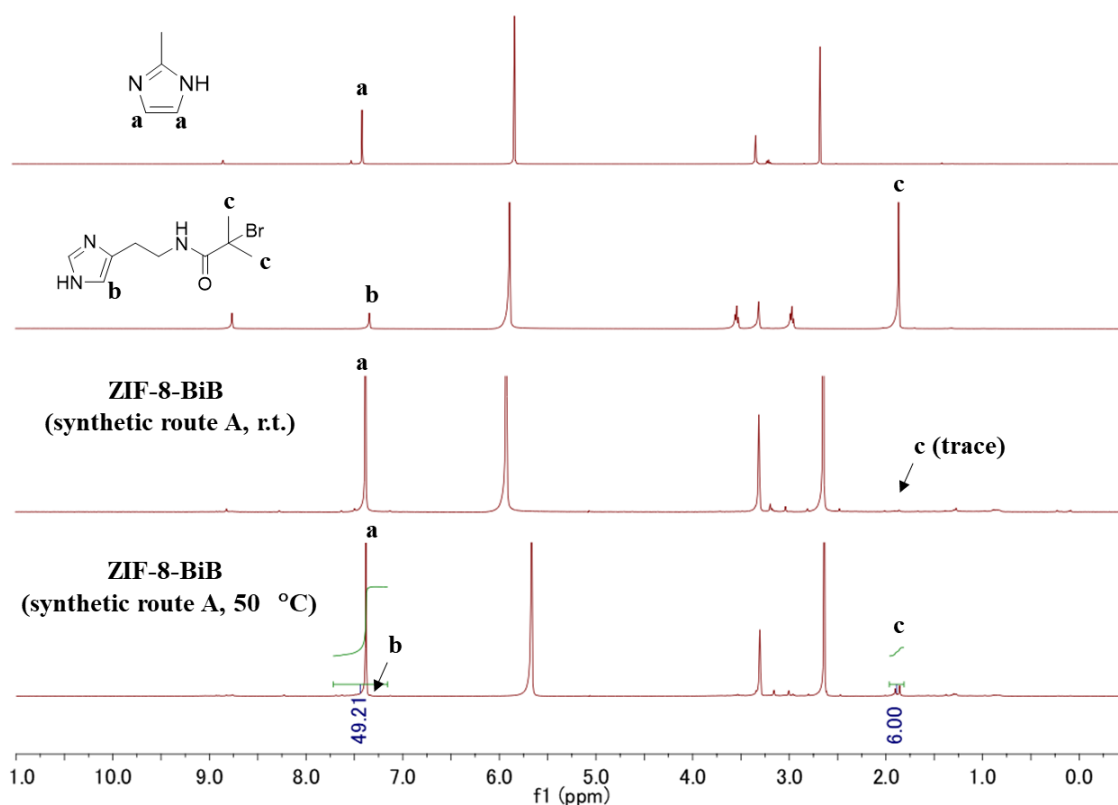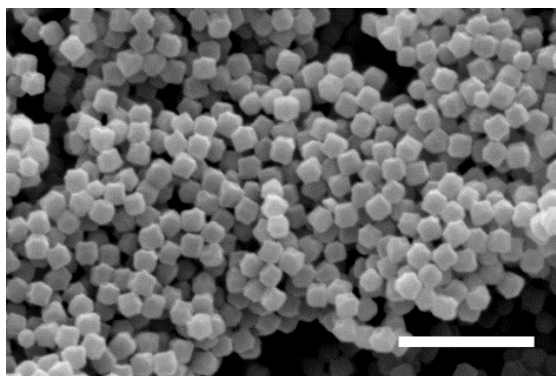
Figure 2–9.   NMR spectra of ZIF-8-BiB synthesized at room temperature and 50 °C via synthetic route A after digestion.   The conversion of BiB group was calculated based on the integral value of 1.86 ppm of hydrogen peak of BiB group and 7.39 ppm of aromatic hydrogen peak of 2-methylimidazole and aromatic hydrogen peak of BiB group.   BiB group conversion was calculated via the equation: (Integral value of hydrogen peak of BiB group / 6) / ((Integral value of aromatic hydrogen peaks – Integral value of hydrogen peak of BiB group / 6) / 2 + (Integral value of hydrogen peak of BiB group / 6)) ×100.

In the synthetic route B, his-BiB (**1**) was presynthesized with histamine dihydrochloride and BiBB (**Scheme 2–2**), and introduced to ZIF-8 particles via PSE reaction, resulting in ZIF-8-BiB.　The SEM images of ZIF-8-BiB particles demonstrate no degradation or etching occurred through the PSE reaction, showing the maintained shapes and particle sizes (**Figure 2–10**), probably because no byproducts such as a strong acid are generated in this reaction.　Using ^{1}H NMR spectra, the mol fraction of his-BiB in ZIF-8-BiB particles was determined to be ~2 mol% based on 2-methylimidazole (**Figure 2–11**).　Despite the large amount of his-BiB in the PSE reaction, the tiny quantities of his-BiB were observed.　This result indicates his-BiB was mostly located on the surface of the particles, as the size of his-BiB is apparently much larger than ZIF-8 effective pore size of $0.40 - 0.42$ nm.[30, 31]　The contact angle measurements demonstrated that the contact angle of ZIF-8-BiB was decreased to be 18° compared to 68° of ZIF-8 particles, showing the decreased hydrophobicity, which also supports that the PSE reaction proceeded preferably on the surface of the particles (**Figure 2–19**, vide infra).　The small contact-angle value of ZIF-8-BiB is probably derived from the hydrophilic amide group of his-BiB in ZIF-8-BiB particles.
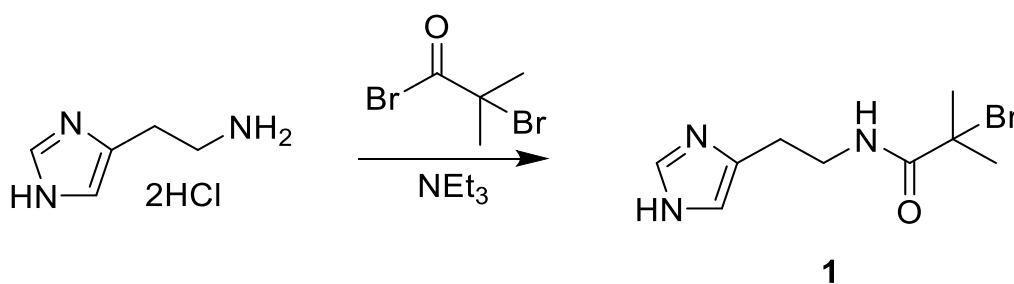
Scheme 2–2.　Synthesis of N-(2-(1H-imidazol-4-yl)ethyl)-2-bromo-2-methylpropanamide (his-BiB) (**1**).

Figure 2–10.　SEM images of ZIF-8-BiB particles synthesized via synthetic route B. Scale bar is 1 μm.
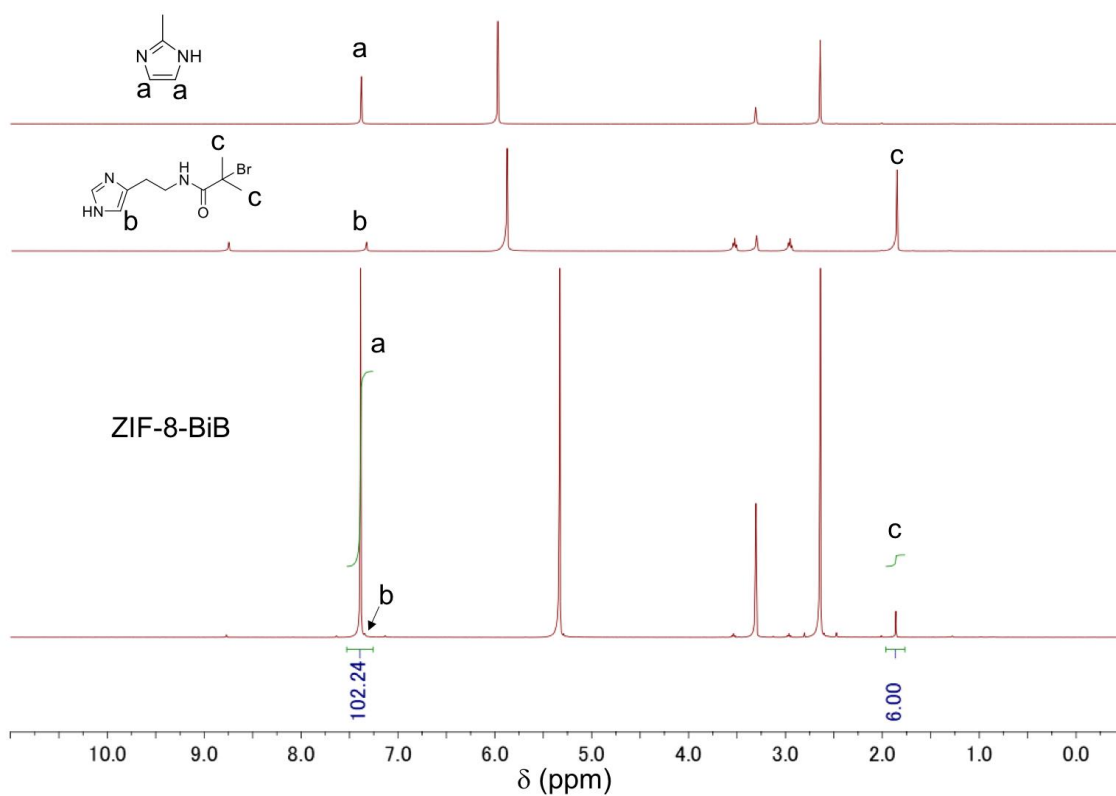
Figure 2–11. NMR spectra of ZIF-8-BiB synthesized via synthetic route B after digestion. The conversion of his-BiB in the ZIF-8-BiB was calculated based on the integral value of 1.86 ppm of hydrogen peak of BiB group in his-BiB and 7.39 ppm of aromatic hydrogen peak of 2-methylimidazole and aromatic hydrogen peak of his-BiB. his-BiB conversion was calculated via the equation: (Integral value of hydrogen peak of BiB group in his-BiB / 6) / ((Integral value of aromatic hydrogen peaks – Integral value of hydrogen peak of BiB group in his-BiB / 6) / 2 + (Integral value of hydrogen peak of BiB group in his-BiB / 6)) ×100.

The ratio of the his-BiB and the quantity of surface imidazole linker were also calculated as below. Average particle facet length of ZIF-8-BiB was roughly 175 nm as determined by SEM. The volume of each particle was calculated by (volume of a cube):

$$(175 \ nm)^3 = 5.36 \times 10^6 \ nm^3/particle$$

The length of a side of the unit cell of ZIF-8 is 1.6993 nm based on the literature.[32] Therefore, the volume of the unit cell is calculated by:

$$(1.6993 \ nm)^3 = 4.91 \ nm^3/unit \ cell$$

The number of 2-methylimidazole (Im) in each unit cell is 24. Therefore, the number of Im in each particle is calculated by:

$$\frac{5.36 \times 10^6 \ nm^3/particle \ \times \ 24 \ Im/unit \ cell}{4.91 \ nm^3/unit \ cell} = 2.62 \ \times \ 10^7 \ Im/particle$$

The mole ratio of 2-methylimidazole to his-BiB in ZIF-8-BiB is 1.94 mol% as determined by NMR (**Figure 2–11**, this can change depending on the PSE conversion). The number of his-BiB is calculated by:

$$2.62 \ \times \ 10^7 \ Im/particle \ \times \ 0.0194 = 5.09 \ \times \ 10^5 \ his-BiB/particle$$

The surface area of each particle is given by:

$$(175 \ nm)^2 \times 6 = 1.84 \ \times \ 10^5 \ nm^2/particle$$

The surface area of one face of unit cell is given by:

$$(1.6933 \ nm)^2 = 2.89 \ nm^2/unit \ cell$$

Therefore, surface exposed 2-methylimidazole is calculated by:

$$\frac{1.84 \ \times \ 10^5 \ nm^2/particle \times \ 24 \ Im/unit \ cell}{2.89 \ nm^2/unit \ cell}$$

$$= 1.53 \ \times \ 10^6 \ Im/particle \ surface$$

Considering that his-BiB is located on the surface, the mole ratio of 2-methylimidazole on the surface to his-BiB on the surface is calculated by:

$$\frac{5.09 \times \ 10^5 \ His-BiB/particle \ surface}{1.53 \ \times \ 10^6 \ Im/particle \ surface} \times 100 = \ 33 \ \%$$

Therefore, the conversion of PSE on the particle surface is around 33 %. In addition, the his-BiB density which is equal to the initiator density on the surface is calculated by:

$$\frac{5.09 \times 10^5 \; His - BiB/particle}{1.84 \times 10^5 \; nm^2/particle \times 6} = 0.45 \; his - BiB/nm^2$$

The values of 33 % of PSE conversion and 0.45 his-BiB/nm^2 of his-BiB density are reasonable to consider with PSE mainly occurring on the surface of the particles.

To synthesis core-shell ZIF-8 particles (ZIF-8-PMMA), ARGET ATRP (Activators regenerated by electron transfer atom transfer radical polymerization) was used with methyl methacrylate (MMA) as a PSP reaction ("grafting-from" method) (**Figure 2–4**).   ARGET-ATRP has been widely used for synthesizing a polymer brush, and has two advantages over conventional ATRP: the improved oxygen tolerance and the reduced use of a heavy metal catalyst.   Ascorbic acid and *N,N,N',N'',N'''*-pentamethyldiethylenetriamine (PMDETA) were selected as a reducing agent and ligand, respectively.   The polymer grows from the initiator which is an alkyl halide of BiB group on the surface of the particles.   After the grafting reaction, the resulting particles were washed with methanol and toluene to remove the remaining monomer and the other reagents.   Powder X-ray diffraction (PXRD) analysis demonstrated that ZIF-8-PMMA still retained ZIF-8 crystallinity after the PSE and ATRP reactions (**Figure 2–12**). ^{1}H NMR spectra of the digested ZIF-8-PMMA evidenced the presence of grafted PMMA polymer (**Figure 2–13**), and gel-permeation chromatography (GPC) measurements with digested ZIF-8-PMMA particles showed that the polymerization successfully proceeded, albeit with poor control (Mn = 75k g/mol, Mw = 112k g/mol, Mw / Mn = 1.63) (**Figure 2–14**).   The relatively high dispersity is unsurprising, as ascorbic acid is known to rapidly reduce Cu(II) to Cu(I) which lowers the concentration of deactivator and overall control of the polymerization, and the 2-bromoisobutyramide initiator can limit the initiation efficiency of MMA due to the penultimate effect.[33, 34] However, this was not seen as a drawback, as several studies have shown that broad dispersity of the polymer brush can increase particle-particle interaction.[35, 36]

ZIF-8 mass fraction in ZIF-8-PMMA was determined using Thermogravimetric analysis (TGA).   The weight loss of ZIF-8, PMMA polymer, and ZIF-8-PMMA were measured for the calculation of ZIF-8 contents, which showed the extremely high ZIF-8 mass fraction of 87 wt % (89 vol %) in ZIF-8-PMMA (**Figure 2–15, Table 2–1**).   The surface area of ZIF-8-PMMA was measured to be 1398 ± 80 m^2/g using Brunauer-Emmett-Teller (BET) surface area analysis (**Table 2-1**).   As PMMA polymer is a non-porous material (**Figure 2–16**), the BET surface area of 1398 ± 80 m^2/g was predominantly derived from the ZIF-8 component in the core-shell MOF.   Based on the BET surface area of ZIF-8 particles (1625 ± 55 m^2/g) and ZIF-8 contents in ZIF-8-

PMMA (87 wt %), the theoretical (estimated) surface area of ZIF-8-PMMA can be calculated to be ~1413 m^2/g, which is consistent with the experimental surface area of ZIF-8-PMMA (1398 ± 80 m^2/g).   This calculation clearly shows that the porosity of ZIF-8 is intact even after the PSE and PSP reactions.
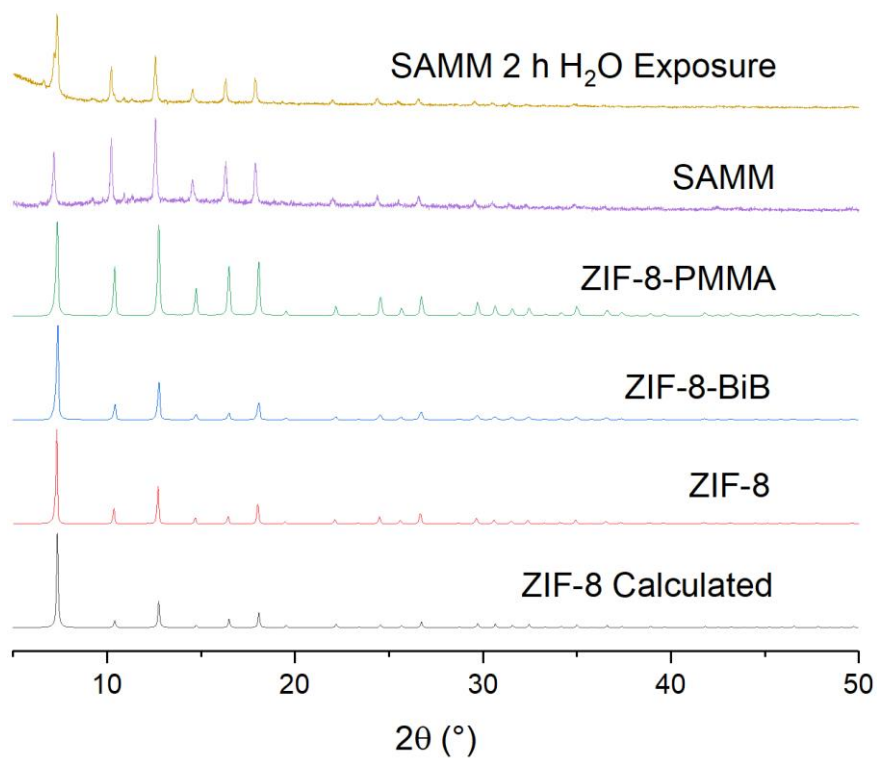
Figure 2–12.   PXRD spectra of ZIF-8 (simulated pattern), ZIF-8, ZIF-8-BiB, ZIF-8-PMMA, ZIF-8-PMMA SAMM, and ZIF-8-PMMA SAMM after exposure to H_2O for 2 h.
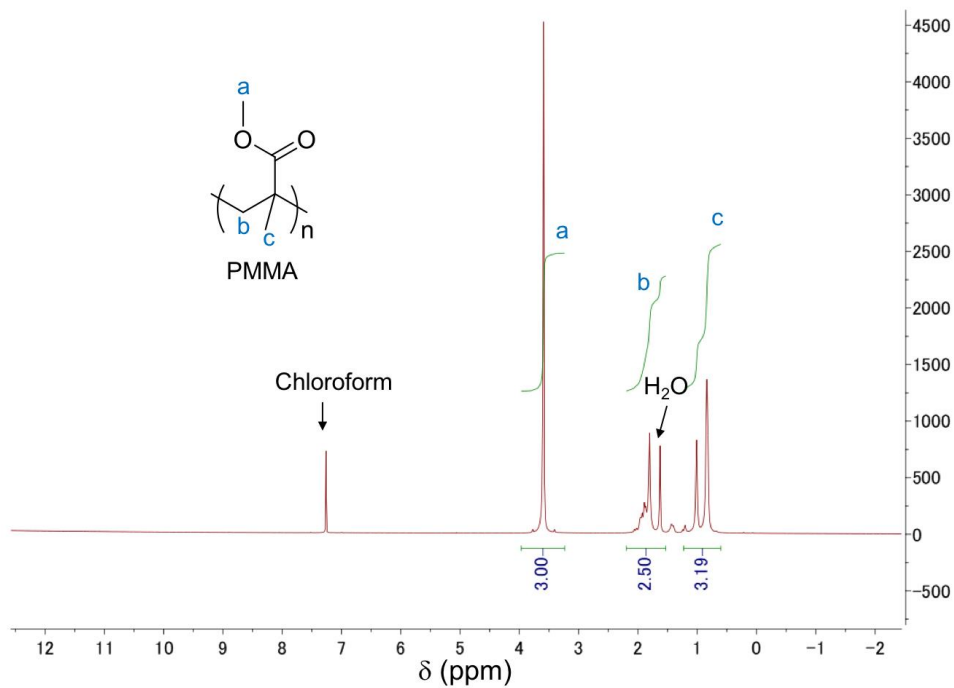
Figure 2–13. NMR spectra of digested ZIF-8-PMMA.
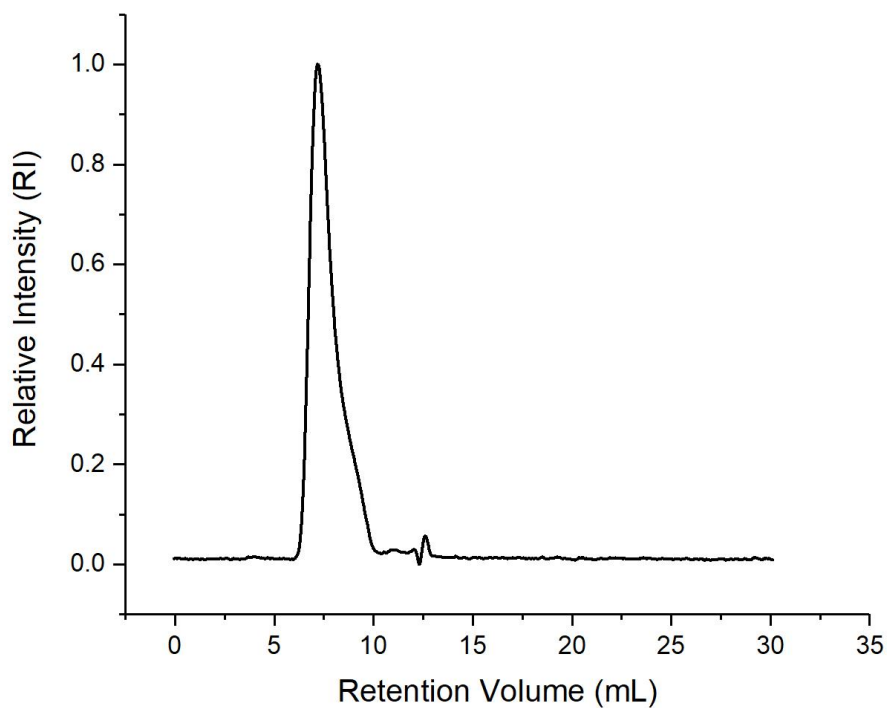
Figure 2–14. GPC trace of digested ZIF-8-PMMA.
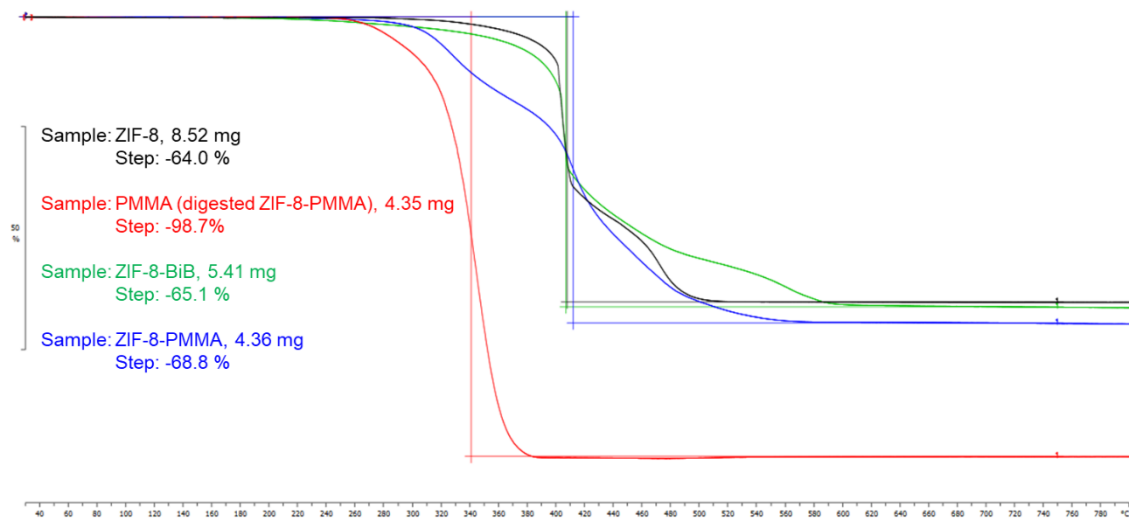
107

Figure 2–15. TGA data example for ZIF-8 (Black), PMMA (Red), ZIF-8-BiB (Green), ZIF-8-PMMA (Blue). PMMA was obtained from digested ZIF-8-PMMA. TGA was measured with 75 cm^3/min air, scan rate of 5°C/min.
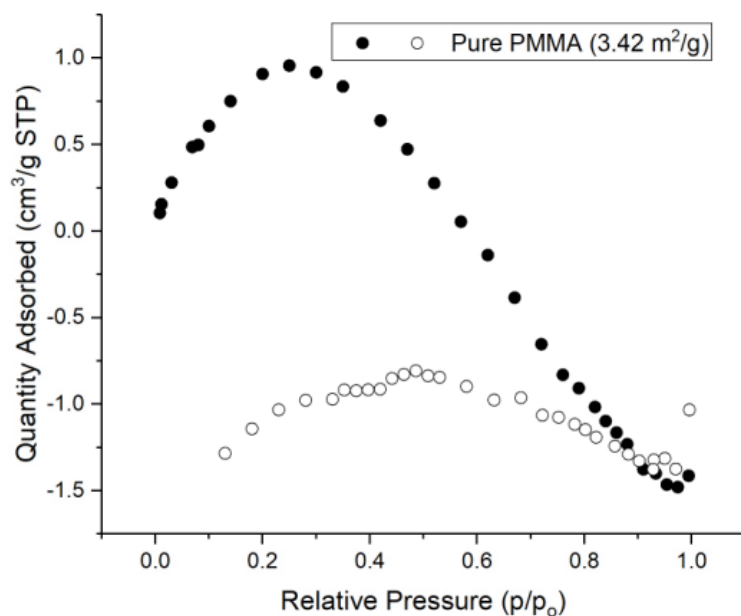
Figure 2–16. N$_2$ adsorption isotherm for bulk PMMA (Aldrich, average Mw ~120,000).

Table 2–1. Weight loss of the particles in TGA measurements, ZIF-8 contents calculated based on the weight loss, Brunauer-Emmett-Teller (BET) surface area, and contact angle measurements.

Material	Weight loss (%)	ZIF-8 wt content (%)	BET surface area (m^2/g)	Contact angle (deg)
ZIF-8	64.2	100	1625 ± 55	68
ZIF-8-BiB	64.8	>99	1557 ± 158	18
ZIF-8-PMMA	68.8	87	1398 ± 80	124

ZIF-8-PMMA showed no etching or degradation in the SEM images (**Figure 2–17**).   Interestingly, fiber-like polymers between the particles were observed in the crack of the particle aggregates which was generated by the irradiation of SEM electron beam (**Figure 2–17b**).   Transmission electron microscopy (TEM) measurement also highlights the presence of polymer around the ZIF-PMMA particles, while nothing is observed around the ZIF-8 and ZIF-8-BiB particles in the SEM images (**Figure 2–18**).   Contact angles of the particles were also measured to check the hydrophobicity of the particles.   ZIF-8, ZIF-8-BiB, and ZIF-8-PMMA demonstrated the contact angles of 68 °, 18 °, and 124 °,respectively (**Table 2–1**, **Figure 2–19**).   The ZIF-8-PMMA displayed the most hydrophobic property of all three particles, indicating that hydrophobic PMMA was successfully grafted from the surface of the particles.   As ZIF-8-BiB showed the lower contact angle compared to ZIF-8 particles, the surface of ZIF-8-BiB turned hydrophilic probably because of the presence of amide groups of the his-BiB on the ZIF-8-BiB particle surface (vide supra).
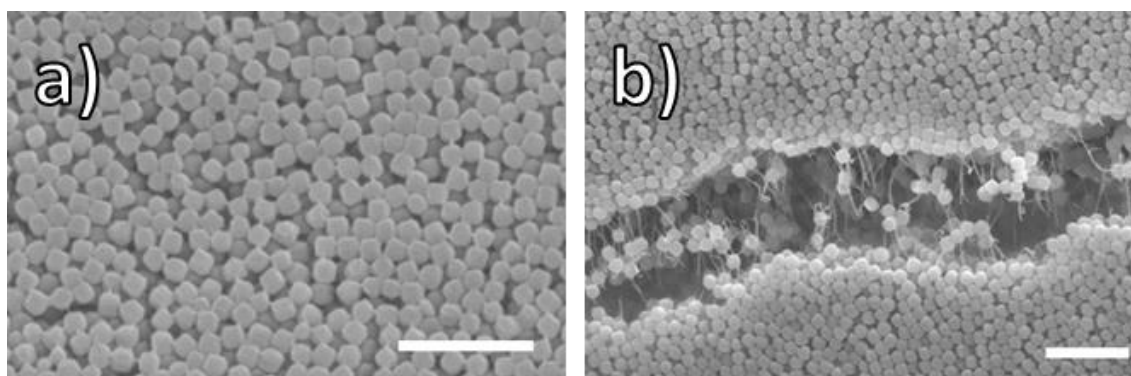
Figure 2–17.   SEM images of ZIF-8-PMMA particles: (a) ZIF-8-PMMA particles. (b) Crack of ZIF-8-PMMA aggregation.   Electron beam of SEM (5 kV) resulted in a cracked area where the presence of PMMA around the MOF particles is evident.   Scale bars are 1 μm.
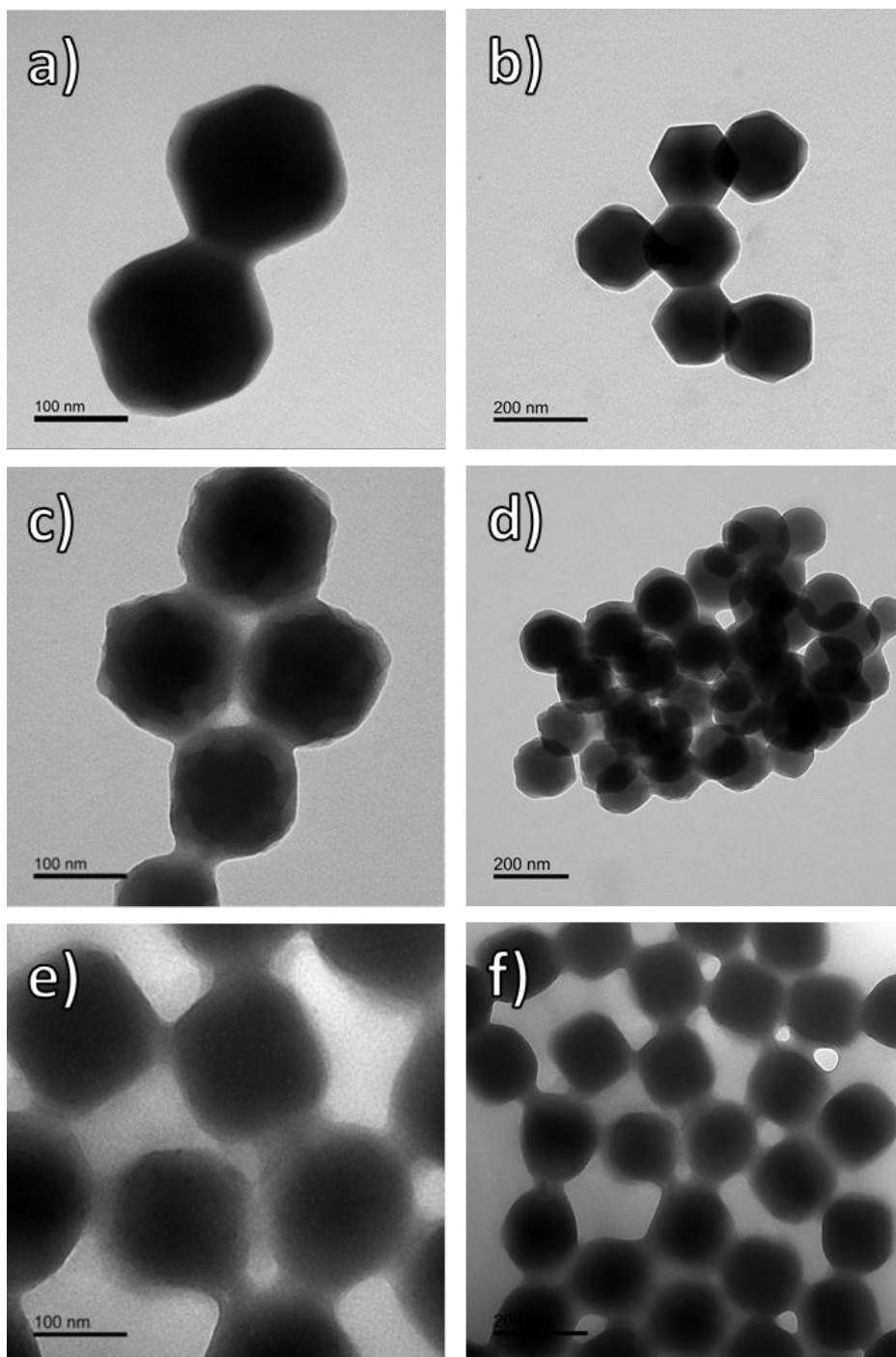
Figure 2–18. TEM image of particles: (a-b) ZIF-8, (c-d) ZIF-8-BiB, (e-f) ZIF-8-PMMA. Scale bars are 100 nm for (a), (c), (e); and 200 nm for (b), (d), (f).
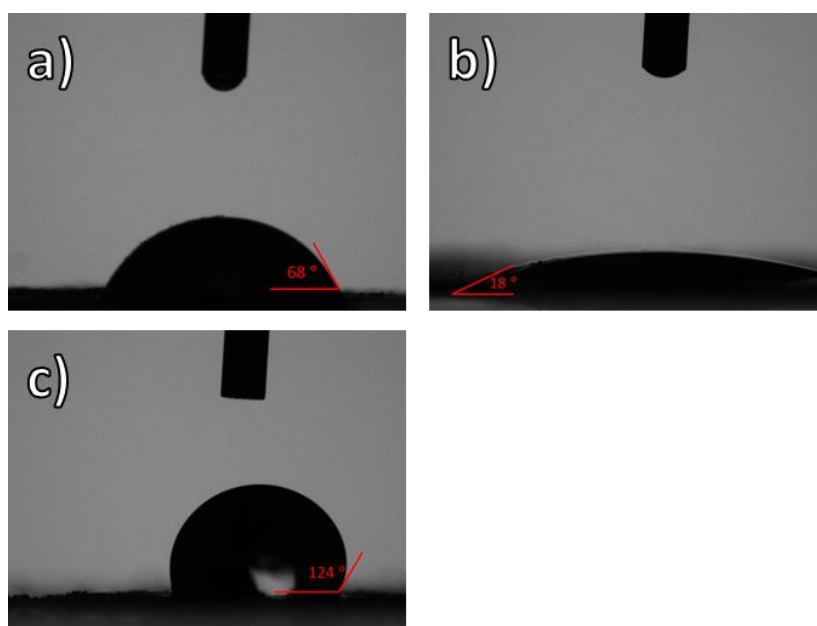
Figure 2–19. Contact angle measurements of particles: (a) ZIF-8, (b) ZIF-8-BiB and (c) ZIF-8-PMMA.

Evaporation-induced interfacial assembly at the liquid-air interface was utilized to fabricate SAMMs.　ZIF-8-PMMA particles were dispersed in toluene (30mg/ml) with sonication, and a drop of the solution (10 μL) was carefully put on the surface of the water in a Petri dish.　The solution spread immediately, generating the ultrathin layer with iridescence.　After toluene was evaporated for 1 min, the ultrathin layer was carefully scooped with a carbon tape attached on a glass plate (**Figure 2–20,** see **Video S1** in published paper**:**　J. Am. Chem. Soc. 2019, 141, 20000−20003).

In the SEM images of obtained SAMM films, the densely-packed and well-ordered particles were observed as a self-assembly structure (**Figure 2–21**).　The particles are connected each other only by taking advantage of the fusion of each PMMA shell, generating in the uniform continuous films **(Figure 2–4)**.　The reduced SEM images also display the uniform large area of the self-assembly structure with no clear defects.　Interestingly, polymer-only parts were not observed in SEM images since PMMA polymer is only located around the ZIF-8 particles.　The cross-sectional SEM images of SAMMs clearly shows that the obtained self-assembly structure is a monolayer with excellent flexibility.　The SEM images of torn parts of the SAMM (**Figure 2–21d and 2–21e**) also clearly show the flexibility and dense packing of the SAMMs, demonstrating the connection of each particle.　By measuring TEM, the overlap of the particles can be observed since the TEM electron beam can be transmitted through samples.　TEM images of SAMMs show no overlap between discrete particles, which provides further evidence of the densely packed monolayer (**Figure 2–22**).　Interestingly, the monolayer was rolled up by the irradiation of the TEM electron beam and a dynamic movement of the monolayer rolling up was observed, showing the excellent flexibility of the SAMM films.
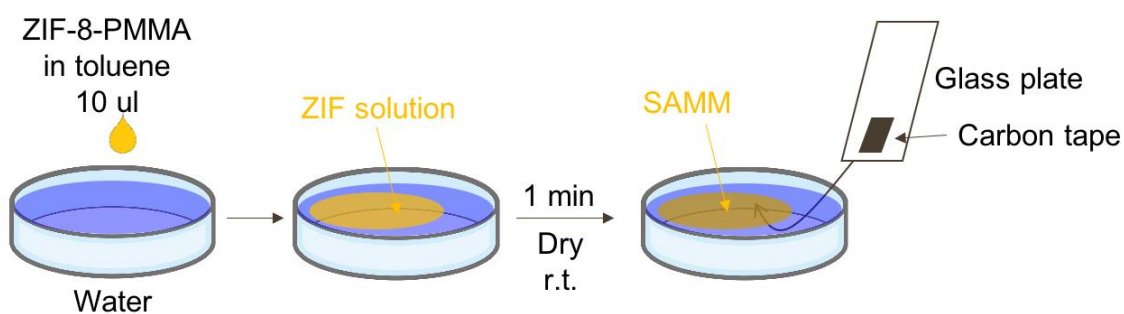
Figure 2–20.　Procedure of evaporation-induced interfacial assembly.
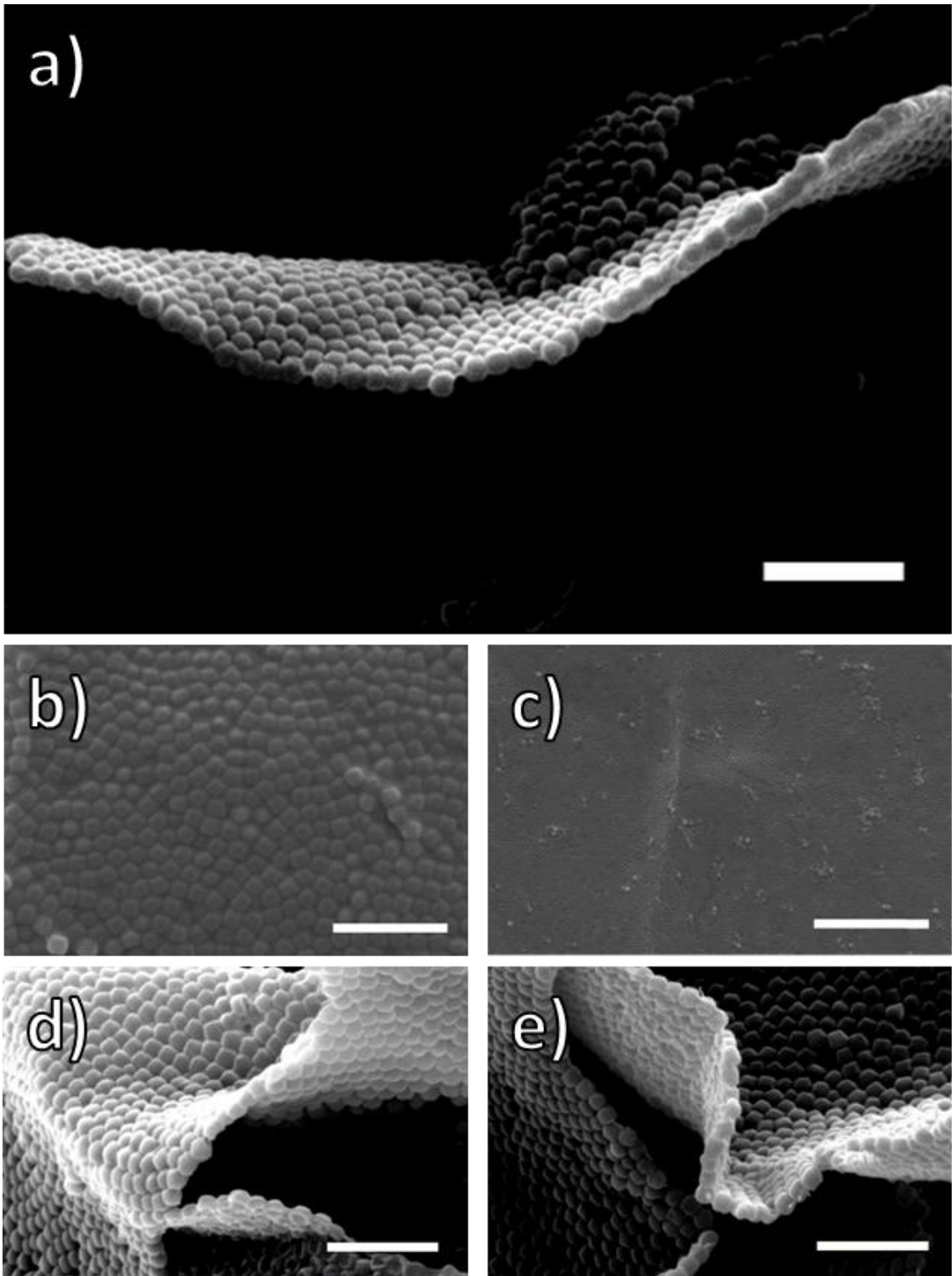
Figure 2–21. SEM images of SAMM film: (a) Cross section image. Scale bar is 1 µm. (b) Surface of the SAMM film. Scale bar is 1 µm. (c) Reduced view of the SAMM film surface. Scale bar is 5 µm. (d, e) Torn parts of the SAMM film. Scale bars are 1 µm.
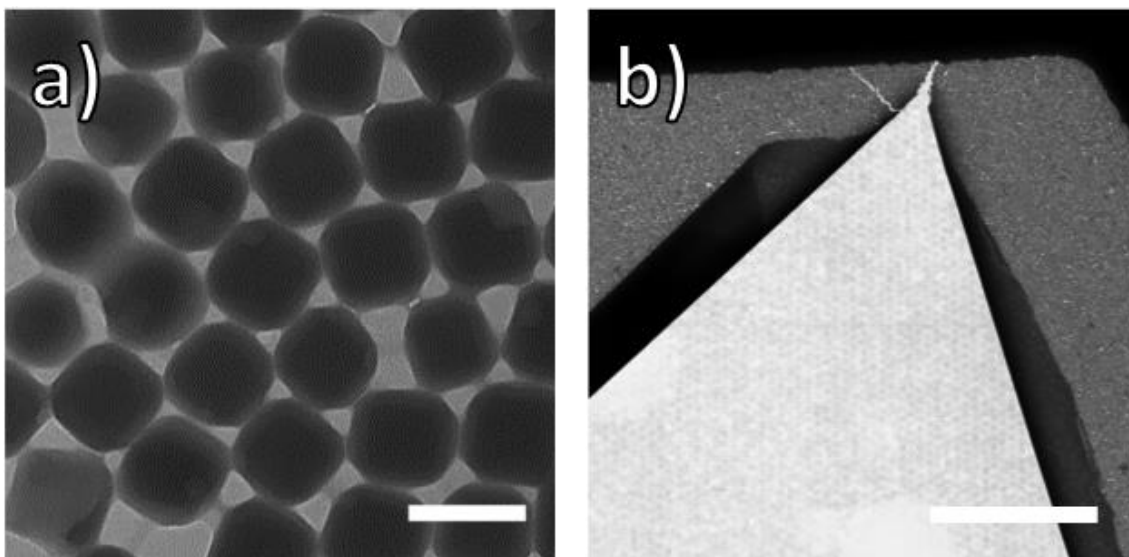
Figure 2–22. TEM image of SAMMs: (a) Scale bar is 200 nm. (b) The monolayer was rolled up through the irradiation of the TEM electron beam . Scale bar is 20 μm.

Furthermore, PXRD was measured, showing the retained ZIF-8 crystallinity of the SAMM (**Figure 2–12**).   Though it was not able to measure the porosity of SAMMs since SAMMs consist of a tiny amount of ZIF-8-PMMA, the porosity must be intact because the SAMMs are composed of only ZIF-8-PMMA particles (without adding other materials such as a polymer matrix etc.) and the crystallinity of SAMMs are retained (vide supra).   To confirm the stability of the SAMM film, SAMMs were soaked in water for 2 h.   The optical and SEM images, and the crystallinity measured with PXRD demonstrated that film did not show any change after soaking (Figures **2–12, 2–23**, and **2–24**), showing the stability of the SAMMs against water.
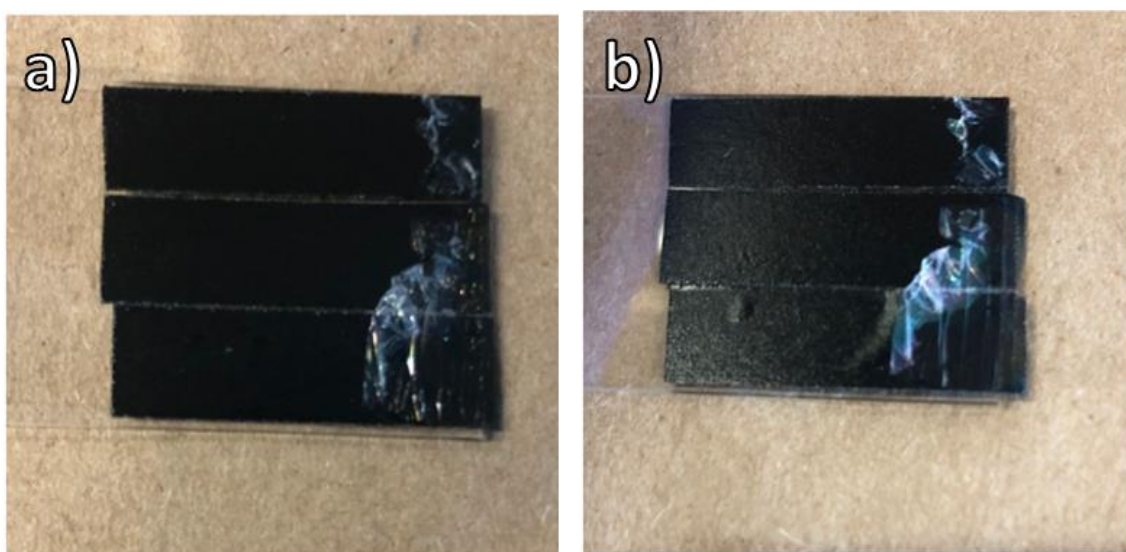
Figure 2–23.   Optical images of SAMM film on glass plate and carbon tape (a) as synthesized and b) after exposure to H$_2$O for 2 h.
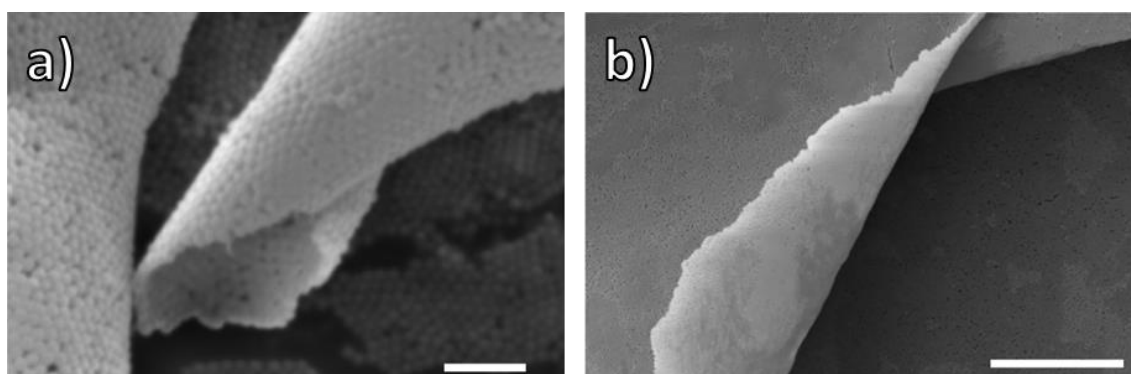
Figure 2–24.   SEM image of SAMM films after exposure to H$_2$O for 2 h: (a) Scale bar is 1 μm.   (b) Scale bars is 10 μm.

In order to clarify the advantage of core-shell MOFs toward the fabrication of SAMMs, ZIF-8, ZIF-8-BiB was also applied to the evaporation-induced interfacial self-assembly.　Right after putting a drop of the MOF solution on the water surface, the particles instantly scattered because of the evaporation of toluene.　The SEM images indicate the interfacial self-assembly of ZIF-8 and ZIF-8-BiB generated the severe particle aggregates and could not create any monolayer films. (**Figure 2–25a – 2–25d**). These results are mainly caused by the poor particle dispersibility in toluene, and the lack of factors that allow for the sufficient adhesion of each particle to form the self-assembly structure.　To further elucidate the advantage of core-shell MOF strategy, the evaporation-induced interfacial self-assembly was also applied to a physical mixture of 15 wt % of PMMA polymer (average Mw ≈ 120000, Aldrich) and 85 wt % of unmodified ZIF-8 particles, which is almost the same ZIF-8/polymer composition of ZIF-8-PMMA films.　In this case, a function of PMMA aided to form a film, however, the severe particle aggregation was observed as evidenced with the SEM images. (**Figure 2–25e, f**).　The SEM images also show that there are polymer-only parts in the film of the ZIF-8/PMMA physical mixture, which completely differs from the case of SAMMs with core-shell MOFs in which there are no polymer-only parts in the film. These results clearly show that the core-shell MOF strategy is beneficial to control the monolayer morphologies and essential to fabricate uniform ordered SAMMs.
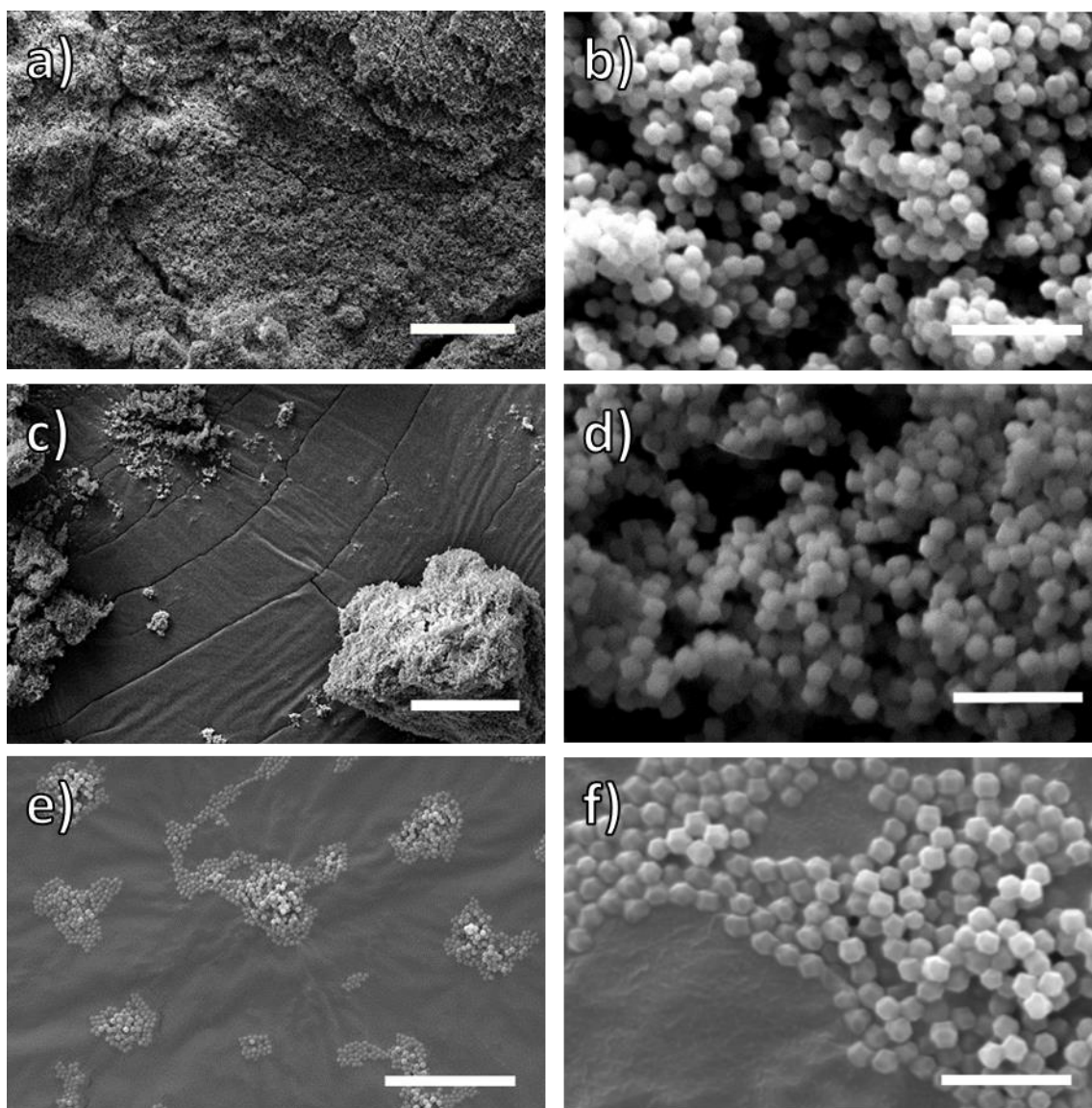
Figure 2–25. SEM image of particles obtained via the evaporation-induced interfacial assembly: (a-b) ZIF-8, (c-d) ZIF-8-BiB, (e-f) physical mixture of 15 wt% of PMMA polymer and 85 wt% of ZIF-8 particles. Scale bars are 20 μm for (a) and (c); 1μm for (b), (d), (f); 5 μm for (e).

The potential for a coating application was demonstrated by coating SAMMs on the three-dimensional structure such as microbeads. SiO_2 microparticles (particle size 5 μm, Aldrich) were used as the three-dimensional object. By scooping SAMMs with SiO_2-particle attached carbon tape, the coating was achieved. The SEM images demonstrated that the SAMM film was successfully coated on the SiO_2 particles, showing the continuous monolayer with a flexible self-assembly structure (Figure **2–26**). These results demonstrate the excellent applicability of SAMMs for coating on the three-dimensional objects, also demonstrates flexibility of the SAMM films. The further synthetic control of SAMMs was demonstrated by the fabrication of the multilayer films. The multilayer films with SAMMs were synthesized by scooping several SAMM films sequentially (homo-multilayered film). After SAMMs were scooped three times, the multilayer film showed an iridescence reflection, suggesting the presence of Bragg reflection derived from the multilayer self-assembly structure. The cross-sectional SEM images display the multilayer film with three-layer of monolayer, as expected (**Figure 2–27**). The SEM top view of the three-layer stacked film also shows that a SAMM is overlapped on the other SAMM. The crystallinity of multilayer film was maintained as evidenced by PXRD (**Figure 2–28**). Systematic variation in PXRD peak intensity suggests that the particles select preferred orientation in the film synthesis, and the similar trend has been previously reported with ZIF-8 during seeded growth of the particles.[37, 38] Additionally, multicomponent multilayer film (hetero-multilayer film) was synthesized with alternating SAMMs and PMMA thin films. PMMA thin film was selected to demonstrate that the hetero-multilayer film could be fabricated with two different layers. The film was fabricated by scooping ZIF-8 SAMM film and thin PMMA film alternately with a glass plate. The cross-sectional SEM images shows the four-layered multilayer composed of two kinds of different layers which stack alternately, demonstrating the multicomponent multilayer film (**Figure 2–29**). The top view of the SEM also shows the alternatively stacked layers, demonstrating the versatile control of multi-layer fabrication. Finally, a free-standing self-assembly film with core-shell MOF particles was achieved. A 20 mL vial was employed instead of a Petri-dish for the evaporation-induced interfacial self-assembly of the free-standing film. Since the spreading of the ZIF-8-PMMA solution is restricted by the small area of the vial, ZIF-8-PMMA particles could be stacked during the evaporation-induced interfacial self-assembly. In the SEM images, the obtained film shows approximately five SAMM layers, demonstrating the thickness of 1 μm (**Figure 2–30**). Interestingly, this film could be collected with a wire ring, obtained as a free-standing film with opalescence (**Figure 2–30c**). The stability of the

obtained multilayer film against water was also tested by putting the film in water for 2 h. The film demonstrated no breakdown as evidenced by the optical inspection (**Figure 2–31**).
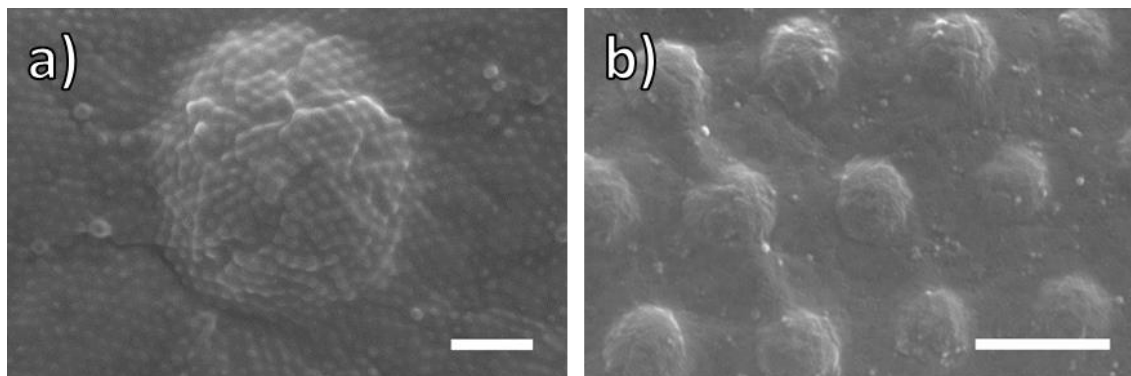
Figure 2–26. SEM images of SAMMs covering SiO_2 microparticles: (a) Scale bar is 1 μm. (b) Reduced view. Scale bar is 5 μm.
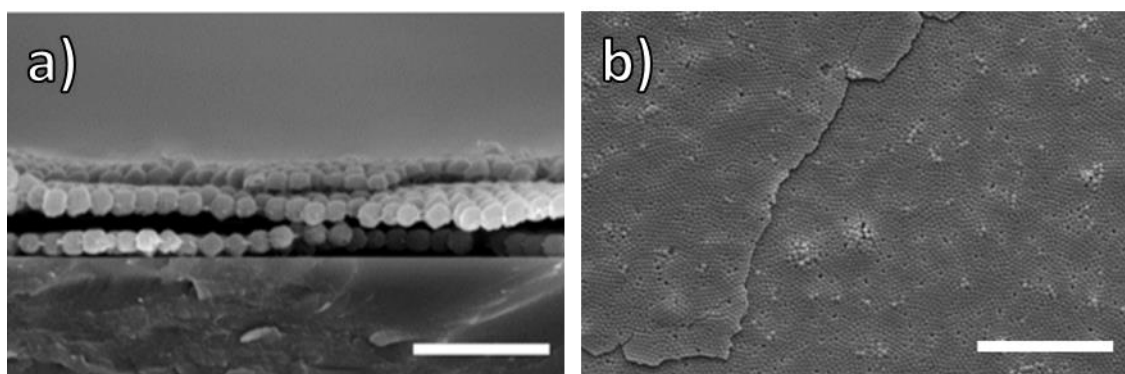
Figure 2–27. SEM images of homo-multi-layer film with SAMM: (a) Cross sectional SEM image of SAMM homo-multi-layer film (three layers). Scale bar is 1 μm. (b) Top view of SAMM homo-multi-layer film: Scale bar is 5 μm.
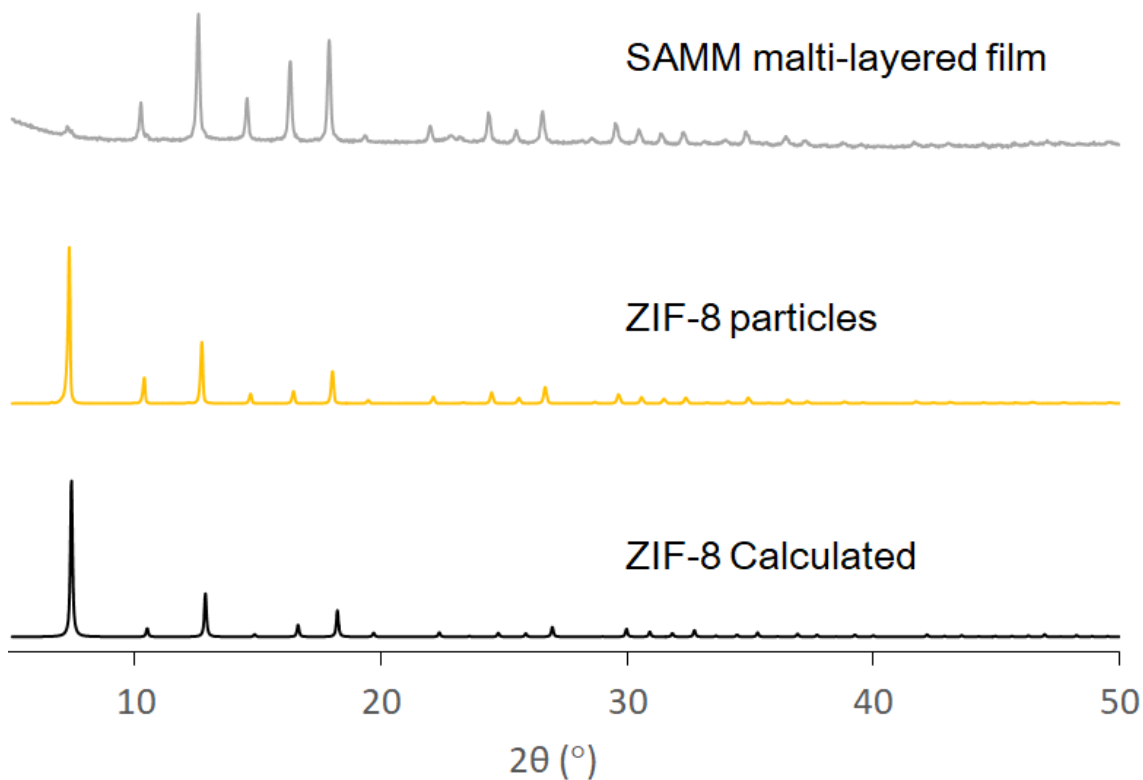
Figure 2-28. PXRD spectra of ZIF-8 (simulated pattern), ZIF-8 particles and SAMM multi-layered film.
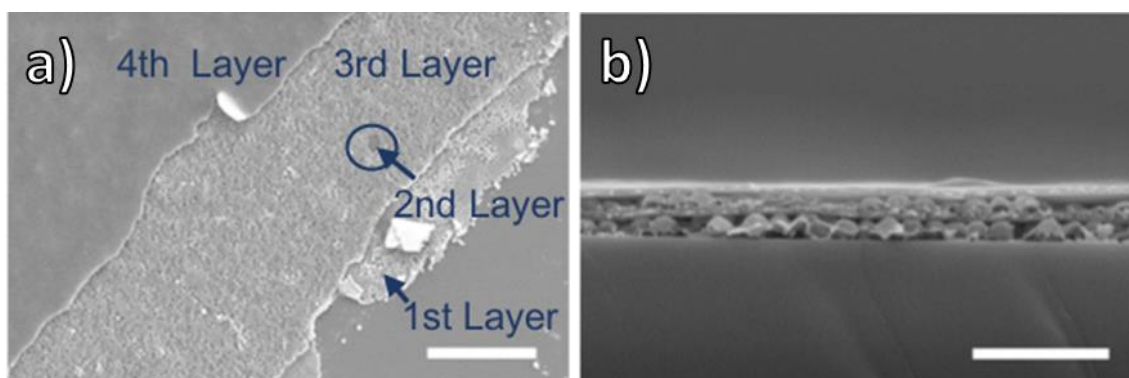
Figure 2–29. SEM images of hetero-multi-layered film consists of SAMMs and PMMA thin films: (a) Top view of hetero-multi-layered film. The 1st and 3rd layers are SAMM films, and the 2nd and 4th layers are PMMA thin films. The 2nd layer is observed in the exposed area of the 3rd layer, which is shown with a circle. Scale bar is 5 μm. (b) Cross-sectional SEM image of hetero-multilayered film. Scale bar is 1 μm.
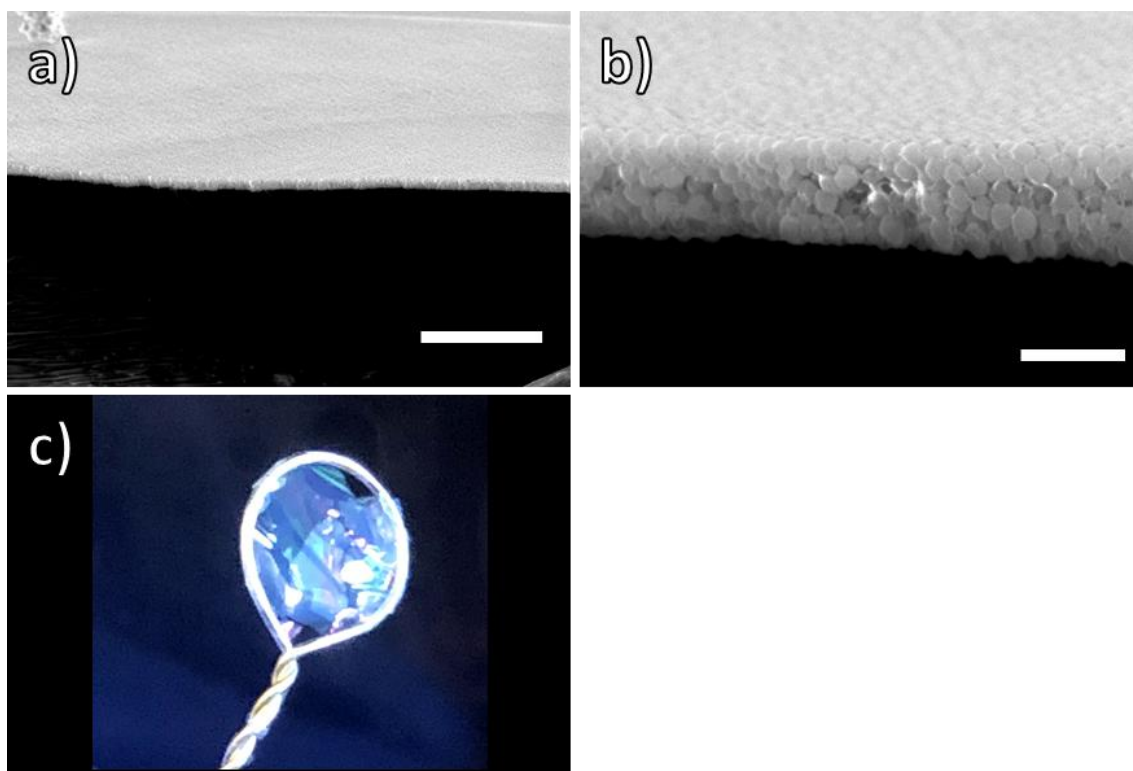
Figure 2–30. (a, b) Cross-sectional SEM image of a free-standing SAMM film: (a) Scale bar is 10 μm. (b) Enlarged view of the film. Scale bar is 1 μm. (c) Optical images of free-standing film with iridescence. A copper ring was used for collecting the free-standing film.

Figure 2–31. Optical images of SAMM multilayer film: (a) as synthesized, b) soaking in H_2O and (c) after exposure to H_2O for 2 h.

Conclusions

In this study, the synthesis Self-assembled MOF monolayers (SAMMs) with core-shell MOF particles via the liquid-air interface method was achieved.   The core-shell particles are synthesized using the combination of postsynthetic methods.   An ATRP initiator group (BiB group) was introduced to the surface of ZIF-8 particles via PSE reaction with his-BiB, resulting in ZIF-8-BiB.   Histamine acts as an anchor between ZIF-8 particles and ATRP initiator group.   ZIF-8-BiB was used for synthesizing core-shell particles of ZIF-8-PMMA via ATRP reaction ("graft-from" method) as postsynthetic polymerization.   The core-shell particles allow for the controlled synthesis of ordered assemblies to produce SAMMs via liquid-air interface method.   High MOF loading (~87 wt %, 89 vol %) and ultrathin film (only the one-particle thickness, ~200 nm) have been achieved with SAMMs, and the ZIF-8 properties of SAMMs such as the crystallinity and porosity are retained.   The SAMM films also show the excellent flexibility and no overlapping particles.

Furthermore, the homo- and hetero-multilayers were achieved by taking advantage of SAMMs, showing the ability of the excellent synthetic control.   The SAMMs have also demonstrated the potential for coating applications, showing the ability to cover Si microparticles (particle size 5 μm).   Additionally, we have also achieved unprecedented, free-standing opalescent multilayer films composed of only five stacked layers of core-shell MOF particles.

This is the first report on self-assembled porous monolayer and free-standing multilayer films with an extremely high particle loading.   We demonstrated that this core-shell strategy enables to control the properties of MOF particles towards high MOF-loaded thin films with ordered assembly.   This approach is a significant advancement towards various application including coatings and highly functional porous films.

References

1.   Shi, Q.; Cheng, W., Free-Standing 2D Nanoassemblies. *Adv. Funct. Mater.* **2019**, 1902301.

2.   Davis, M. E., Ordered porous materials for emerging applications. *Nature* **2002,** *417*, 813-821.

3.   Ackley, M. W.;   Rege, S. U.; Saxena, H., Application of natural zeolites in the purification and separation of gases. *Microporous and Mesoporous Mater.* **2003,** *61*, 25-42.

4.   Wang, C.;   Liu, X.;   Keser Demir, N.;   Chen, J. P.; Li, K., Applications of water stable metal–organic frameworks. *Chem. Soc. Rev.* **2016,** *45*, 5107-5134.

5.   Zhang, Y.;   Feng, X.;   Yuan, S.;   Zhou, J.; Wang, B., Challenges and recent advances in MOF–polymer composite membranes for gas separation. *Inorganic Chemistry Frontiers* **2016,** *3* (7), 896-909.

6.   Denny Jr, M. S.; Cohen, S. M., In Situ Modification of Metal–Organic Frameworks in Mixed-Matrix Membranes. *Angew. Chem., Int. Ed.* **2015,** *54*, 9029-9032.

7.   Kitao, T.;   Zhang, Y.;   Kitagawa, S.;   Wang, B.; Uemura, T., Hybridization of MOFs and polymers. *Chem. Soc. Rev.* **2017,** *46*, 3108-3133.

8.   Dechnik, J.;   Gascon, J.;   Doonan, C. J.;   Janiak, C.; Sumby, C. J., Mixed-Matrix Membranes. *Angew. Chem. Int. Ed.* **2017,** *56*, 9292-9310.

9.   Aroon, M. A.;   Ismail, A. F.;   Matsuura, T.; Montazer-Rahmati, M. M., Performance Studies of Mixed Matrix Membranes for Gas Separation: A Review. *Sep. Purif. Technol.* **2010,** *75*, 229-242.

10.   Cheng, W.;   Campolongo, M. J.;   Cha, J. J.;   Tan, S. J.;   Umbach, C. C.;   Muller, D. A.; Luo, D., Free-standing nanoparticle superlattice sheets controlled by DNA. *Nat. Mater.* **2009,** *8*, 519.

11.   Lee, J.;   Bhak, G.;   Lee, J.-H.;   Park, W.;   Lee, M.;   Lee, D.;   Jeon, N. L.;   Jeong, D. H.;   Char, K.; Paik, S. R., Free-Standing Gold-Nanoparticle Monolayer Film Fabricated by Protein Self-Assembly of α-Synuclein. *Angew. Chem., Int. Ed.* **2015,** *54*, 4571-4576.

12.   Pang, J.;   Xiong, S.;   Jaeckel, F.;   Sun, Z.;   Dunphy, D.; Brinker, C. J., Free-Standing, Patternable Nanoparticle/Polymer Monolayer Arrays Formed by Evaporation Induced Self-Assembly at a Fluid Interface. *J. Am. Chem. Soc.* **2008,** *130*, 3284-3285.

13.   Xiong, S.;   Dunphy, D. R.;   Wilkinson, D. C.;   Jiang, Z.;   Strzalka, J.;
Wang, J.;   Su, Y.;   de Pablo, J. J.; Brinker, C. J., Revealing the Interfacial Self-
Assembly Pathway of Large-Scale, Highly-Ordered, Nanoparticle/Polymer Monolayer
Arrays at an Air/Water Interface. *Nano Lett.* **2013,** *13*, 1041-1046.

14.   Xiong, S.;   Molecke, R.;   Bosch, M.;   Schunk, P. R.; Brinker, C. J.,
Transformation of a Close-Packed Au Nanoparticle/Polymer Monolayer into a Large
Area Array of Oriented Au Nanowires via E-beam Promoted Uniaxial Deformation and
Room Temperature Sintering. *J. Am. Chem. Soc.* **2011,** *133*, 11410-11413.

15.   Sabouri, H.;   Huang, Y.;   Ohno, K.; Perrier, S., Silica core–polystyrene shell
nanoparticle synthesis and assembly in three dimensions. *Nanoscale* **2015,** *7*, 19036-
19046.

16.   Mueggenburg, K. E.;   Lin, X.-M.;   Goldsmith, R. H.; Jaeger, H. M., Elastic
membranes of close-packed nanoparticle arrays. *Nat. Mater.* **2007,** *6*, 656.

17.   Tang, J. S. J.;   Bader, R. S.;   Goerlitzer, E. S. A.;   Wendisch, J. F.;
Bourret, G. R.;   Rey, M.; Vogel, N., Surface Patterning with SiO2@PNiPAm Core–
Shell Particles. *ACS Omega* **2018,** *3*, 12089-12098.

18.   Kiesow, I.;   Marczewski, D.;   Reinhardt, L.;   Mühlmann, M.;   Possiwan,
M.; Goedel, W. A., Bicontinuous Zeolite Polymer Composite Membranes Prepared via
Float Casting. *J. Am. Chem. Soc.* **2013,** *135*, 4380-4388.

19.   Avci, C.;   Imaz, I.;   Carné-Sánchez, A.;   Pariente, J. A.;   Tasios, N.;
Pérez-Carvajal, J.;   Alonso, M. I.;   Blanco, A.;   Dijkstra, M.;   López, C.; Maspoch,
D., Self-assembly of polyhedral metal–organic framework particles into three-
dimensional ordered superstructures. *Nat. Chem.* **2017,** *10*, 78.

20.   Lu, G.;   Cui, C.;   Zhang, W.;   Liu, Y.; Huo, F., Synthesis and Self-
Assembly of Monodispersed Metal-Organic Framework Microcrystals. *Chem. Asian J.*
2013, *8*, 69-72.

21.   Zhu, W.;   Xiang, G.;   Shang, J.;   Guo, J.;   Motevalli, B.;   Durfee, P.;
Agola, J. O.;   Coker, E. N.; Brinker, C. J., Versatile Surface Functionalization of
Metal–Organic Frameworks through Direct Metal Coordination with a Phenolic Lipid
Enables Diverse Applications. *Advanced Functional Materials* **2018,** *28* (16), 1705274.

22.   Chen, B.;   Yang, Z.;   Zhu, Y.; Xia, Y., Zeolitic imidazolate framework
materials: recent progress in synthesis and applications. *J. Mater. Chem. A* **2014,** *2*,
16811-16831.

23.   Park, K. S.;   Ni, Z.;   Côté, A. P.;   Choi, J. Y.;   Huang, R.;   Uribe-Romo,
F. J.;   Chae, H. K.;   O'Keeffe, M.; Yaghi, O. M., Exceptional chemical and thermal
stability of zeolitic imidazolate frameworks. *Proceedings of the National Academy of*

Sciences **2006,** *103* (27), 10186.

24.   Kwon, H. T.; Jeong, H.-K., In Situ Synthesis of Thin Zeolitic–Imidazolate Framework ZIF-8 Membranes Exhibiting Exceptionally High Propylene/Propane Separation. *J. Am. Chem. Soc.* **2013,** *135*, 10763-10768.

25.   Jayachandrababu, K. C.;   Sholl, D. S.; Nair, S., Structural and Mechanistic Differences in Mixed-Linker Zeolitic Imidazolate Framework Synthesis by Solvent Assisted Linker Exchange and de Novo Routes. *J. Am. Chem. Soc.* **2017,** *139*, 5906-5915.

26.   Pan, Y.;   Heryadi, D.;   Zhou, F.;   Zhao, L.;   Lestari, G.;   Su, H.; Lai, Z., Tuning the crystal morphology and size of zeolitic imidazolate framework-8 in aqueous solution by surfactants. *CrystEngComm* **2011,** *13* (23), 6937-6940.

27.   Xie, K.;   Fu, Q.;   He, J.;   Kim, J.;   Goh, S. J.;   Nam, E.;   Qiao, G. G.; Webley, P. A., Synthesis of well dispersed polymer grafted metal–organic framework nanoparticles. *Chem. Commun.* **2015,** *51*, 15566-15569.

28.   Sun, H.;   Tang, B.; Wu, P., Development of Hybrid Ultrafiltration Membranes with Improved Water Separation Properties Using Modified Superhydrophilic Metal–Organic Framework Nanoparticles. *ACS Appl. Mater. Interfaces* **2017,** *9*, 21473-21484.

29.   Liu, H.;   Zhu, H.; Zhu, S., Reversibly Dispersible/Collectable Metal- Organic Frameworks Prepared by Grafting Thermally Responsive and Switchable Polymers. *Macromol. Mater. Eng.* **2015,** *300*, 191-197.

30.   Fairen-Jimenez, D.;   Moggach, S. A.;   Wharmby, M. T.;   Wright, P. A.; Parsons, S.; Düren, T., Opening the Gate: Framework Flexibility in ZIF-8 Explored by Experiments and Simulations. *J. Am. Chem. Soc.* **2011,** *133*, 8900-8902.

31.   Zhang, C.;   Lively, R. P.;   Zhang, K.;   Johnson, J. R.;   Karvan, O.; Koros, W. J., Unexpected Molecular Sieving Properties of Zeolitic Imidazolate Framework-8. *J. Phys. Chem. Lett.* **2012,** *3*, 2130-2134.

32.   Gaillac, R.;   Pullumbi, P.; Coudert, F.-X., Melting of Zeolitic Imidazolate Frameworks with Different Topologies: Insight from First-Principles Molecular Dynamics. *The Journal of Physical Chemistry C* **2018,** *122* (12), 6730-6736.

33.   Min, K.;   Gao, H.; Matyjaszewski, K., Use of Ascorbic Acid as Reducing Agent for Synthesis of Well-Defined Polymers by ARGET ATRP. *Macromolecules* **2007,** *40* (6), 1789-1791.

34.   Lin, C. Y.;   Coote, M. L.;   Petit, A.;   Richard, P.;   Poli, R.; Matyjaszewski, K., Ab Initio Study of the Penultimate Effect for the ATRP Activation Step Using Propylene, Methyl Acrylate, and Methyl Methacrylate Monomers. *Macromolecules* **2007,** *40* (16), 5985-5994.

35.   Midya, J.; Cang, Y.; Egorov, S. A.; Matyjaszewski, K.; Bockstaller, M. R.; Nikoubashman, A.; Fytas, G., Disentangling the Role of Chain Conformation on the Mechanics of Polymer Tethered Particle Materials. *Nano Letters* **2019,** *19* (4), 2715-2722.

36.   Wang, Z.; Yan, J.; Liu, T.; Wei, Q.; Li, S.; Olszewski, M.; Wu, J.; Sobieski, J.; Fantin, M.; Bockstaller, M. R.; Matyjaszewski, K., Control of Dispersity and Grafting Density of Particle Brushes by Variation of ATRP Catalyst Concentration. *ACS Macro Letters* **2019,** *8* (7), 859-864.

37.   Zhong, Z.; Yao, J.; Chen, R.; Low, Z.; He, M.; Liu, J. Z.; Wang, H., Oriented two-dimensional zeolitic imidazolate framework-L membranes and their gas permeation properties. *Journal of Materials Chemistry A* **2015,** *3* (30), 15715-15722.

38.   Bux, H.; Feldhoff, A.; Cravillon, J.; Wiebcke, M.; Li, Y.-S.; Caro, J., Oriented Zeolitic Imidazolate Framework-8 Membrane with Sharp H2/C3H8 Molecular Sieve Separation. *Chemistry of Materials* **2011,** *23* (8), 2262-2269.

Concluding Remarks

In this thesis, the author investigated Metal-organic frameworks (MOFs)-polymer hybrid materials towards high MOF loaded thin films. The integration of MOFs and polymer can generate MOF materials with flexible form factor and processability. As the control of the MOF-polymer interfaces is the key to create the hybrid materials, the covalently integrated core-shell structured MOFs with the polymer shell were synthesized. By using postsynthetic methods, MOF particles with desired properties were obtained. Using the core-shell MOFs, the high MOF-loaded thin films including Mixed-matrix membranes (MMMs) and self-assembled MOF monolayer were achieved.

Core-shell structured corona-MOFs consisting of UiO-66-Allyl (UiO: University of Oslo) particles and poly(dimethylsiloxane) (PDMS) polymer shell were utilized to synthesis MMMs for gas separation membranes. The covalent particle/polymer integration and the improved particle dispersibility were achieved, allowing for forming defect-free MMMs with 50 wt % MOF loading without suboptimal structures. The corona-MOF MMMs demonstrate the improved separation performance, showing the potential for the flexible, free-standing thin MMMs. This is the first study that generates the covalent binding between MOF/PDMS polymer, and also the first study that achieves 50 wt % MOF-loaded PDMS MMMs without suboptimal structures and defects. This study apparently demonstrates the advantage of corona-MOFs strategy for gas separation MMMs.

Towards further potential hybrid materials, we also synthesized self-assembled MOF monolayers (SAMMs) and free-standing multilayer films. Core-shell MOF particles consisting of ZIF-8 particle and poly(methyl methacrylate) (PMMA) polymer shell were synthesized via postsynthetic methods. SAMMs were fabricated through a liquid-air interface assembly, generating an extremely thin MOF/polymer hybrid film with the controlled particle assembly method. SAMMs showed exceptional high MOF loadings (87 wt %), retaining the intact crystallinity and porosity. Exceptional synthetic controls such as fabricating alternating MOF/polymer hetero-multilayered structures, coating SAMMs on silicon microparticles, fabricating a free-standing opalescent film, were achieved. This is the first report about self-assembled porous monolayer and free-standing multilayer films composed of MOF particles. This study is a significant advancement for the coating and highly functional porous films.

As this study has demonstrated the core-shell strategies can be a strong tool to control the MOF-polymer interfaces and particle assemblies, applying this techniques to the practical application is the future interesting research field.　With a further advancement of the core-shell approach, films with unique properties would be obtained.　For the research area of MMMs for gas separation, synthesizing higher MOF-loaded MMMs containing smaller pore-sized MOFs such as ZIF-8 (ZIF = Zeolitic Imidazolate Framework) with the core-shell strategy is attractive approach.　The selection of the polymer matrix for the separation membranes and applying it to the core-shell approach would allow for the high performance membranes towards practical applications.　The fabrication of thin MOF-polymer hybrid films with high MOF loading on the porous polymer substrates would also be achievable.　On the other hand, the concept of SAMMs can be utilized to a wide range of applications such as an extremely high MOF-loaded separation membranes, photonic crystals, sensors and so on.　The development of application of SAMMs would be the interesting research field and would create the novel application which the conventional MOF powders, pure MOF films and nonporous nanoparticle monolayers cannot achieve.　The processability of MOF-polymer hybrid films, and the technique for controlling the MOF properties using core-shell strategy would accelerate the development of materials towards practical applications.

List of publications

- <u>Y. Katayama</u>, K. C. Bentz, and S. M. Cohen, "Defect-Free MOF-Based Mixed-Matrix Membranes Obtained by Corona Cross-Linking" *ACS Appl. Mater. Interfaces* **2019**, 11, 13029-13037.

- <u>Y. Katayama</u>, M. Kalaj, K. S. Barcus, and S. M. Cohen, "Self-Assembly of Metal–Organic Framework (MOF) Nanoparticle Monolayers and Free-Standing Multilayers" *J. Am. Chem. Soc.,* **2019**, 141, 51, 20000-20003.

- Y. Kiyotsuka, H. P. Acharya, <u>Y. Katayama</u>, T. Hyodo, and Y. Kobayashi, "Picolinoxy Group, a New Leaving Group for anti S_N2' Selective Allylic Substitution with Aryl Anions Based on Grignard Reagents ", *Org. Lett.* **2008**, 10, 1719-1722.

- T. Hyodo, <u>Y. Katayama</u>, and Y. Kobayashi, "Allylic substitution on the pyran ring", *Tetrahedron Lett.* **2009**, 50, 3547-3549.

- Y. Kiyotsuka, <u>Y. Katayama</u>, H. P. Acharya, T. Hyodo, and Y. Kobayashi, "New General Method for Regio- and Stereoselective Allylic Substitution with Aryl and Alkenyl Coppers Derived from Grignard Reagents ", *J. Org. Chem.* **2009**, 74, 1939-1951.

- M. Kalaj, K. C. Bentz, S. Ayala Jr., J. M. Palomba, K. S. Barcus, <u>Y. Katayama</u>, and S. M. Cohen, "MOF-Polymer Hybrid Materials: From Simple Composites to Tailored Architectures" *Chem. Rev.* **2020**, 120, accepted for publication

Acknowledgements

First of all, I would like to express the deepest appreciation to my thesis advisor Professor Masaaki Ohba (Kyushu University) for his generous support for my thesis, and kindly accepting my offer even though I am not an alumnus of his research group.   I could not have found a chance to get a PhD without his help and kindness. I would like to express my gratitude to Professor Ken Sakai, Professor Miho Yamauchi, Associate Professor Ryo Ohtani (Kyushu University) for kindly accepting my co-supervisor.

I would like to show my greatest appreciation to Professor Seth M. Cohen (University of California, San Diego) for providing a great opportunity to work in his group, his constructive suggestions, and giving me a fantastic experience at UC San Diego.   I was able to learn MOF chemistry in his group and I am really happy to have published two papers in his group.   I would like to thank Cohen lab members at UC San Diego.   I deeply grateful to Dr. Kyle C. Bentz, Mark Kalaj, Kyle S. Barcus (University of California, San Diego) for their support on my project, the fruitful discussions, helping me to write the paper.   I also learned American working style and the positive way of thinking from them.   My publications could not have been accepted without their kind help.   I want to thank Dr. Michael S. Denny, Jr. (University of California, San Diego), who accepted to be my mentor at UC San Diego and kindly taught me MOF synthesis and his MMM techniques.   I would like to thank Dr. Jessica C. Moreton, Joseph M. Palomba, Dr. Sergio Ayala, Jr. (University of California, San Diego) for having a constructive discussion and helping my US life.

I would like to express my sincere gratitude to Dr. Jinichiro Kato, Ikuya Miyamoto, Masahiko Kawashima, Dr. Noboru Kubota (Asahi Kasei Corporation) for their helpful advices.   I deeply grateful to Dr. Masato Mikawa (Asahi Kasei Corporation) for his constructive suggestion and his continuous support during my stay in the US.

I would like to express my gratitude to Professor Yuichi Kobayashi (Tokyo Institute of Technology) for his thoughtful guidance in my Master's course.   I was able to learn the skill of organic synthesis, which was really helpful to achieve the project at UC San Diego.   I am grateful to Yuta Otsubo (Kyushu University), who supported me to learn MOF chemistry at UC San Diego, and connected me with Professor Ohba.

I want to thank my family.   I would like to thank my wife, Eri Katayama, for always being the biggest supporter.   She is always cheering me up and encouraging

131

me.　I can always make a big decision in my life thanks to her support.　I would like to thank my son, Ryota Katayama, my daughter, Riho Katayama, for always making us happy and understanding me.　I would like to thank my parents, Shigeo Katayama and Reiko Katayama for their kind support.